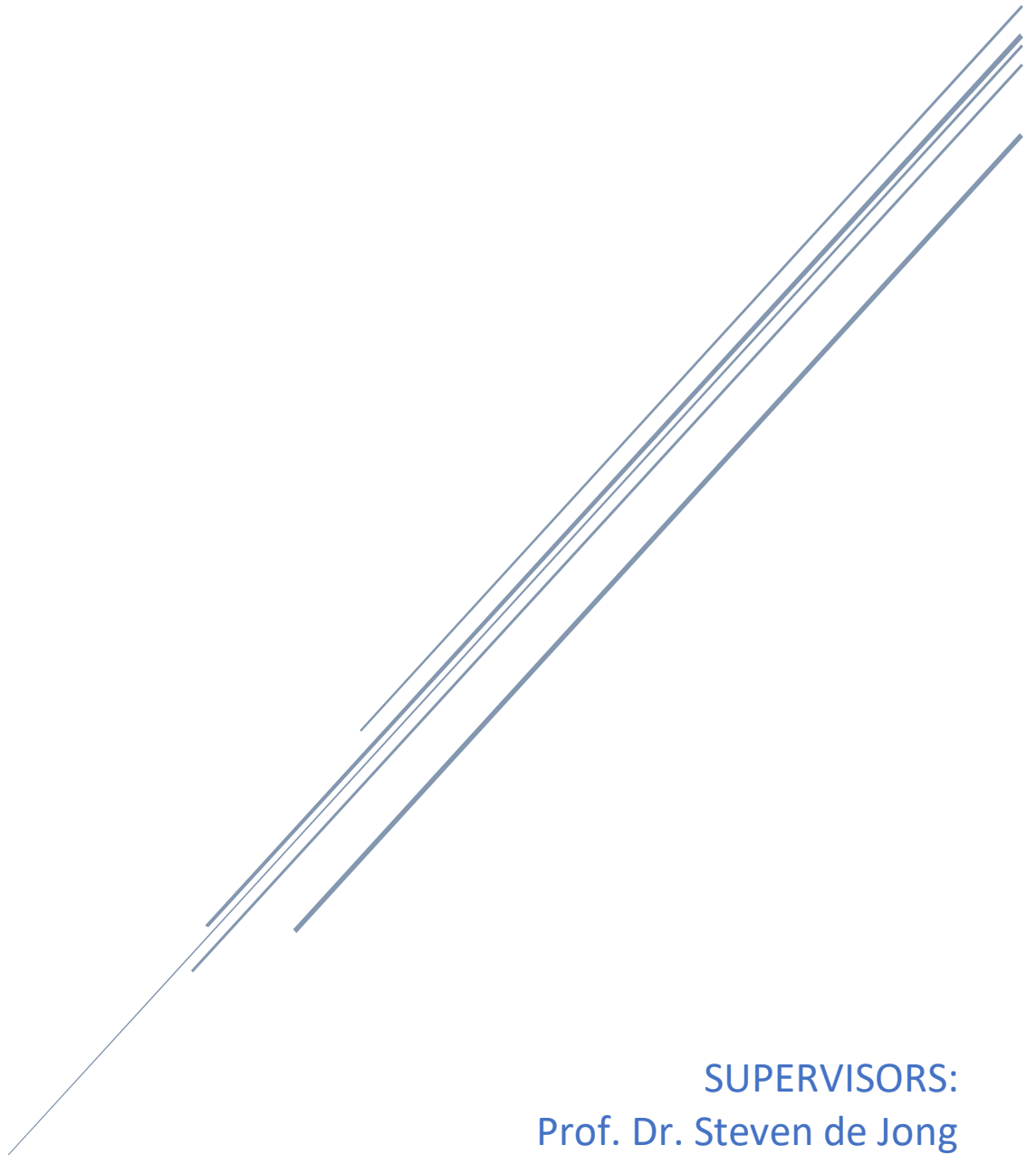


# MAPPING MINERALOGY IN THE RODALQUILAR CALDERA, SPAIN, USING PRISMA SATELLITE IMAGES

Lucía Carmona Juárez

February 2022



**SUPERVISORS:**  
Prof. Dr. Steven de Jong  
Prof. Dr. Hans de Bresser

# MAPPING MINERALOGY IN THE RODALQUILAR CALDERA, SPAIN, USING PRISMA SATELLITE IMAGES

By Lucía Carmona Juárez  
Utrecht, The Netherlands, February 2022

Thesis submitted to the Faculty of Geosciences of Utrecht University in partial fulfilment  
of the requirements for the degree of Master of Earth Structure and Dynamics

## SUPERVISORS:

Prof. Dr. Steven de Jong  
Prof. Dr. Hans de Bresser

## DISCLAIMER

This document describes work undertaken as part of a programme of study at the Faculty of Geosciences of the University of Utrecht. All views and opinions expressed therein remain the sole responsibility of the author and do not necessarily represent those of the Faculty.

## Abstract

---

The geochemical reactions that produce hydrothermal alteration in host rocks are critically important since they provide evidence of pathways of fluid and geochemical evidence for the conditions of alteration, producing 3D distribution of hydrothermal alteration zones. The understanding of this arrangement provides information useful in mineral exploration and may provide vectors to undiscovered deposits or important evidence that a terrane under assessment is favorable for occurrence of Volcanogenic Massive Sulfide ore deposit (VMS). This study presents the use of hyperspectral imagery to map and identify the hydrothermal alteration mineralogy of the epithermal gold alunite deposits in Rodalquilar (SE of Spain, Almería). The objective was recognizing faults and halos of epithermal alteration zones in two different deposits (Cerro del Cinto and Los Tollos) and their similarities in terms of geological conditions. Spectral Angle Mapper classification, a physically-based spectral classification that uses an  $n$ -D angle to match pixels to reference spectra, was applied to analyze the data from PRISMA images. Other sources of information were used to compare results and assess quality and reliability of PRISMA images. These sources were HyMap images (to which the same steps made with PRISMA images were applied), previous research performed by Arribas et al., and rock-samples collected in 2003 and 2004 in the Rodalquilar area during different campaigns performed by ITC staff and students. These rock-samples were assigned into alteration zones, allowing to create an additional map to compare and verify the existing and calculated maps. Geological knowledge of the area and a cautious in situ reflectance spectra study were considered fundamental to analyse the resulted maps from HyMap and PRISMA images. Final maps were compared and, in order to provide a better visualization of this comparison, two cross-sections crossing Los Tollos and Cerro del Cinto deposits were drawn and used to compare in a 2D design the three sources of information (VISU-Spectral information, HyMap image, and PRISMA image). The fault zone was recognizable on the SAM-map and the identified alteration of the high sulfidation epithermal system zones in Cerro del Cinto and Los Tollos deposits broadly coincide with other maps. It is also visible the differences in between these two deposits, showing a more supergene alteration zone in Los Tollos than in Cerro del Cinto. However, this study showed that PRISMA images should not be used as a single source of information. The use of PRISMA yielded to not satisfying results, which might be due to the low resolution of the images.

## Contents

1. INTRODUCTION.....	10
1.1. Research background .....	10
1.2. Volcanic rocks and society .....	11
1.3. Problem definition.....	11
1.4. Research objectives .....	12
1.5. Research questions.....	13
1.6. Thesis structure .....	13
2. DESCRIPTION OF THE STUDY AREA .....	14
2.1. Location and geology .....	14
2.2. Evolution .....	15
2.3. Mineralization model in Rodalquilar .....	17
2.4. Structural geology in Rodalquilar .....	19
3. DATASETS AND METHODS.....	22
3.1. Datasets .....	22
3.1.2. Spaceborne/airborne imaging spectroscopy.....	23
3.1.2.1. HyMap images .....	23
3.1.2.2. PRISMA images .....	24
3.1.3. Geological map IGME image .....	26
3.1.4. Rock samples .....	27
3.2. Research methods .....	28
3.2.1. Spectroscopy in the laboratory .....	28
3.2.2. Creation of local spectral library.....	29
3.3. Mineral mapping .....	30
4. IMAGE PROCESSING .....	32
4.2. Image corrections.....	33
4.3. Masking vegetation using spectral indices .....	33
4.4. Endmember extraction from HyMap and PRISMA images .....	34
4.4.1. Spectroscopy studies in Rodalquilar .....	35
4.4.2. Spectral characteristics of the high sulfidation epithermal system.....	35
5. RESULTS.....	41
5.1. Endmembers selection .....	41
5.2. NDVI Results.....	44
5.3. SAM map resulted from HyMap images using image endmembers .....	45
5.4. SAM map resulted from PRISMA images using image endmembers .....	48
5.5. Comparison with other sources of information .....	50

5.6.	Cross-sections indicating alteration zones and rock samples .....	52
5.6.1.	Cross-section from HyMap images .....	53
5.6.2.	Cross-section from PRISMA images .....	56
5.7.3.	Cross-section from rock-samples projection.....	59
5.7.4.	Comparison between PRISMA-HyMap-Rock samples cross-sections.....	61
6.	DISCUSSION .....	65
7.	CONCLUSIONS.....	67
8.	RECOMMENDATIONS.....	68

## LIST OF TABLES

Table 1.1. Main hydrothermal alteration types (simplified after Wohletz and Heiken, 1992). ...	10
Table 2.1. Alteration zones present in the area and main characteristics (Madrid et al., 2014, Ylagan et al., 1996).....	19
Table 3.1. HyMap instrument specifications. ....	23
Table 3.2. Overview of PRISMA instrument parameters. ....	24
Table 4.1. Minerals association based on literature (modified after Arribas et al., 1995). ....	36
Table 5.1. PRISMA and HyMap endmembers information. ....	41
Table 5.2. List of endmembers selected from the ITC rock-samples together with their spectral signature and location in the map. ....	42
Table 5.3. Comparison of classification from different sources (laboratory spectra, HyMap images and PRISMA image). ....	65

## LIST OF FIGURES

Figure 1.1. The larger Cinto area, which roughly marks the eastern wall of the Lomilla caldera. Most of the gold workings are concentrated in this area. ....	12
Figure 2.1. Location of Rodalquilar complex (geological and topographical maps) .....	14
Figure 2.2. (a) Geological map of Rodalquilar Caldera. (b) Geological map with indication of the caldera's borders. (c) Geological cross section of Rodalquilar Caldera covering points of interest (Lomilla Caldera and Cerro del Cinto) (Instituto Geológico y Minero de España). ....	15
Figure 2.3. Scheme of Rodalquilar and La Lomilla calderas formation (Arribas, A., 1993). 1 Rising magma to a level close to the surface. 2 Eruption of Cinto ignimbrites and first collapse. 3 Dome intrusion and resurgence of Rodalquilar caldera. 4 Eruption of Lázaras ignimbrites and second collapse; subsidence of Lomilla caldera and andesites emission; gold deposit formation. ....	16
Figure 2.4. (Left figure) Cross-section of alteration zones characteristic of high-sulphidation deposits. Diagram at left shows schematic outward zonation from a subvertical mineralized body, shown at right. (Right figure) Generalized surface alteration map (A) and cross-section (B) of the Rodalquilar HS deposit in the Rodalquilar and Lomilla calderas. ....	18
Figure 2.5. Significant mineral assemblage in the alteration zones of the Rodalquilar epithermal system (After Arribas et al., 1995) .....	18
Figure 2.6. Scheme of detailed mineral assemblages in alteration zones in Rodalquilar (Arribas et al., 1995). ....	19
Figure 2.7. Map of the Rodalquilar Caldera complex, modified from Rytuba et al., 1990 and Oopen et al., 1989. ....	20
Figure 2.8. Hydrothermal origin of deposits (modified after Arribas et al., 1995). ....	21
Figure 2.9. Localization of 340 Vein in Rodalquilar (F.Hernandez Ortiz, 2002). ....	22
Figure 3.1. True colour images of HyMap Cabo de Gata (Black lines in the center, top and bottom of the image is due to the centring and geocorrection of the images) .....	23
Figure 3.2. General scheme of Level 2 processing. ....	25
Figure 3.3. PRISMA satellite image of Rodalquilar. ....	26
Figure 3.4. Geological map of the area scale 1:50.000 MAGNA. ....	27
Figure 3.5. Setting of the two cross-sections (yellow lines) drawn along the two different hydrothermal alteration zones (Arribas et al., 1995). ....	28
Figure 3.6. Laboratory set up for spectrum measurement. (1) Source of light (2) Spectrometer (3) Spectrum Software analyzer. ....	29
Figure 3.7. PSR +3500 Instrument specifications. ....	29
Figure 4.1. Flowchart of the followed steps. ....	32
Figure 4.2. Differences between multispectral (left) imaging, only providing discrete and discontinuous portions of the spectral range, and hyperspectral (right) imaging, creating the hypercube using a large number of contiguous spectral bands. The result gives a complete spectrum for each pixel (xi, yi). Adapted from Luca Giannoni et al 2018 J. Opt. 20 044009. ....	33
Figure 4.3. Typical vegetation cover of the Rodalquilar area (Environment and Water Agency and Mountain Federation of Andalucía). ....	34
Figure 4.4. Field reflectance spectrum of vegetation in HyMap images. ....	34
Figure 4.5. Reflectance spectra from the silicic alteration zone in the visible and SWIR wavelength range (source USGS spectral library). ....	36
Figure 4.6. Reflectance spectra from the advanced argillic alteration zone in the visible and SWIR wavelength range (Source USGS spectral library). ....	37

Figure 4.7. Reflectance spectra from the supergene alteration zone in the visible and SWIR wavelength range (Source USGS spectral library). .....	38
Figure 4.8. Reflectance spectra from the intermediate argillic alteration zone in the visible and SWIR wavelength range (Source USGS spectral library). .....	39
Figure 4.9. Reflectance spectra of illite-smectite, illite and smectite in the visible and SWIR wavelength range (Source USGS spectral library). .....	39
Figure 4.10. Reflectance spectra from the propylitic alteration zone in the visible and SWIR wavelength range (Source USGS spectral library). .....	40
Figure 5.1. Spectral class selection collected from HyMap images. ....	41
Figure 5.2. Location of the rock samples selected to create the spectral library for HyMap and PRISMA images. ....	43
Figure 5.3. Comparison of alunite spectra coming from different sources. White from HyMap images (Cabo de Gata 2 & 3), red from rock sample analysed in the laboratory and green from USGS spectral library.....	43
Figure 5.4. Comparison of alunite spectra coming from different sources. White from USGS spectral library, red from rock sample studied in the laboratory and green from PRISMA images. ....	44
Figure 5.5. Spectra collected of minerals selected for SAM calculation obtained from PRISMA images. ....	44
Figure 5.6. NDVI images calculated from PRISMA images (a) and HyMap images (b). ....	45
Figure 5.7. HyMap SAM Cabo de Gata 3 on top of Cabo de Gata 2. White, blue and black lines representing important faults in the area and thick black lines representing the location of the cross-sections which will indicate the changes in the alteration zones.....	46
Figure 5.8. HyMap SAM Cabo de Gata 2 on top of Cabo de Gata 3. White, blue and black lines representing important faults in the area and thick black lines representing the location of the cross-sections which will indicate the changes in the alteration zones.....	46
Figure 5.9. Spectral signature assigned for silicic and supergene alteration zones (Source HyMap image). ....	47
Figure 5.10. Spectral signature assigned for advanced and intermediate argillic alteration zones (Source HyMap image). ....	47
Figure 5.11. Spectral signature assigned for propylitic alteration zone (Source HyMap image). ....	48
Figure 5.12. Image map resulted from PRISMA SAM classification. In this image it is noticeable the low resolution of PRISMA compared to HyMap images. ....	48
Figure 5.13. PRISMA image resulted from SAM classification. White, blue and black lines representing important faults in the area and thick black lines representing the location of the cross-sections which will indicate the changes in the alteration zones.....	49
Figure 5.14. Spectral signature assigned for silicic and supergene alteration zones. ....	49
Figure 5.15. Spectral signature assigned for advanced and intermediate argillic alteration zones. ....	50
Figure 5.16. Spectral signature assigned for propylitic alteration zone. ....	50
Figure 5.17. Alteration map of the Rodalquilar area (modified after Arribas et al., 1995) which show alteration patterns. ....	51
Figure 5.18. Alteration map of the Rodalquilar area (modified after Arribas et al., 1995) showing alteration patterns on top of HyMap images. ....	51
Figure 5.19. Alteration map of the Rodalquilar area (modified after Arribas et al., 1995) showing alteration patterns on top of PRISMA image.....	52

Figure 5.20. Final setting of cross-sections (on top of PRISMA image) used to represent alteration zones distribution. Yellow stars symbolize rock-samples collected in the field and studied in the laboratory.....	53
Figure 5.21. A. Location of the cross-section selected. B. Cross-section P.T.2 from Los Tollos deposit.....	54
Figure 5.22. HyMap image of Los Tollos with P.T.2 cross section (black) and important faults (white, blue and black) influencing the deposit. ....	55
Figure 5.23. A. Location of the cross-section selected. B. Cross-section P.C.2 from Cerro del Cinto deposit. ....	55
Figure 5.24. HyMap image of Cerro del Cinto with P.C.2 cross section (black) and important faults (white, blue and black) influencing the deposit.....	56
Figure 5.25. A. Location of the cross-section selected. B. Cross-section P.T.2 from Los Tollos deposit with blue and white arrows indicating important faults (W-E and N-S, respectively). ...	57
Figure 5.26. SAM classification of PRISMA images. White, blue and black lines represent important faults within the deposit of Los Tollos.....	58
Figure 5.27. A. Location of the cross-section selected. B. Cross-section P.C.2 from Cerro del Cinto deposit with black, blue and white arrows indicating important faults (radial, W-E and N-S, respectively).....	58
Figure 5.28. SAM classification of PRISMA images. White, blue and black lines represent important faults within the deposit of Cerro del Cinto.....	59

# 1. INTRODUCTION

## 1.1. Research background

The most important gold deposits of the Southeastern part of the Iberic Peninsula are located in the Miocene caldera of the volcanic field of Cabo de Gata, in the province of Almería. Mineralisations occurring in this area with a volcanic origin have been formed at shallow depths from hydrothermal fluids which origin is related to magmatic activity (Arribas, A., 1993). The metallic mining started at the beginning of IX century with the extraction of Silver, Lead and Zinc minerals in the Quartz veins located close to San José village where, later during 1880, gold was discovered. Afterwards gold was also found in the veins close to Rodalquilar (around 10 kms to the N-W) and, eventually, mining became more intense in this area with a final production of 6 tons between 1943 and 1966. At present, the district remains inactive for gold mining.

Hydrothermal mineralizations and alterations in the area have characteristics that are typical of epithermal type of mineral deposits (Demoustier et al., 1999). Mineralizations within the Rodalquilar caldera complex consist of low-sulphidation (sulfidation Pb-Zn-(Cu-Ag-Au) quartz veins) and most important high-sulphidation (Au-(Cu-Te-Sn) ores) sub-type of epithermal deposits (Arribas et al., 1995).

Mineral associations and alteration zones in epithermal systems occur due to the interaction of the hot fluids (with different pH values, different salinity, temperature and pressure) with the host rock at shallow depths. They occur with characteristic alteration mineral assemblages as shown in table 1.1. Understanding the main hydrothermal alteration types and their characteristics is key for proper alteration zoning and for exploration of epithermal gold deposits.

Alteration type	Alteration characteristics	Mineral assemblages	
		High sulphidation	Low sulphidation
Silicification	Characterized by introduced silica or a silica residue after total hydrolysis	Quartz+alunite+chalcedony ± jarosite, alunite, barite	Chalcedony ± opal, adularia
Advanced Argillic Alteration (AAA)	Minerals representing extreme base leaching (for example alunite, kaolinite) and sulfates such as alunite	Alunite+chloritic ± pyrophyllite, kaolinite, dickite, topaz, quartz	Kaolinite + alunite ± illite/smectite- native sulfur
Sericitic-argillic	Sericite + kaolin-smectite- group minerals	Kaolinite + illite ± montmorillonite, smectite, sericite, quartz, k-feldspar	Illite ± illite-smectite
Argillic	Kaolin- and smectite- group minerals (for example montmorillonite); does not typically include mica-type minerals	Kaolinite/dickite + montmorillonite ± illite-smectite, sericite, quartz	Kaolinite (or halloysite, or dickite) + sericite (or muscovite) ± montmorillonite, chlorite
Propylitic	Characterized by chlorite, albite, epidote, carbonate +- pyrite, Fe-oxides and minor sericite	Epidote + albite ± chlorite, calcite, k-feldspar	Epidote + carbonate ± chlorite, albite, sericite, montmorillonite

Table 1.1. Main hydrothermal alteration types (simplified after Wohletz and Heiken, 1992).

These alteration zones and mineral assemblages can be identified by the use of visual observation, remote sensing techniques and spectral studies.

## 1.2. Volcanic rocks and society

Beyond the academic interest that volcanic rocks possess, their importance to society is huge and twofold. There is the intimate relationship between volcanic rocks and ore deposits, for example, the volcanic hosted massive sulfides (VMS) with Cu, Pb, and Zn, and the epithermal precious (gold and silver) metal deposits.

Cabo de Gata is an excellent example of this type of deposits: The Rodalquilar gold deposits, hosted by pyroclastic rocks of Miocene age within a large volcanic caldera. In this respect, the need for minerals worldwide is progressively growing, increasing this way the demanding to find new mineral resources, map mining sites, estimate ore reserves and conduct the geological planning of a mining operation.

The mines of Cerro del Cinto and the plant Denver (where the auriferous material extracted was cyanided and threated) were the central axis in which the economy of Rodalquilar was rotating, being its motor of development and growth between the years 1948 and 1996, dealing to the admiration from a big part of the province of Almería. But at the same time plant Denver became the monoculture to which Rodalquilar commended all its future. There were practically no economic activities independent from Denver plant. In this way, when Cerro del Cinto gold deposits started to falter, all the economy and society of Rodalquilar suffered from this factor and throughout the year 1996 they eventually collapsed.

It was not until the 1990 decade when local economy started to grow based on the tourism attracted to its natural values, nationally recognized with its declaration as Natural Marine-Terrestrial Park of Cabo de Gata Níjar (1987) and internationally with the declaration from UNESCO of the Biosphere Reserve of Cabo de Gata-Níjar (1997) and the European Geopark of Cabo de Gata-Níjar (2006).

However, there is still to recognize and put in value the prominent Mining Heritage, composed by sustainable values that can be a solid and noted point for the wellness of the local residents (Hernández et al., 2016).

## 1.3. Problem definition

Previous studies have employed different methods to map and identify the alteration in minerals in the study area, as is the use of petrography and geochemical techniques (Arribas et al., 1995), remote sensing techniques with an airborne (Benidini et al., 2009), SWIR non-imaging spectroscopy on rock samples (García, 2013) and SWIR imaging spectroscopy on rock samples (Contreras A., 2017). Regarding spectral signatures, Bedini et al., 2009 used HyMap imaging spectrometer to map the distribution of alunite, kaolinite, smectite-illite and pyrophyllite. Van der Werff et al., 2016 used Sentinel and Landsat images to map mineralogy associated with a hydrothermal alteration system in southeast Spain.

Limitations with remote sensing techniques are defined by the characteristics of the spaceborn sensors in use. For example, Landsat-5 Thematic Mapper is used by Arribas et al., 1995. This study is constrained to 7 spectral bands with a lower resolution since Landsat-5 has wider spectral bands, loosing relevant information of spectral signatures from minerals.

Bandwidth is key for identifying the narrow absorption features of minerals in full spectra. Narrowband sensors capture reflectance from a very specific area of the spectrum, providing more detailed information. Observation of the reflectance properties of minerals in very narrow VIS and NIR bands can be correlated with specific physico-chemical characteristics such as their physical structure, or water content and can, therefore, provide significant improvements in their identification.

Therefore, this research uses the innovative PRISMA hyperspectral spaceborne in order to improve our understanding of processes and mineral spreading in hydrothermal alteration zones, being the first spaceborne that covers light from 0.4  $\mu\text{m}$  to 2.5  $\mu\text{m}$  with 255 spectral bands with 10 nm spectral sampling through two partially overlapped spectrometers and in addition a co-registered Panchromatic camera of 5m, making possible to compare them with HyMap images. HyMap is an advanced hyperspectral sensor that covers the 0.45 to 2.48  $\mu\text{m}$  region with 126, approximately 15-nm-wide spectral bands with 3-10m spatial resolution.

#### 1.4. Research objectives

The aim of this project is based on the production of hydrothermal maps by using the new technology of PRISMA spaceborne to improve our understanding of the hydrothermal processes and composition of the area. For that we will focus on the area of Rodalquilar, comparing these obtained images with products obtained by older technologies as are airborne images, HyMaps and spectral libraries.

Overall, the geology of the area is well known, based on fieldwork and previous remote sensing work. However, questions still remain on the role of the fault and joint systems, and on the reasons for the division of Rodalquilar district into two major areas of very intensely altered (Cinto and Los Tollos).

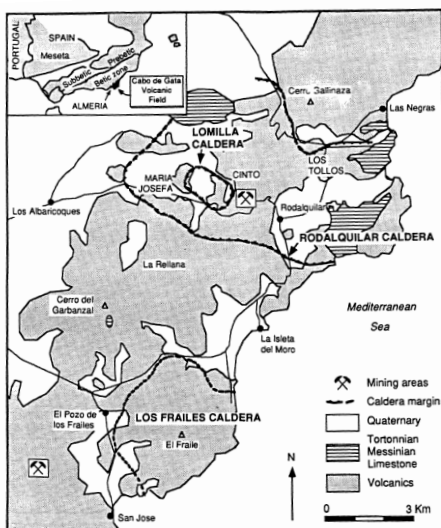


Figure 1.1. The larger Cinto area, which roughly marks the eastern wall of the Lomilla caldera. Most of the gold workings are concentrated in this area. To the northeast, the Los Tollos area shows the effects of advanced argillic alteration with numerous abandoned alunite open pits but gold has not been found there.

With this research it is expected to be able to identify and map the spatial distribution of surface mineralogy, which will be indicative for the underlying geology.

This map will also be indicative of the processes in the hydrothermal areas, as is the interpretation of the distribution of pressure and temperature of the system, the geochemistry, how the faults played a role in determining the hydrothermal processes, the

classification in time of this faults (pre-, syn-, post-events), differentiation between the two main alteration zones (Los Tollos and Cerro del Cinto).

The specific objectives include the interpretation of alteration zones, the production of a hydrothermal map, the production of sub-maps, the creation of a spectral library of local rock-samples, the production of cross-sections and the quality assessment of the hydrothermal map obtained.

#### 1.5. Research questions

- Which are the rock-types determining the differenced sub-areas identified within Rodalquilar?
- Which is the influence of faults present in this system? Which is the classification of the faults system (pre-, syn-, post- events)
- Which existing faults are influencing the hydrothermal system? How is the development of the system affected by faults?
- Which properties and characteristics make the area subdivided in Cerro de los Cintos and Los Tollos?
- Which is the distribution of pressure and temperature parameters along the system?
- Which is the distribution and diffusion of minerals present in the area?
- Is PRISMA spaceborne useful for surveying hydrothermal regions?

#### 1.6. Thesis structure

This research Project is structured into 6 chapters. Chapter 1 introduces the research background, volcanic rocks and society, problem definition, research objectives and research questions. Chapter 2 description of the study area, including location and geology, evolution, mineralization model and the structural geology in Rodalquilar. Chapter 3 comprises datasets used and methods applied; starting with spaceborne/airborne imaging spectroscopy, including technical data of HyMap airborne and PRISMA spaceborne and the images acquired with them, description of IGME images and the rock-samples obtained in the field, it also includes a as research methods spectroscopy in the laboratory) and creation of spectral library (as research methods) and, finally, mineral mapping. Chapter 4 comprises image preprocessing, this are image corrections, NDVI and endmember extraction from HyMap and PRISMA images, containing the last chapter information of spectroscopy studies in Rodalquilar and spectral characteristics of the high sulfidation epithermal system. Chapter 5 consists on the results obtained after chapter 4. Those are endmembers selected, NDVI mask, local spectral library, SAM maps resulted from the different sources, comparison with other sources of information and cross-sections indicating alteration zones and rock samples. Chapter 6 being the discussion of the results obtained and final conclusions and recommendations for future projects using PRISMA images Chapter 7 and 8, respectively.

## 2. DESCRIPTION OF THE STUDY AREA

### 2.1. Location and geology

The Miocene Cabo de Gata (Figure 2.1) volcanic field is located along the south-eastern coast of Spain and is the only extensive area of Tertiary volcanic rocks in the country (Cunningham et al., 1990, Part II). The volcanic field extends for 40 km along the Mediterranean Sea, and in the western part of the field, regionally extensive rhyolite to dacite ash-flow tuffs, and andesitic stratovolcanoes and cones are present.

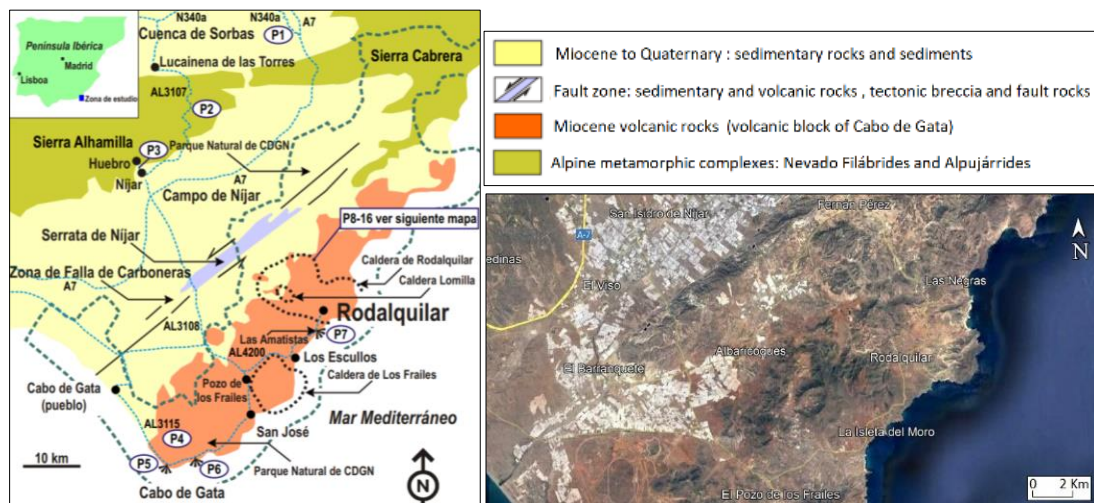


Figure 2.1. Location of Rodalquilar complex (geological and topographical maps)

In this area the Rodalquilar caldera complex is located, which is a collapse-structure, with oval form, with approximately 8 km long in E-W direction and 4 km long in N-S direction. It consists of a nested caldera, Caldera of Rodalquilar, located 8 km to the North of the older Los Frailes caldera, developed on an older andesitic volcanic field composed of coalescing stratovolcanoes and cones (Cunningham et al., 1990, Part II); this hosts in turn a second smaller caldera, Lomilla Caldera, in its central part (Rytuba et al., 1990). The rocks composition varies between basaltic andesites, andesites, dacites, rhyodacites and rhyolites (López Ruis and Rodríguez-Badiola, 1980; Di Battistini et al., 1987; Toscani et al., 1990).

Within this caldera The Rodalquilar gold-alunite deposit is located, one of the best-exposed epithermal high-sulphidation systems in the world. The geological evolution as well as the hydrothermal alteration in this deposit have been studied mainly by using petrographical and geochemical techniques (Arribas et al., 1995), although recent research has proved that the implementation of remote sensing spectroscopy is highly convenient in this area (Bedini et al., 2009), since several short-wave infrared (SWIR) active minerals are present in the hydrothermal alteration assemblage, making it possible to use remote sensing for mapping the spatial distribution of the alteration mineralogy.

There are two important hydrothermal altered spots in the volcanic field of Rodalquilar caldera complex: one of them is Cerro del Cinto, in which gold deposits are located, and the other is Los Tollo, in which there are only small open mines for Alunite (Figure 2.2).

The Los Tollos alunite deposits are localized in collapse breccias and intracaldera Cinto ash-flow tuff and Lazaras ash-flow tuff about 0.5 km from the north-central margin of the Rodalquilar caldera. The deposits were mined by open pit methods and consist primarily of replacement alunite in which the original texture of the collapse breccia and ash-flow tuff is well preserved. Narrow veins of alunite with minor jarosite are locally present but constitute a minor part of the ore body (Rytuba, et al., 1989).

On the southeast flank of the resurgent dome of the Rodalquilar caldera, an unnamed alunite deposit was developed in intracaldera Cinto ash-flow tuff and interbedded collapse breccia. The open pit mine was developed in a zone of veining where alunite is present primarily as vein filling up to 30 cm in width. The vein zone was localized along a north-south fault. Replacement alunite and small alunite veinlets extend outward into the country rock but vein density decreases (Rytuba, et al., 1989).

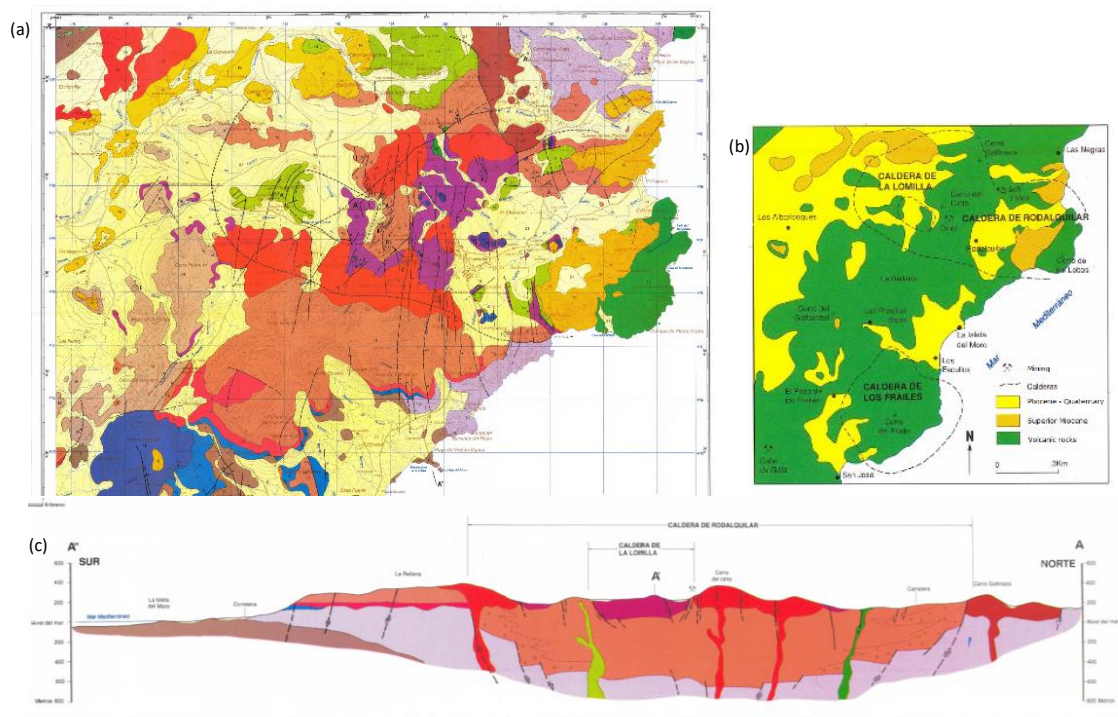
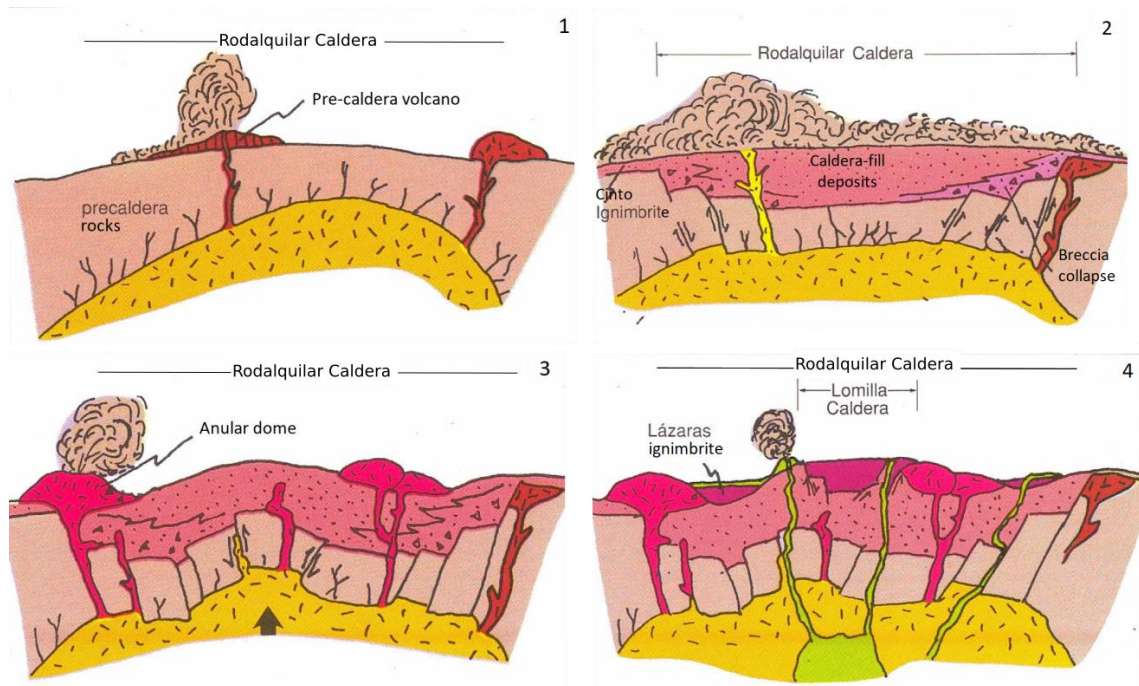


Figure 2.2. (a) Geological map of Rodalquilar Caldera. (b) Geological map with indication of the caldera's borders. (c) Geological cross section of Rodalquilar Caldera covering points of interest (Lomilla Caldera and Cerro del Cinto) (Instituto Geológico y Minero de España).

## 2.2. Evolution

The formation of the Rodalquilar caldera complex can be divided into five phases:



*Figure 2.3. Scheme of Rodalquilar and La Lomilla calderas formation (Arribas, A., 1993). 1 Rising magma to a level close to the surface. 2 Eruption of Cinto ignimbrites and first collapse. 3 Dome intrusion and resurgence of Rodalquilar caldera. 4 Eruption of Lázaras ignimbrites and second collapse; subsidence of Lomilla caldera and andesites emission; gold deposit formation.*

A first phase of magma ascent. This scheme (Figure 2.3 part 1) corresponds to the original setting of Rodalquilar caldera complex.

A second phase is the Cinto Ignimbrite eruption and collapse (Figure 2.3 part 2). Collapse of Rodalquilar caldera was 11 M.a as a consequence of the eruption of Cinto ignimbrites, which correspond to a thick serie of pyroclastic materials of dacitic and rhyolitic composition. The morphology of the caldera has been well conserved in its central part, however oriental and occidental borders are covered by marine sediments and younger volcanic rocks. The border of the caldera is structural and coincides with a vertical fault that has more than 2 kms length and which splits the precaldera dacitic domes from Cinto riolites.

A third phase is dome intrusion (Figure 2.3 part 3). As it frequently happens with these kind of volcanic structures, there was a reactivation of magmatic processes in the central part of the caldera which lead to the emplacement of anular-rhyolitic domes, which outcrops can be found approximately along 5 kms in the meridional border of the caldera. They are composed of massive dacites and rhyolites which frequently have a foliation flow and are surrounded by breccias from debris avalanches.

The fourth phase is the eruption of Lázaras ignimbrites and collapse (Figure 2.3 part 4). The resurgence of the Rodalquilar caldera culminated with the explosive destruction of its central part and the emission of Lázaras ignimbrite, which was deposited in the trench and in sunken zones of the caldera, where it reaches 80 m deep. The eruption of this ignimbrite lead to the formation of La Lomilla caldera, with a diameter of maximum 2 Km. The oriental topographic border of this caldera is well preserved and corresponds to the actual occidental slope of

Cerro del Cinto. Au mineralisations present in this area are associated with tangential and angular faults of La Lomilla caldera.

On top of Las Lázaras ignimbrites, fine lake grain sediments, highly silicified volcanoclastic breccias and lava flows were successively deposited. During this episode important faults were created, mainly N-S direction, in which convective hydrothermal circuits were developed, leading to mineralizations and to the large halo that characterizes Rodalquilar.

The last volcanic episode is represented by andesites lavas, breccias, diques and chimneys that are identical to the younger andesites from Los Frailes caldera. These rocks are specially found in the oriental border of Rodalquilar Caldera complex, in Lobos area, and have an age between 8.5 and 7.5 Ma. They are younger than the mineralization, therefore they are not altered.

The final phase consists of sea incursion during Superior Tortonense and Messiniense (8.5 and 5.5 Ma ago). A large part of the volcanic area of Cabo de Gata, including Rodalquilar area, was covered by the sea, leading to the deposition of a massive series of detritic sediments and reef limestones from which still remains many signs. This incursion of sea water into the caldera occurred after the late-stage resurgence, because these strata are not deformed (Cunningham et al., 1990, Part II).

### 2.3. Mineralization model in Rodalquilar

The ore deposits in the Rodalquilar caldera complex are mainly alunite, gold-alunite of high-sulphidation origin, and lead-zinc-silver-gold of low-sulphidation origin. The age of mineralization and hydrothermal alteration within the Rodalquilar caldera complex is younger than the Lomilla caldera and sedimentary and volcanic rocks which fill the moat of the Rodalquilar caldera. It occurred during the early phase of andesitic volcanism but ended before the last flows were emplaced at  $9.0 \pm 0.6$  Ma (Rytuba et al., 1989).

Hydrothermal processes at Rodalquilar were influenced by two fluids of different origin and composition: fluid inclusions with NaCl, KCl, hematite, and other unidentified daughter minerals represent a hypersaline fluid interpreted to be of magmatic origin, and low-salinity fluids that are assumed to have been derived from sea water (Rytuba et al., 1989).

The formation of the Rodalquilar Au and alunite deposits can be divided in 3 main stages: a first stage based on the formation of the Rodalquilar caldera complex sometime after 11.2 Ma, a second stage of development of a hydrothermal system resulting in high-sulphidation Au mineralization about 10.4 Ma (this event may be further subdivided into an early stage of intense acid sulfate alteration and a main ore stage), and a third stage of supergene acid sulfate alteration between 4 and 3 Ma (Rytuba et al., 1989).

Hydrothermal mineralizations and alterations in the area have characteristics that are typical of epithermal type of mineral deposits (Figure 2.4) (Demoustier et al., 1999). Mineralizations within the Rodalquilar caldera complex are either low-sulphidation (deposits, consisting of Pb-Zn-(Cu-Ag-Au) quartz veins) or high-sulphidation (consisting of alunite veins and, more importantly, Au-(Cu-Te-Sn) chalcidonic quartz veins and hydrothermal breccias) (Carranza et al., 2008) sub-type of epithermal deposits (Arribas et al., 1995). The last is the product of very acidic conditions ( $\text{pH} < 2$  at  $T \approx 250^\circ\text{C}$ ) that occur within sulfate-rich hydrothermal fluid formed by absorption of magmatic vapour (Arribas et al., 1995). Neutralization of the acidic

solution by reaction with the wallrock results in a sequence of alteration zones, outward from the hydrothermal conduit, which is indicative of decreasing acidity and is defined by the presence of alunite, kaolinite, illite, and montmorillonite±chlorite (Steven & Ratté 1960; Fig 2.4 left)

Precious-metal epithermal deposits are associated with intensely hydrothermally altered rocks characterized by a silicic (vuggy silica) central zone, which grades outwards to an advanced argillic (mainly quartz + alunite + kaolinite) zone (being the host of the highest grade gold mineralization in the eastern part of the Lomilla caldera (Arribas et al., 1989)) and then to an argillic (mainly quartz, kaolinite, illite) zone. The base-metal epithermal deposits occur in propylitic (mainly quartz, chlorite, illite) zones peripheral to the areas described above (Figure 2.4-AB) (Arribas et al., 1995).

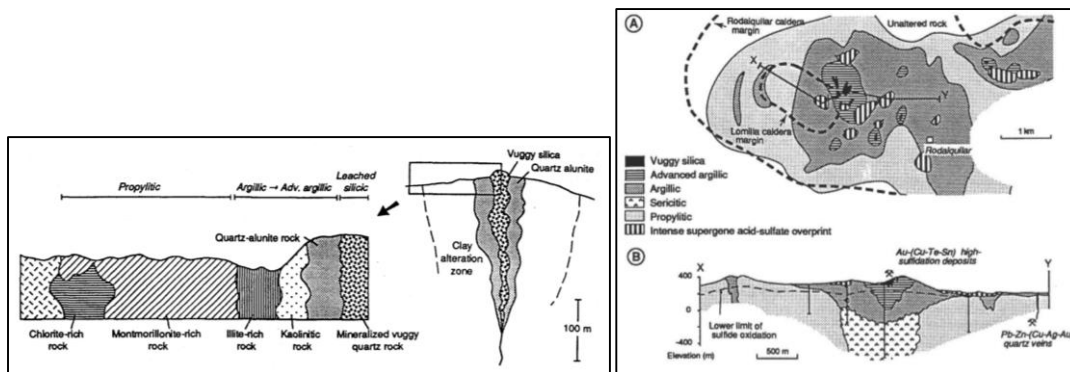


Figure 2.4. (Left figure) Cross-section of alteration zones characteristic of high-sulphidation deposits. Diagram at left shows schematic outward zonation from a subvertical mineralized body, shown at right. (Right figure) Generalized surface alteration map (A) and cross-section (B) of the Rodalquilar HS deposit in the Rodalquilar and Lomilla calderas.

The correct identification and characterization of hydrothermal alteration paragenesis allows constraining the chemical-physical characteristics (i.e., temperature and pH conditions) of the environment in which the hydrothermal alteration developed (Fulginiti, P. 2020).

The main types of hydrothermal alteration stages and minerals assemblage are indicated in figure 2.5, together with their indicative T and pH conditions of formation in table 2.1.

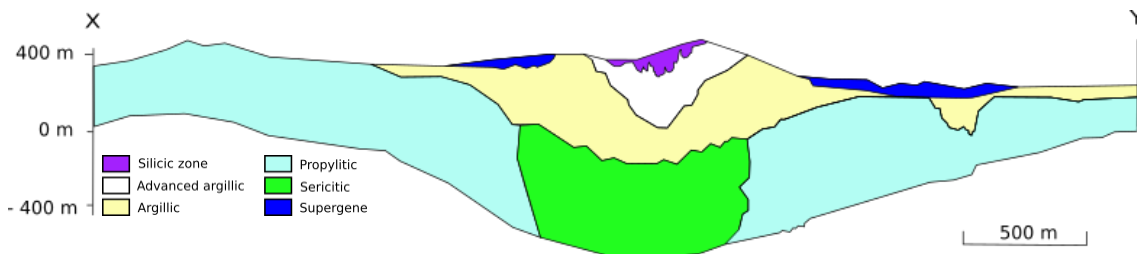


Figure 2.5. Significant mineral assemblage in the alteration zones of the Rodalquilar epithermal system (After Arribas et al., 1995)

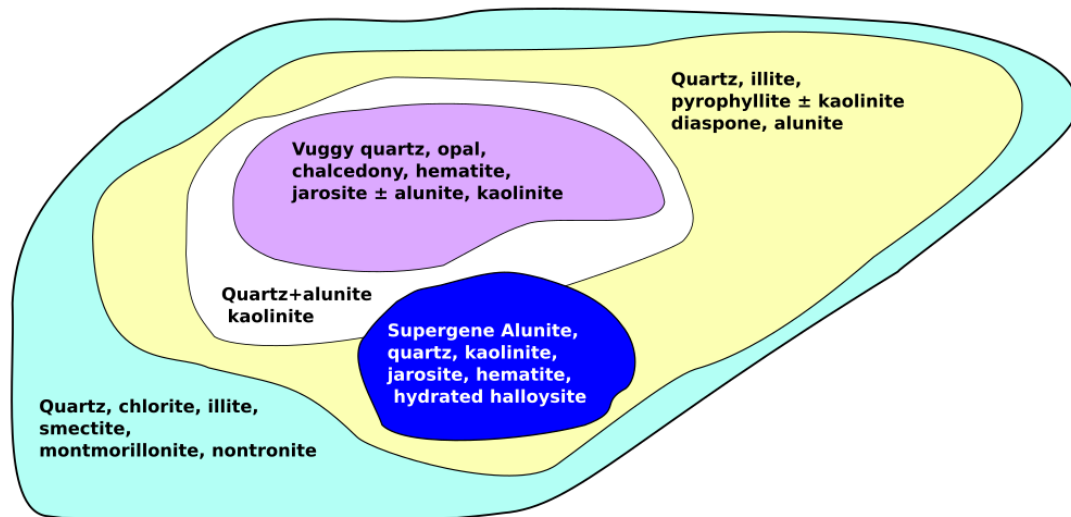


Figure 2.6. Scheme of detailed mineral assemblages in alteration zones in Rodalquilar (Arribas et al., 1995).

Alteration	Occurrence and origin
Sericitic	The temperatures were possibly as high as 300°C
Propylitic	Develops at >240°C deep in the epithermal environment through alteration by near-neutral pH waters (pH 5.5-7)
Argillic	Develops at <180°C on the periphery and in the shallow epithermal environment through alteration by steam-heated CO <sub>2</sub> -rich waters (pH 5.5-7)
Advanced Argillic	Develops at <120°C near the water table and in the shallowest epithermal environment through alteration by steam-heated acid-sulphate waters; locally associated with silica sinter but only in geothermal systems (pH (2-4)
Silicic zone	Develops in an extremely acid environment (pH<2)
Supergene	Develops at <40°C through weathering and oxidation of sulfide-bearing rocks

Table 2.1. Alteration zones present in the area and main characteristics (Madrid et al., 2014, Ylagan et al., 1996).

#### 2.4. Structural geology in Rodalquilar

Fault systems formed during different phases of the caldera cycle control the structural behaviour of ore deposits formed within or near the caldera. Regional faults present prior to caldera formation (phase 1 from section 2.2) may be important in localizing magma emplacement and, after caldera formation, these faults may reactivate caldera-related structures leading to a complex structural evolution of the caldera (Rytuba, J.J., 1994). While ring and radial faults developed during caldera resurgence may also be important in localizing them as in the gold-alunite deposits within Rodalquilar Caldera complex (Rytuba et al., 1990).



Figure 2.7. Map of the Rodalquilar Caldera complex, modified from Rytuba et al., 1990 and Oepen et al., 1989.

During resurgence of the Rodalquilar caldera (phase 3 from section 2.2), ring domes were emplaced along the southern and northern ring fault and a dome formed within the centre (Figure 2.7) (Rytuba, J. J. 1994). Radial faults located within the central dome of the caldera were formed due to the continued resurgence of the caldera. Those faults extended from the structural margin of La Lomilla into the caldera wall were then formed due to the catastrophic venting of the resurgent magma, with eruption of Lázaras ash-flow tuff and the formation of La Lomilla caldera. North-trending faults were formed at the end of the caldera cycle, in response to the renewed movement along the strike-slip Cabo de Gata fault. These faults cut both calderas and caused the reactivation of the North-trending radial faults previously mentioned. The emplacement of a dioritic stock domed and opened the radial and north-trending fault zones (Rytuba et al., 1990). During this magmatic phase, SO<sub>2</sub> degassing from this magma and acid sulphate alteration resulted in development of large zones of vuggy silica enveloped in alunite and kaolinite along the east ring fault, the radial faults, and the north-trending faults in the east wall of the Lomilla caldera (Arribas et al., 1989).

Gold deposits (Au) in Rodalquilar have their origin due to the presence of a shallow dioritic magmatic intrusion (3-4 km) that provided acid hydrothermal fluids (pH<2) rich in SiO<sub>2</sub> and a temperature in between 200 and 400°C. These fluids rich in metals raised to the surface through faults and altered zones when they cooled down the metals they transported precipitated.

Gold was deposited in small veins or disseminated within amorphous silica veins (figure 2.8). These veins have a brecciated aspect and form the fault places through where the hydrothermal fluids circulated.

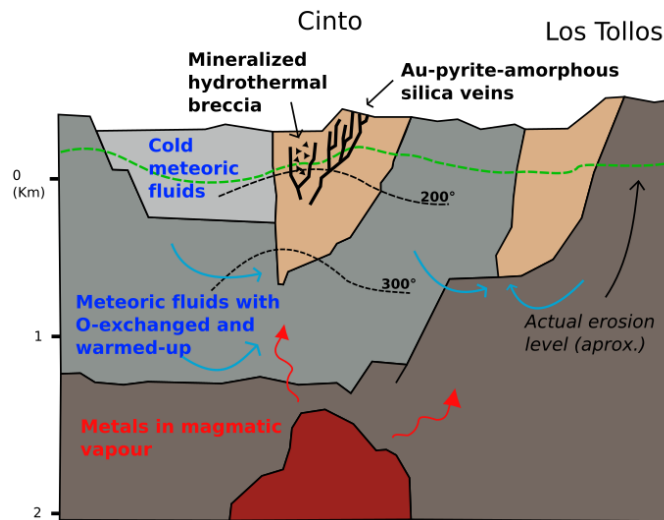


Figure 2.8. Hydrothermal origin of deposits (modified after Arribas et al., 1995).

Epithermal alteration processes in the caldera occurred in two different moments, leading to two different types of deposits: low-sulphidation and high sulphidation (Ágülia et al., 2017).

The gold-alunite deposits (high sulphidation) are the most economically important deposits in the caldera complex (Skillings Mining Review 1988). Altered rocks in the ore zone formed from pervasive acid sulfate alteration and consists of an assemblage of quartz, alunite, kaolinite, jarosite, pyrophyllite and hematite. Along faults the country rock is completely leached and consists of vuggy silica (Rytuba et al., 1990). The most symbolic vein is the so-called vein 340 (Figure 2.9), due to its orientation N340°E, associated with high-sulphidation Au-(Cu-Te-Sn) epithermal processes. This vein was discovered in 1963, producing around 1 Ton of gold with an average grade of 83 g/t (Sintes, 2016). This vein consisted on hydrothermal vein of up to 2 meters thick, located in a North-South fault crossing tuffs and collapse breccias. San Diego gold vein is also an important vein defined by extensive mine workings (Rytuba et al., 1990). It is localized in a ring dome emplaced just north of the south-central margin of the Rodalquilar caldera.

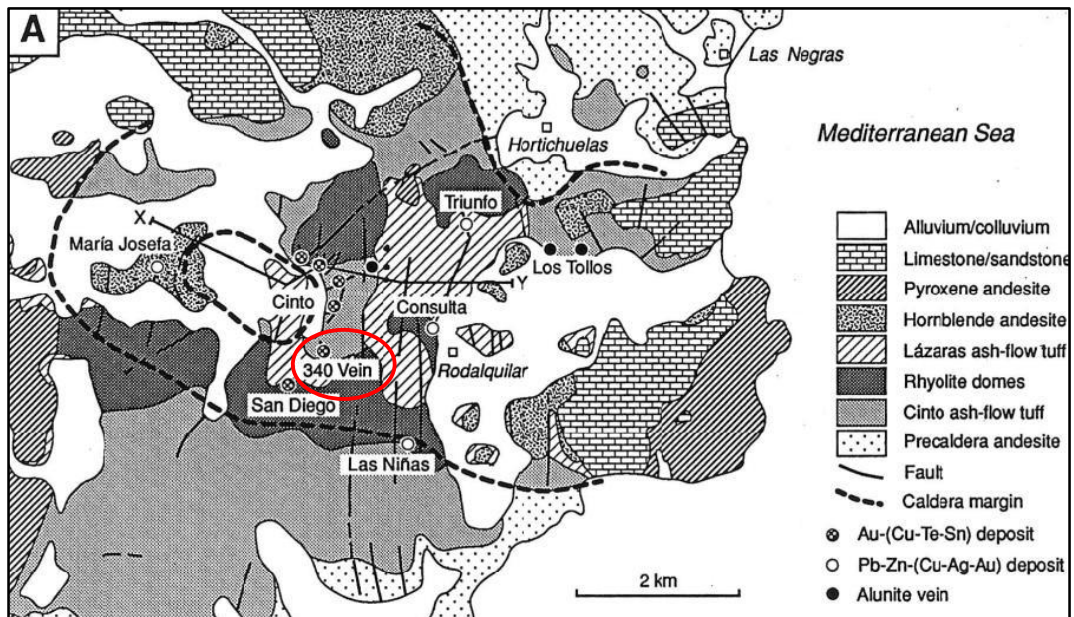


Figure 2.9. Localization of 340 Vein in Rodalquilar (F.Hernandez Ortiz, 2002).

The lead-zinc-silver-gold quartz (low-sulphidation) vein deposits occur along north-south trending faults. The Triunfo vein system is form of individual veins are up to 20 cm wide and occur in a zone about 2 m width that extends for about 0.5 km along its strike of N 3 E. The vein extends northward into the Hortichuela ring dome and altered rocks extend outward from the vein. The Consulta vein system is similar to the Triunfo vein and is characterized by massive bands of galena in a quartz gangue. The vein system extends for about 1.5 km southward from the central part of the Rodalquilar caldera to the south border of the Rodalquilar caldera where it is termed the Las Nifias deposit (Rytuba et al., 1990).

### 3. DATASETS AND METHODS

This first part of this chapter contains information about the data sets: multispectral and hyperspectral imagery, introducing HyMap and PRISMA instruments specifications and products, and geological map and rock-samples used to corroborate results obtained from HyMap and PRISMA.

The second part is focused on research methods: spectroscopy in the laboratory, the creation of the local-spectral library and mineral mapping (SAM).

Imagine processing (chapter 4) is separated from this section since it was considered an extent and important part of the study.

#### 3.1. Datasets

The sources from which information was based and compared were the geological map of Rodalquilar district (escale 1:50.000) from MAGNA 50, combining pages 1046 (Carboneras) and 1060 (Pozo de los Frailes), the alteration map of the Rodalquilar area described by Arribas et al., 1995, two airborne HyMap scenes recorded in 2004 in 126 narrow bands, with a spectral range from 0.45 to 2.84  $\mu\text{m}$ , with a spatial resolution in the range of 3 to 10 m, PRISMA hyperspectral scene recorded in 2004 in ~ 250 bands narrow bands, in a spectral

range of 400 to 2500 nm, at a spatial resolution of 30 m and a panchromatic imagery at a spatial resolution of 5 m, 55 rock samples (17 powder size and 38 VISU size) collected in 2003 and 2004 in the Rodalquilar area during different campaigns performed by ITC staff and students, the USGS spectral library (version 7) and DARWin SP Software Version 1.3.0.0.

### 3.1.2. Spaceborne/airborne imaging spectroscopy.

#### 3.1.2.1. HyMap images

The HyMap<sup>®</sup> sensor is an airborne imaging system developed by Integrated Spectronics, Sydney, Australia, and operated by HyVista Corporation. It consists of sensors located on a fixed wing aircraft typically flown at an altitude of approximately 10.000ft (3000m) above MSL (Corp, H. 2004. HyEurope 2004 Summary Report).

HyMap images are used for Earth resources remote sensing. In essence, the HyMap is an airborne spectrometer that can detect and identify materials by the spectral features contained in the recorded data. The HyMap sensor records 128 spectral bands. However, the delivered data contains 126 since the first and the last band of the first spectrometer are deleted during the pre-processing. It covers the 0.45-2.48  $\mu\text{m}$  wavelength range, including the visible to near-infrared (VNIR) and short wave-infrared (SWIR) regions of the electromagnetic spectrum (Table 3.1). The sensor has 4 spectrometers (VIS, NIR, SWIR1 and SWIR2), each producing 32 spectral bands of imagery. Typically, the spatial resolution achieved with the HyMap is in the range 3x3 to 10x10  $\text{m}^2$ .

Spectral module	Wavelength range	Bandwidth	Spectral sampling
VIS	0.45 – 0.89 $\mu\text{m}$	15 – 16 nm	15 nm
NIR	0.89 – 1.35 $\mu\text{m}$	15 – 16 nm	15 nm
SWIR1	1.40 – 1.80 $\mu\text{m}$	15 – 16 nm	13 nm
SWIR2	1.95 – 2.48 $\mu\text{m}$	18 – 20 nm	17 nm
IFOV: 2.5 mrad along track; 2.0 mrad across track			
FOV: 61.3 degrees (512 px)			
Swath: 2.3 km at 5m IFOV; 4.6 km at 10m IFOV			

IFOV, instantaneous-field-of-view; FOV, fielf-of-view; mrad, milliradian

Table 3.1. HyMap instrument specifications.



Figure 3.1. True colour images of HyMap Cabo de Gata (Black lines in the center, top and bottom of the image is due to the centring and geocorrection of the images)

### 3.1.2.2. PRISMA images

The high-resolution space and spectral satellites have changed the way we consider the environment and the environmental phenomena (Agenzia Spaziale Italiana). This is the case of PRISMA (Hyperspectral Precursor of the Application Mission).

In 2008 PRISMA (PREcursore IperSpettrale della Missione Applicativa) was under development by the Italian Space Agency ASI (Agenzia Spaziale Italiana) and started its journey in space later on March 22<sup>nd</sup>, 2019. It is a medium-resolution hyperspectral image mission and a follow-on project of the previously started HypSEO (Hyperspectral Satellite for Earth Observation) program whose phase B was completed in 2002 and then discontinued. The PRISMA project is conceived as a pre-operational and technology demonstrator mission, focused on the development and delivery of hyperspectral products and the qualification of the hyperspectral payload in space.

PRISMA (the name of the mission and of the sensor are identical) is an advanced hyperspectral instrument including a panchromatic camera at medium resolution. This combination allows the satellite to determine the chemical-physical composition of the objects present on the scene in addition to recognizing their geometric characteristics. The design is based on a pushbroom type observation concept providing hyperspectral imagery (~ 250 bands) at a spatial resolution of 30 m on a swath of 30 km. The spectral resolution is better than 12 nm in a spectral range of 400-2500 nm (VNIR and SWIR regions). In parallel, Pan (Panchromatic) imagery is provided at a spatial resolution of 5 m (Kramer, H., 2002).

Parameter	VNIR channel	SWIR channel	Pan channel
Spectral range	400-1010 nm	920-2505 nm	400-700 nm
Spectral resolution (FWHM)	≤ 12 nm	≤ 12 nm	-
Spectral bands	66	171	1
Swath width	30 km (FOV = 2.77°)		
Spatial resolution	30 m		5 m
Spatial detector pixels		1000 x 256 with 30 μm pitch	6000
IFOV	48.34 μrad		

Table 3.2. Overview of PRISMA instrument parameters.

All products are in HD5-EOS format and include HYP data cube and + PAN image + metadata. These products are divided in four levels: Level 1, corresponding to Top-of-Atmosphere Radiance radiometrically corrected and calibrated in physical units (including cloud mask, sun-glint mask, classification mask, calibration and characterization data); Level 2B, which is geolocated at Bottom-of-Atmosphere Radiance; Level 2C, geolocated at Bottom-of-Atmosphere Reflectance (including aerosol characterization product (VNIR), water vapour map product (HYP) and cloud characterization); and Level 2D, which is the geocoded version of the level 2C products.

The general scheme of Level 2 processing is illustrated in Figure 3.2. The processing steps which allow the transformation from Top-of-Atmosphere spectral radiance (Level 1) to at-surface reflectance (Level 2c) are generally called atmospheric correction. The processing step which brings to the level 2d is identified as geocoding.

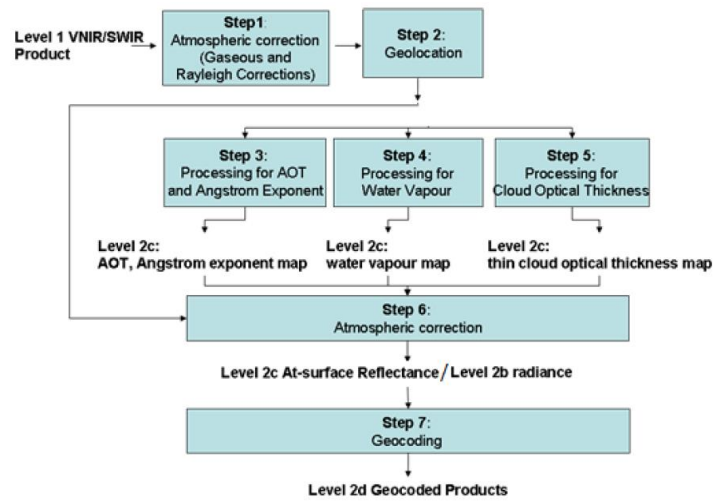
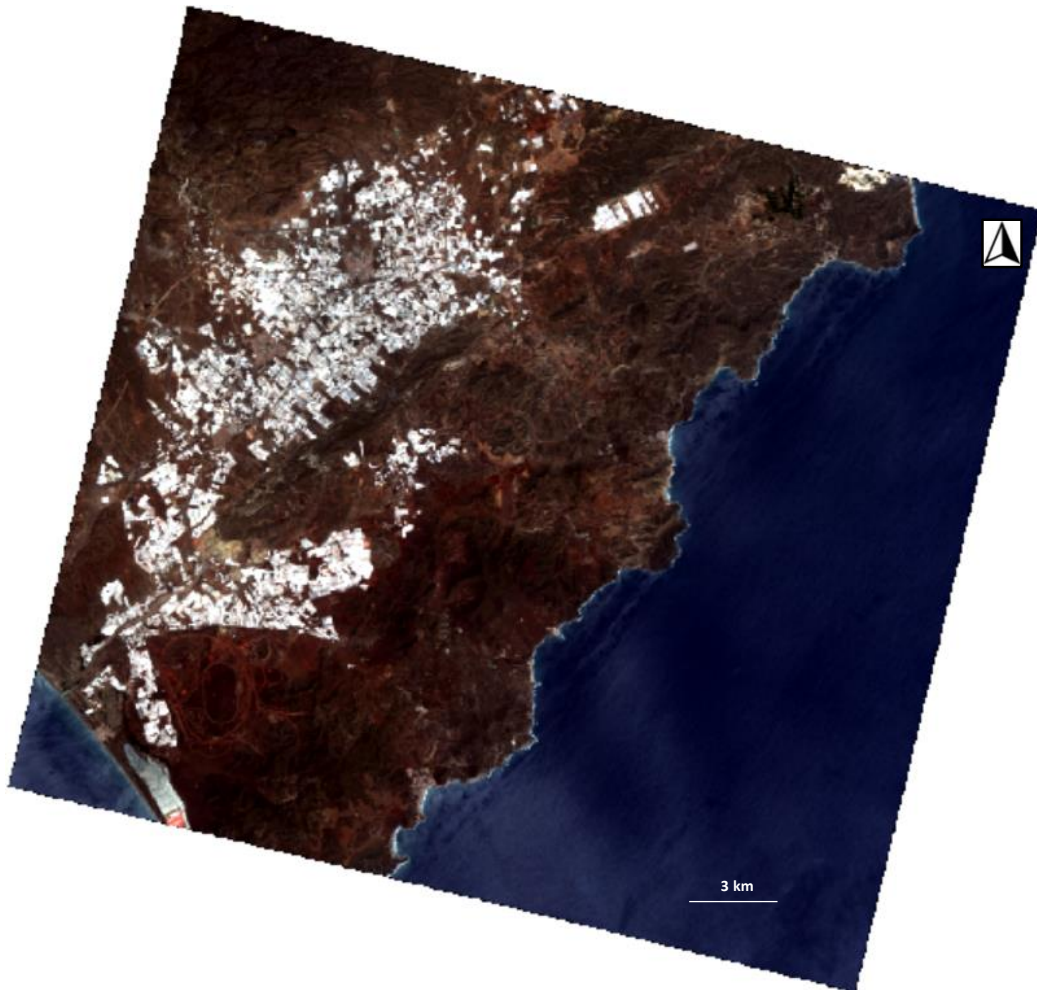


Figure 3.2. General scheme of Level 2 processing.

For this project, image acquisition from PRISMA was done of Level 2D products, so that the information from the surface does not need to be corrected for atmosphere interactions since it is geocoded imagery processed into reflectance (Figure 3.3).



*Figure 3.3. PRISMA satellite image of Rodalquilar.*

### 3.1.3. Geological map IGME image

The National Geological Map (MAGNA) was realized between 1972 and 2003 by the Geologic and Miner Institute of Spain. This map (figure 3.4) represents the constitution of materials (rocks and sediments) that appear in the terrestrial surface, their spatial distribution and the geometric relationships between the different cartographic units.

A cartographic unit is the aggrupation of one or more lithologies with a common range of age, that has a representation in the map in a defined scale or resolution. Each cartographic unit, just as the different geological structures, are represented in the map with its own symbology. The representation of these units, on the base of the topographical map, provides in a certain way tridimensional information that is completed with other geological data as geological sections, stratigraphic sections, drilling exploration, etc.

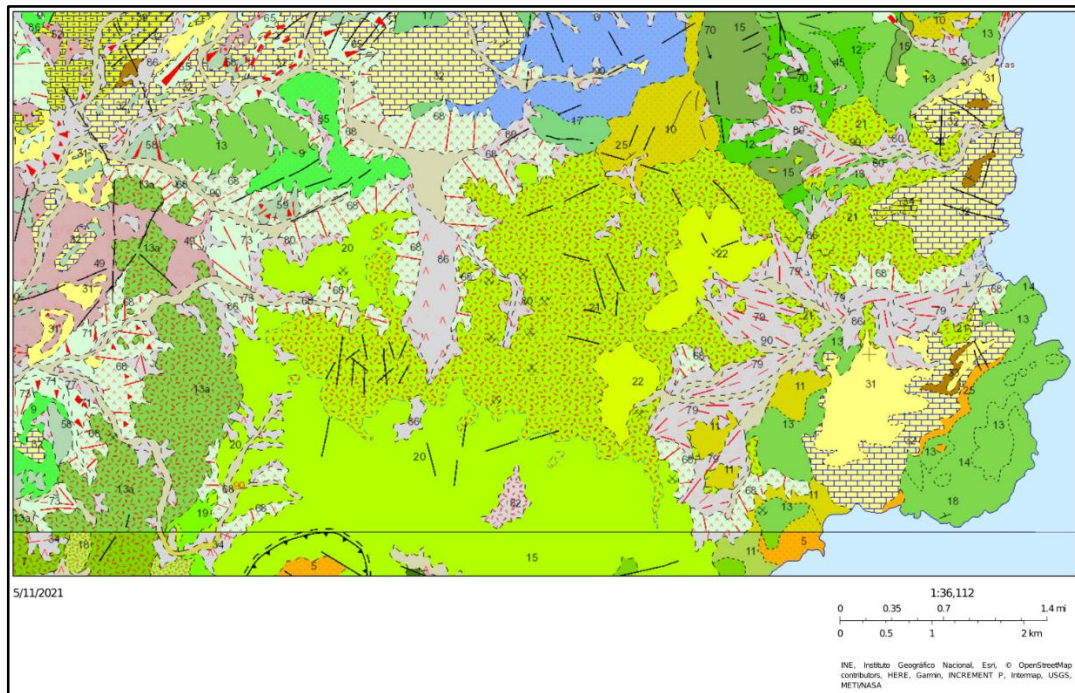


*Figure 3.4. Geological map of the area scale 1:50.000 MAGNA*

#### 3.1.4. Rock samples

More than 200 rocks are available from the ITC. These rock samples have been collected by ITC students during several fieldtrips to the Caldera de Rodalquilar Complex. Among these samples, a total of 52 samples were selected for spectral analysis, being 16 of them powder samples. This selection was based on location of these rocks along two profiles previously drawn cross-cutting both hydrothermal alteration zones, Cerro del Cinto to the West and Los Tollos to the East (Figure 3.5). The distance of these rock samples from the profiles was calculated using ArcGis Pro applying a buffer of ~ 200 meters, although only a small amount of samples fell down in such a distance since these profiles were drawn non-straight, following these rock samples while cross-cutting the most interesting hydrothermal areas. The geographic location of the samples is presented in Appendix 2.

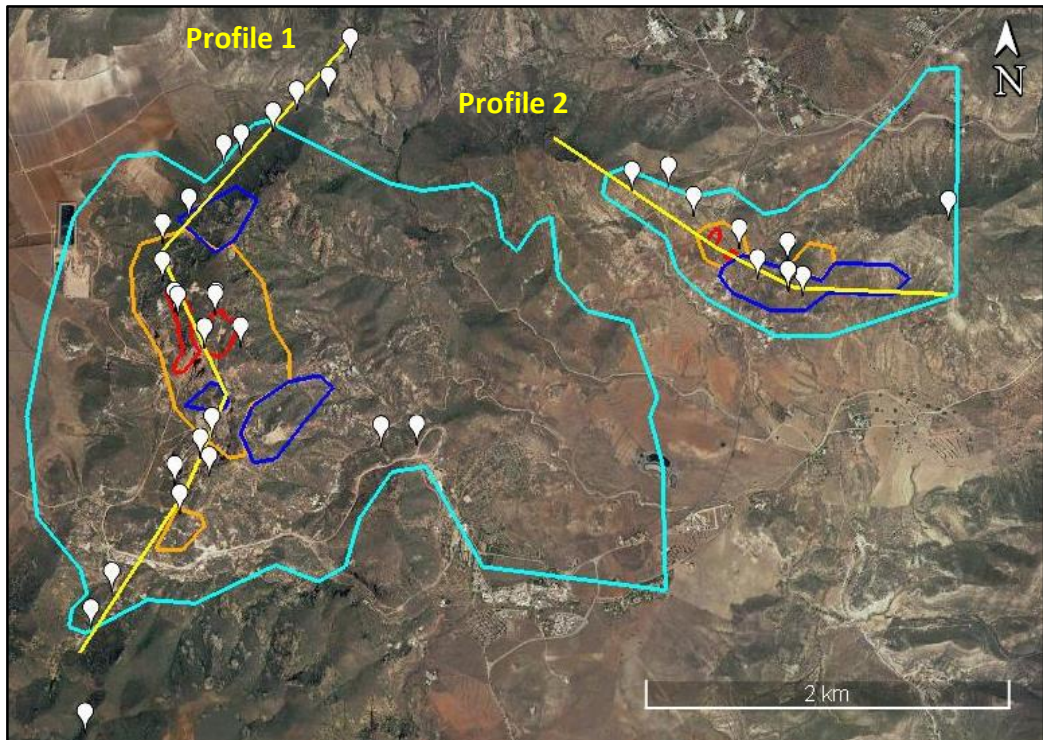


Figure 3.5. Setting of the two cross-sections (yellow lines) drawn along the two different hydrothermal alteration zones (Arribas et al., 1995).

### 3.2. Research methods

#### 3.2.1. Spectroscopy in the laboratory

Laboratory spectroscopy is a technique that has been used since the nineties, consisting on the study of the absorption and emission of light and other radiation by matter, as related to the dependence of these processes on the wavelength of the radiation. More recently, the definition has been expanded to include the study of the interactions between particles such as electrons, protons and ions, as well as their interaction with other particles as a function of their collision energy (Graybeal et al., 2021).

Production and analysis of a spectrum require the following: (1) a source of light (or other electromagnetic radiation), (2) a disperser to separate the light into its component wavelengths, and (3) a detector to sense the presence of light after dispersion (Figure 3.6). The apparatus used is called Spectral Evolution PSR+spectrometer (Table 3.7). Spectra can be obtained rather in the form of emission spectra, which show one or more bright lines or bands on a dark background, or absorption spectra, which have a continuously bright background except for one or more dark lines.

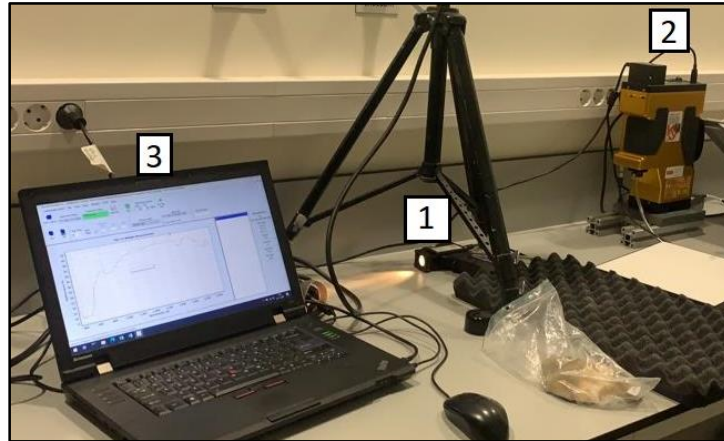


Figure 3.6. Laboratory set up for spectrum measurement. (1) Source of light (2) Spectrometer (3) Spectrum Software analyzer.

The method used in this project is absorption spectroscopy, which measures the loss of electromagnetic energy after it illuminated the sample under study.

Ground spectroscopic measurements in the SWIR range were the sources of information. These measurements were taken in the laboratory with the purpose of affording the identification of features that characterize those minerals considered as path finders. The data was collected at continuous and high spectral resolution.

PSR+ 3500 Specifications	
Spectral Range	350-2500nm
Spectral Resolution—FWHM (Full Width at Half Maximum)	2.8nm @ 700nm 8nm @ 1500nm 6nm @ 2100nm
Si Detector	512 element Si photodiode array (350-1000nm)
InGaAs Detectors (cooled)	256 element extended wavelength photodiode array (970-1910nm) 256 element extended wavelength photodiode array 1900-2500nm
FOV Options (direct mount)	4°, 8°, or 14° lens, 25° fiber optic, diffuser, integrating sphere
Fiber Mount Options	1, 2, 3, 4, 5, 8 and 10° Lenses
Noise Equivalence Radiance (4° lens)	0.5x10 <sup>-9</sup> W/cm <sup>2</sup> /nm/sr @400nm 0.8x10 <sup>-9</sup> W/cm <sup>2</sup> /nm/sr @1500nm 1.0x10 <sup>-9</sup> W/cm <sup>2</sup> /nm/sr @2100nm
Max Radiance @ 700nm (4° lens)	1.5x10 <sup>-4</sup> W/cm <sup>2</sup> /nm/sr
Minimum Scan Speed	100 milliseconds
Wavelength Reproducibility	0.1nm
Wavelength Accuracy	±0.5 bandwidth
Communications Interface	USB or Class I Bluetooth - laptop or PDA compatible
Size	8.5" x 11.5" x 3.25"
Tripod Mounting	2 each ¼-20 mounting holes provided
Weight	7.6 lbs (3.5 kg)
Batteries	Lithium ion; 7.4V; 7200mAh; 400g/battery
Battery Operation	Removable battery; typically up to 4 hour operation/battery (2 provided)
On Board Memory	Storage of 1000 spectra

Figure 3.7. PSR +3500 Instrument specifications.

### 3.2.2. Creation of local spectral library

Spectral libraries contain sets of endmembers. Endmembers are detailed spectra, measured under controlled conditions in the laboratory or field, representing certain materials (minerals, vegetation species, man-made materials etc.). For minerals the spectra are most often collected from air-dried and grinded samples. Sets of these endmembers, contained in the spectral libraries, are then used as reference spectra in

algorithms like Spectral Angle Mapping (SAM) or Linear Spectral Unmixing (LSU) (Wur, J. n.d.).

The advantage of spectral libraries created in a laboratory is that it is possible to control the conditions (humidity, weather state etc.) in which measurements are taken, allowing for more “pure” spectra to be measured. Water absorption features are lacking in most library spectra because the samples of which the spectra are measured have been dried and will thus not show the typical water absorption bands.

The disadvantage of a spectral library like this one is that the spectra are acquired from air-dry, grained, fresh samples. Such a sample preparation may be necessary to optimally determine the pure spectrum of this mineral and the location of the absorption bands, but the spectra are less suitable for comparison with real images spectra. Real image spectra always provide information of weathered minerals, sometimes covered by a surface seal or crust, and the soil surface in the real world is usually not oven-dry. The spectral library created was based originally in the VISU interpretation of the rock samples collected and studied in the laboratory (Wur, J. n.d.).

The first step was classifying the rock samples in the different alteration zones based on their VISU appearance. For each zone, specific characteristics were assigned so that a first interpretation of these rocks was feasible.

In the vuggy silica alteration zone, the common characteristics were the presence of veins and pores. These rocks were quite oxidized, there were no minerals left from the original rock and distinguished by the presence of phenocryst of silica.

The supergene alteration occurs creating an overprinted pattern with the primary mineralization of the advanced argillic zone. The rock samples within this alteration zone are characterized by a very fine grain and a homogeneous pattern.

The advanced alteration zone consists of rock samples with a certain alteration but they also contain some phenocrystals from the original rock. Some veins are also common and the grains vary from fine to very fine.

Distinguishing between advanced and intermediate alteration zone by just doing VISU interpretation is to some extent a challenging task. However, the closer the rock samples are to the prophylic zone, the more amount of phenocrystals from the original rock are present.

Rocks belonging to the prophylic zone are those that are barely altered and that still conserve a large part of the phenocrystals from the original rock.

The following step was the spectral interpretation, which also facilitated the grouping of samples in different alteration zones. Each alteration zone has specific spectral signatures as discussed in chapter 4.3.2. For each group, a rock sample of each significant mineral with the purest spectra defining this group was assigned.

### 3.3. Mineral mapping

Spectral Angle Mapper (SAM) method was applied to this study to produce mineral maps of both HyMap images (Cabo de Gata 2 & 3) and PRISMA image. Spectral Angle Mapper is a physically-based spectral classification that uses an n-Dimensional angle to match

pixels to reference spectra where  $n$  is the number of bands in the image. The algorithm determines the spectral similarity between an image spectrum (representing an unknown material) and a reference spectrum (representing a known material) by calculating the angle between the spectra, treating them as vectors in  $n$ -dimensional spectral space, where  $n$  is the number of bands. This technique, when used on calibrated reflectance data, is relatively insensitive to illumination and albedo effects. SAM compares the angle between the endmember spectrum vector and each pixel vector in  $n$ -D space. Smaller angles represent closer matches to the reference spectrum (Kruse et al., 1993).

## 4. IMAGE PROCESSING

This chapter introduces the steps of the calculations applied in HyMap and PRISMA images, including image corrections, calculation of NDVI, application of vegetation mask, creation of local spectral library, endmember extraction and mineral mapping.

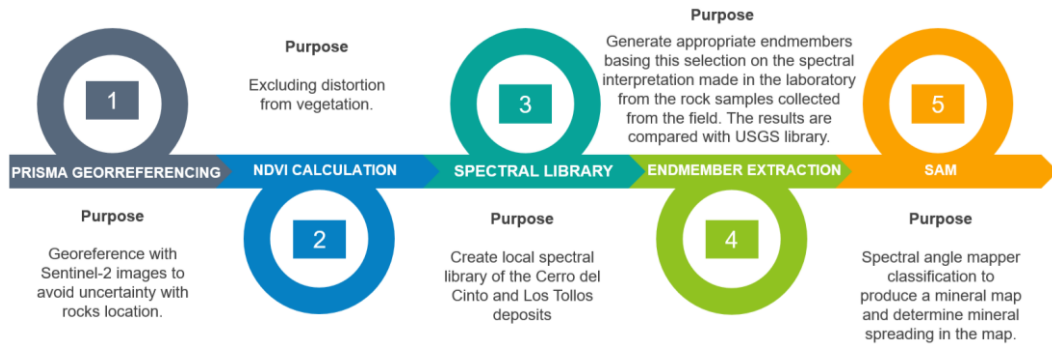


Figure 4.1. Flowchart of the followed steps.

### 4.1. Image processing and interpretation

Every object or material – whether solid, liquid, or gas – reflects or emits electromagnetic energy in a distinctive way. Our eyes can only perceive electromagnetic energy in shades of red, green and blue (RGB)- this is called the visible spectrum. Spectral image analysis utilizes more bands from the electromagnetic spectrum to extract distinct spectral characteristics and derive valuable information.

Spectral data is broken out into two categories, multispectral imagery (which generally has fewer, broader bands) and hyperspectral imagery (which consists of more, narrower bands) (Figure 4.2). Hyperspectral sensors are not being widely used for mapping land resources (Harsanyi and Chang, 1994) such as multispectral datasets have simple spectral information, which makes the precise identification of similar spectral features difficult. Unfortunately, due to internal relations between the spatial and spectral sensitivities of sensors, conventional hyperspectral images generally suffer from low spatial resolution as compared to multispectral or panchromatic images (Garg, 2020), reason why in this study both multispectral and hyperspectral images were compared with other sources of information to verify results.

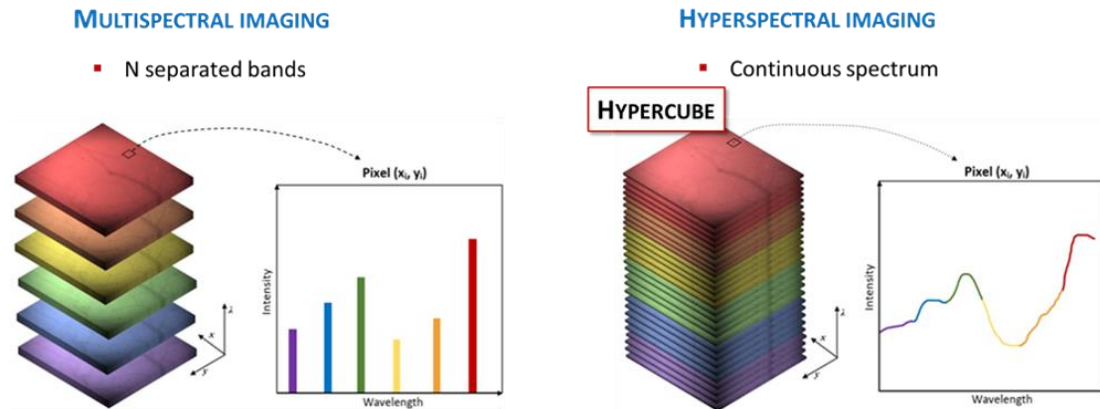


Figure 4.2. Differences between multispectral (left) imaging, only providing discrete and discontinuous portions of the spectral range, and hyperspectral (right) imaging, creating the hypercube using a large number of contiguous spectral bands. The result gives a complete spectrum for each pixel  $(x_i, y_i)$ . Adapted from Luca Giannoni et al., 2018 J. Opt. 20 044009.

For spectral analysis ENVI software is used. ENVI software package was released in 1994 developed by L3Harris Geospatial Remote Sensing company (L3Harris Geospatial.) ENVI is the leader in spectral image processing with the top tools to analyse multi and hyperspectral data including spectral target detection and identification. These tools are based on established, scientific methods for spectral analysis – using pixel responses at different wavelengths to obtain information about the materials within each pixel.

#### 4.2. Image corrections

As mentioned in 3.1.2.2, the image used from PRISMA portal is geocoded. In spite that, the image positions had ~200m offset. Hence, before applying any calculation, HyMap and PRISMA were georeferenced using QGIS 10.3.7. To avoid inaccuracy, Sentinel-2 image was settled as reference to relocate these maps.

#### 4.3. Masking vegetation using spectral indices

Although the area is well exposed and the vegetation cover is poor, the area cannot be considered bare from a remote sensing perspective, thus it is necessary to filter out elements in the image that can distort the outcome of the upcoming analysis, since this obscures the underlying surface area and when the analysis is performed information from the pixels with vegetation can skewer the final result.

As observed from field photographs (Figure 4.3) vegetation cover, mainly grass, palm shrub, Esparto grass, Spanish lavender, Olive trees and Cornicabras (Denver, P. n.d.). Cerro del Cinto- (short route)), is present in the area. This also manifests with false composite images or by computation of NDVI indices (Normalized Difference Vegetation Index).

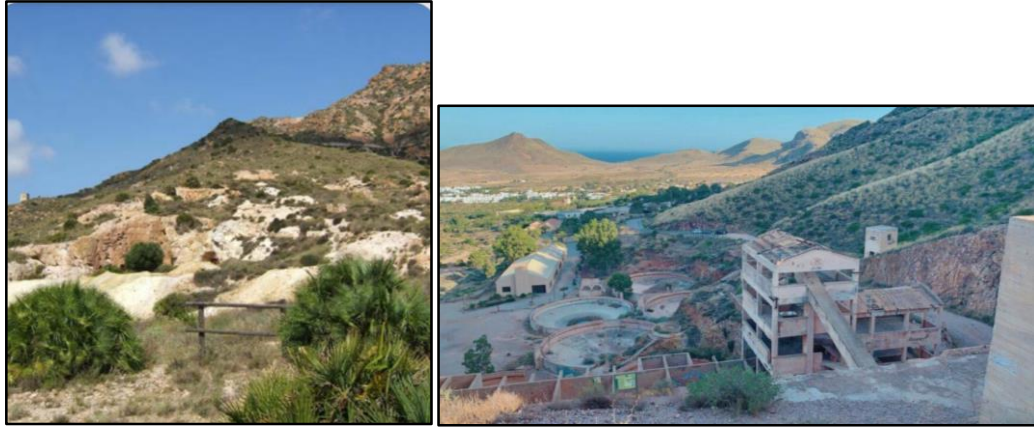


Figure 4.3. Typical vegetation cover of the Rodalquilar area (Environment and Water Agency and Mountain Federation of Andalucía).

Green vegetation reflectance shows the two characteristic peaks in the visible part due to chlorophyll absorption and a strong reflectance mainly in the Near-Infrared due to spongy mesophyll. The other three absorptions located around 1.5, 2.0 and 2.5 are due to water absorptions (figure 4.4).

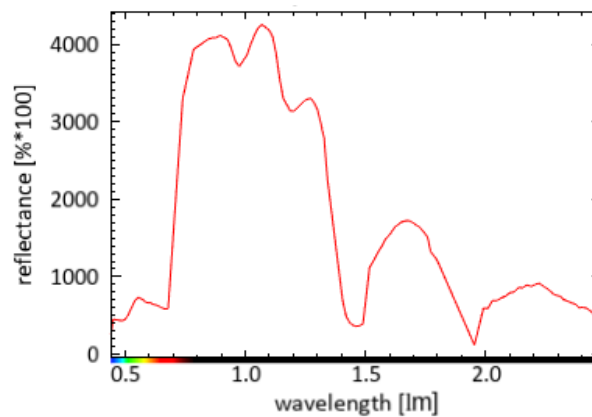


Figure 4.4. Field reflectance spectrum of vegetation in HyMap images.

Spectral vegetation indices are remote sensing image analysis methods aiming at enhancing the spectral contribution of green vegetation while simultaneously minimizing the contribution from soil background, variation of solar irradiance, sun angle and atmosphere. Spectral vegetation indices transform the axes of the multi-dimensional by rotation or ratioing. Well-known spectral vegetation indices are the NDVI: Normalized Difference Vegetation Index (Tucker et al., 1979), SAVI: Soil Adjusted Vegetation Index (Huete, 1998) and the TasCap: Tasselled Cap transformation (Kauth et al., 1976).

In this study, masking vegetation is performed by the use of NDVI. This operation returns a map of the area where the pixels are assigned a value between -1 and 1. The higher is this value, the higher is the probability that it corresponds to green vegetation.

#### 4.4. Endmember extraction from HyMap and PRISMA images

The method used for endmembers extraction will be by simply selecting them from the satellite image using the spectral signature of the ground cover considered (Bierwith, 1990).

Endmembers spectra must have recognizable characteristics in the scene and must be significant for the user, since they constitute abstractions of real objects that have the same or similar properties. In many cases, the number of components and its composition are unknown, and the problem is to unmix spectrally the data in a number supported by the data dimension.

#### 4.4.1. Spectroscopy studies in Rodalquilar

The Rodalquilar Caldera complex is located in the most arid region of Europe with sparse vegetation cover, which enables an open view of the area due to its good exposure and makes possible to study and analyze the hydrothermal system at the earth surface using Remote Sensing and Spectroscopy techniques. Various of the hydrothermal altered minerals have unique spectral signatures and absorption bands, especially in shortwave infrared, making it possible to use these techniques to identify minerals and the distribution of the hydrothermal alteration mineralogy.

Previous studies have evaluated the use of Spectroscopy and Remote Sensing techniques to map and identify minerals delineation in alteration zones. In 1989 (and later in 1995) Arribas et al. already utilized Remote Sensing by using Landsat-5 thematic mapper data as a tool in the initial stages of the study of alteration zones. Afterwards in 1996 Ferrier and Wadge used AVIRIS imaging spectrometer data to detect the hydrothermal alteration mineralogy mapped using traditional ground-based techniques at Rodalquilar. In 2008 Choe et al. used combined geochemistry, field spectroscopy and hyperspectral remote sensing (HyMap image) to map heavy metal pollution. Later in 2009 a study by Bendini et al. was published in which HyMap imaging spectrometer data was also used to map mineralogy in the Rodalquilar caldera applying MESMA (Multiple Endmember Spectral Mixture Analysis) to analyse SWIR imaging spectrometer data. More recent studies have used HyMap imagery in this area, as Vries et al. 2013, applying spectral angle mapping (SAM) operation for geologic interpretation and gypsum variation detection, or Van der Meer et al. 2018, using two approaches, "Wavelength Mapper" and "QuanTools", to derive mineral information based on absorption feature parameters, to compare the results of these two methods and to apply them to mapping of an epithermal system.

#### 4.4.2. Spectral characteristics of the high sulfidation epithermal system

High sulphidation epithermal systems are characterized by alteration zones dominated by advanced argillic minerals, formed from acidic hydrothermal fluids.

A brief description of mineralization and alteration zones is given bellow based on Arribas et al., 1995. The clay assemblage and the zonation reflects decreasing temperatures and acidity outward from the fluid conduits, from an intensely leached residual **silica and alunite** in the center through to **alunite-diaspore-pyrophyllite-dickite** and sometimes **sericite** assemblages outward. Before the argillic assemblage a **kaolinite-dickite-pyrophyllite** assemblage can also be present as an intermediate argillic zone. Moving

outwards of the alteration system there is a propylitic alteration zone dominated by **epidote-chlorite-carbonate-albite and pyrite**.

SILICA	SUPERGENE	ADVANCED ARGILLIC		INTERMEDIATE ARGILLIC		ARGILLIC	PROPYLITIC
		Center	Outwards	Close to adv.argillic	Close to argillic		
Chalcedony, opal, hematite, jarosite. Local alunite and kaolinite	Quartz, crystalline kaolinite, jarosite, alunite, hematite and hydrated halloysite	Quartz, alunite and some kaolinite	Quartz, kaolinite, illite, illite-smectite	Quartz and kaolinite	Illite-smectite, illite	Illite, quartz and pyrophyllite. Rare kaolinite, diaspore and alunite	Quartz, chlorite, illite, smectite, hematite, montmorillonite and nontronite
		Variable amount of alunite, kaolinite-dickite, pyrite, pyrophyllite, illite		Minor alunite, pyrophyllite and diaspore			

Table 4.1. Minerals association based on literature (modified after Arribas et al., 1995).

The silicic zone is dominated by vuggy silica formed by extreme leaching of the original rock. According to Hedenquist et al., 1988, the acidity for leaching the wallrock must have been connected with volcanogenic activity because geothermal acid sulfate fluids do not have sufficient hydrolyzing capacity. This observation supports the assumption that magmatogenic fluids involved in the fluid system at Rodalquilar were acid (Fulginiti, 2020). It is characterized by the presence of mainly quartz (featureless), chalcedony, opal and jarosite. Also local alunite and kaolinite is present in this alteration zone. The quantity of silica depends on the composition of the original rock.

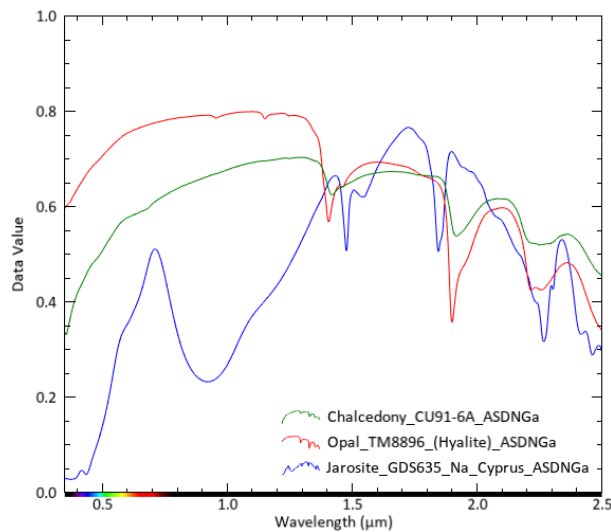


Figure 4.5. Reflectance spectra from the silicic alteration zone in the visible and SWIR wavelength range (source USGS spectral library).

The main differences between chalcedony and opal in SWIR range are the small absorption features at 1.5 µm and 1.95 µm present in opal, which are missing in the spectra of chalcedony.

Jarosite,  $\text{KFe}_3(\text{SO}_4)_2(\text{OH})_6$ . It has three diagnostic absorptions, two in between 1400 and 1600nm and the third one around 1844-1855nm. The 2206 and 2265 absorptions usually persist in mixtures.

The advanced argillic zone is dominated basically by quartz with alunite grading outwards to a zone of quartz with by kaolinite, where illite and illite-smectite are increasingly abundant. There is also some minor dickite and pyrophyllite.

Zoning of the advanced argillic minerals can provide important information for vectoring toward the center of the alteration system.

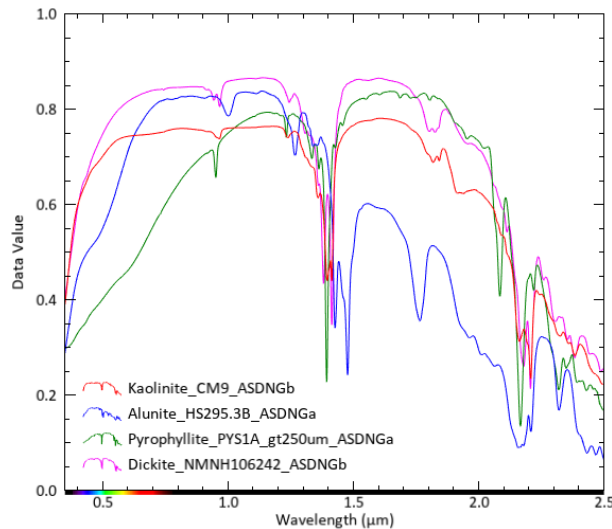


Figure 4.6. Reflectance spectra from the advanced argillic alteration zone in the visible and SWIR wavelength range (Source USGS spectral library).

Dickite,  $\text{Al}_2\text{Si}_2\text{O}_5(\text{OH})_4$ . It has a diagnostic doublet around 1400 associated with  $\text{OH}^-$ , and another one around 2200 associated with  $\text{AlOH}$ . It can be distinguished with Kaolinite looking at the positions and intensities of these doublets. The absorption between 2300 and 2400nm persists in mixed spectra (Pontual et al., 1997).

Alunite, a sulphate mineral  $[(\text{K},\text{Na})\text{Al}_3(\text{SO}_4)_2(\text{OH})_6]$ , is characteristic for the advanced argillic alteration zone of high-sulfidation epithermal gold deposits (M. Tun, et al., 2015). Alunite has a diagnostic doublet absorption at 1470 and 1420nm, which may vary with composition (i.e. Na:K) due to overtone and combination tones of the fundamental  $\text{OH}$ -stretching mode. It also has a diagnostic intense feature near 1770nm due to a combination of the  $\text{OH}$ -bond fundamental stretch with the first overtone of the  $\text{Al-OH}$  bend (Hunt and Ashley, 1979). Another absorption at 2160nm characterizes alunite, which may be modified in mixtures with pyrophyllite, kaolinite and dickite. This feature is due to the  $\text{OH}$ -bond fundamental stretch with the  $\text{Al-OH}$  fundamental bending mode.

Kaolinite, a clay mineral  $[\text{Al}_2\text{Si}_2\text{O}_5(\text{OH})_4]$ , occurs together with alunite in the advanced argillic alteration zone, and is especially characteristic for the intermediate argillic alteration zone of epithermal gold deposits (M. Tun, et al., 2015). It has a characteristic doublet absorption feature around 1400nm due to combination tones of the fundamental  $\text{OH}$ -stretching mode (e.g., Hunt, 1979). The second characteristic doublet occurs at the diagnostic  $\text{Al-OH}$  absorption feature 2200 and 2160 nm. This absorption may be seen as an inflexion or weak absorption in poorly crystalline kaolinite (as, for example, at supergene alteration zone) and mixtures (Pontual et al., 2012). Characteristic 3 absorptions of kaolinite spectra between 2300 and 2400nm. This absorption persists in mixed spectra.

Pyrophyllite,  $\text{Al}_2\text{Si}_4\text{O}_{10}(\text{OH})_2$ . Pyrophyllite has a single sharp absorption around 1396nm. Between 2100 and 2200nm it has a diagnostic absorption and it also contains two absorptions, one in between 2000-2100 and the second one around 2319nm, that persist in mixtures.

Supergene alteration zone occurs creating an overprinted pattern with the primary mineralization of the advanced argillic zone. This zone is characterized by alunite, halloysite, kaolinite, jarosite and amorphous silica mineral. They are formed due to weathering or low-temperature hydrothermal alteration of the primary mineralization (a mineralization form due to high-temperature hydrothermal fluids circulation), thus it is common to find poorly crystalline kaolinite and hydrated halloysite indicating this low-temperature hydrothermal fluids (Abera, 2020).

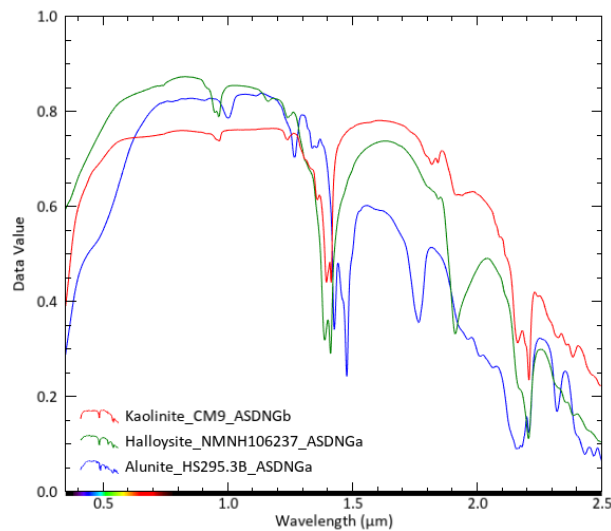


Figure 4.7. Reflectance spectra from the supergene alteration zone in the visible and SWIR wavelength range (Source USGS spectral library).

Halloysite,  $\text{Al}_2\text{Si}_2\text{O}_5(\text{OH})_4$ . It has a diagnostic doublet at 1400nm, which width increases in hydrated Halloysite (note the lack of minor absorptions here compared to Kaolinite). Around 1900 nm it has a water feature which increases in intensity in the hydrated halloysites. The second diagnostic feature occurs in between 2100 and 2200nm, it has similar wavelengths with kaolinite but typically weaker 2166nm absorption relative to the 2206nm absorption.

The intermediate argillic zone is dominated by quartz, kaolinite (near the advanced argillic zone), illite, illite-smectite (in the outer zone, closer to propylitic halo). The assemblage of minerals varies through the alteration zone. For example, near the advanced argillic zone kaolinite-dickite are more abundant, but closer to the propylitic zone illite-smectite become more dominant. There is also minor alunite, pyrophyllite and diaspore (Arribas et al., 1995).

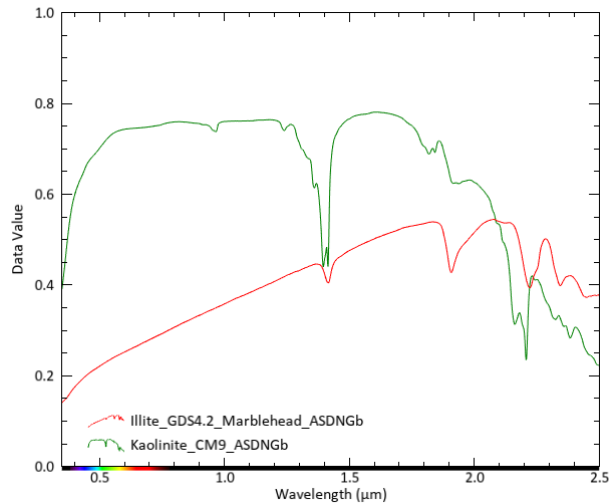


Figure 4.8. Reflectance spectra from the intermediate argillic alteration zone in the visible and SWIR wavelength range (Source USGS spectral library).

Illite,  $[K, H_3O](Al, Mg, Fe)_2(Si, Al)_4O_{10}[(OH)_2, (H_2O)]$ . It has a deep absorption feature at 1900nm due to molecular water within its crystal lattice (Pontual et al. 1997). It has a diagnostic single sharp absorption feature from 2180 to 2228nm which may vary depending on composition. It shows water absorption feature around 1910nm and hydroxyl absorption around 1410nm.

Illite-Smectite,  $(K, H_3O)(Al, Mg, Fe)_2(Si, Al)_4O_{10}$  and  $Ca, Na, H)(Al, Mg, Fe, Zn)_2(Si, Al)_4O_{10}(OH)_2$ . It is not possible to distinguish mixed-layer illite-smectite clays from mixtures of discrete illite and smectite using spectral analysis (Figure 4.9). This is because in both cases the spectra represent mixtures of the two clays. The illite-smectites have a diagnostic AOH absorption between 2180-2228nm. They also have two important and diagnostic absorptions near 2344nm and 2440nm, also associated with AOH absorption. Smectite spectrum is dominated by water absorption near 1400 and 1900nm.

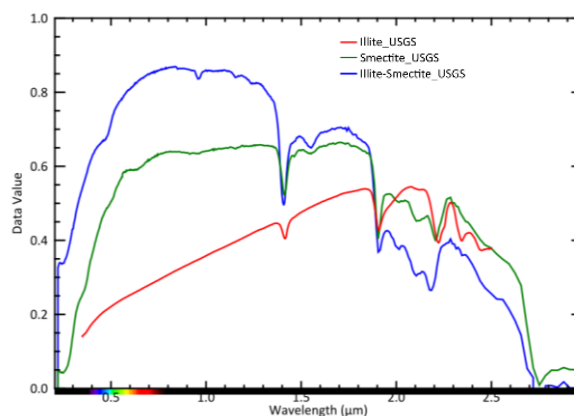


Figure 4.9. Reflectance spectra of illite-smectite, illite and smectite in the visible and SWIR wavelength range (Source USGS spectral library).

The mineralogy of the argillic altered zone is simple and consists mainly on quartz and pyrite (which are featureless in the visible and SWIR wavelength rang) and illite, described already in the advanced argillic zone section (Figure 4.7). There is also some rare kaolinite, diaspore and alunite.

Argillically altered rocks grade into a propylitic assemblage that consists of quartz, montmorillonite, nontronite, chlorite, illite, smectite and goethite. The chemical composition of propylitically altered rocks is relatively unchanged compared to the unaltered rocks within the caldera.

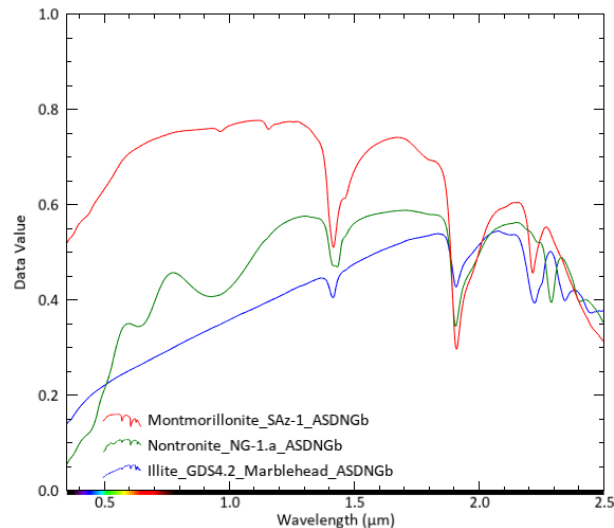


Figure 4.10. Reflectance spectra from the propylitic alteration zone in the visible and SWIR wavelength range (Source USGS spectral library).

Montmorillonite,  $(\text{Na,Ca})_{0,3}(\text{Al,Mg})_2\text{Si}_4\text{O}_{10}(\text{OH})_2 \cdot n\text{H}_2\text{O}$ . It has two deep water absorptions (asymmetric shape), one around 1400 nm and another one at 1900 nm. It has a single absorption that may vary the wavelength from 2205-2212 nm.

Nontronite,  $\text{Na}_{0,3}\text{Fe}_2((\text{Si,Al})_4\text{O}_{10})(\text{OH})_2 \cdot n\text{H}_2\text{O}$ . It has two water that directly overlap the montmorillonite water absorption bands. However, nontronite has two diagnostic absorptions near 2300nm and 2400 nm which discriminate from montmorillonite.

#### 4.3.3. Mineral mapping

Spectral Angle Mapper (SAM) method was applied to this study to produce mineral maps of both HyMap images (Cabo de Gata 2 & 3) and PRISMA image. Spectral Angle Mapper is a physically-based spectral classification that uses an n-Dimensional angle to match pixels to reference spectra where n is the number of bands in the image. The algorithm determines the spectral similarity between an image spectrum (representing an unknown material) and a reference spectrum (representing a known material) by calculating the angle between the spectra, treating them as vectors in n-dimensional spectral space, where n is the number of bands. This technique, when used on calibrated reflectance data, is relatively insensitive to illumination and albedo effects. SAM compares the angle between the endmember spectrum vector and each pixel vector in n-D space. Smaller angles represent closer matches to the reference spectrum (L3 Harriz Geospatial (n.d.)).

## 5. RESULTS

Image analysis using the image derived reference spectra based on the selection of pixels of known location of rock types yields relative the best results. Geological interpretation will provide for knowledge on hydrothermal processed and properties.

### 5.1. Endmembers selection

The process of spectral class selection to apply Spectral Angle Mapper resulted in thirteen classes: alunite+jarosite, opal, alunite, dickite, pyrophyllite+alunite, kaolinite, montmorillonite, nontronite, kaolinite+smectite, buildings, water, cultivated fields and roads (Figure 5.1).

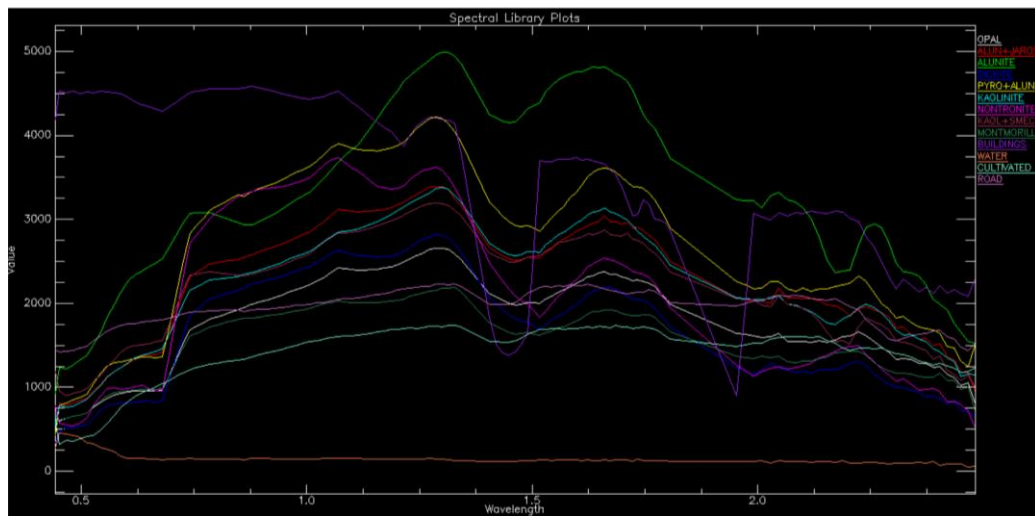


Figure 5.1. Spectral class selection collected from HyMap images.

Based in the results from the laboratory spectroscopy, the first nine endmembers were considered suitable for the description of the alteration system and the identification of the different alteration zones (Table 5.1)

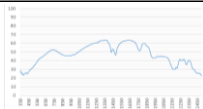
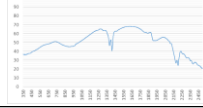
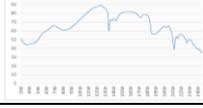
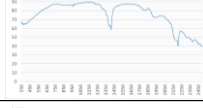
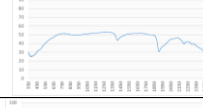
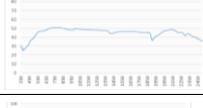
Alteration zone	Endmembers	GPS location		Comments
		X	Y	
Silicic	Alunite+Jarosite	36°51'38.42"N	2° 3'34.87"W	
	Opal	36°51'32.69"N	2° 3'29.20"W	
Supergene	Alunite	36°51'42.69"N	2° 1'27.88"W	±Hidrated halloysite+Crystalline Kaolinite
Intermediate/Advanced Argillic	Dickite	36°51'3.07"N	2° 3'42.69"W	Spectral and geological features proved to be harder to separate. Dickite and pyrophyllite content increase towards the advanced alteration zone
	Pyrophyllite	36°51'38.88"N	2° 3'43.91"W	
	Kaolinite	36°51'41.72"N	2° 1'24.62"W	
Propylitic	Montmorillonite	36°52'23.87"N	2° 3'4.90"W	
	Nontronite	36°52'10.74"N	2° 3'22.03"W	
	Kaolinite+Smectite	36°51'8.11"N	2° 3'43.80"W	

Table 5.1. PRISMA and HyMap endmembers information.

Endmembers were selected from PRISMA and HyMap images, since selection from USGS spectral library was not practical due to the difference in between the spectral signatures with PRISMA. These are pixels where rock-samples collected from the field with the purest spectral signature (compared with USGS library spectra available in ENVI) are located. This

selection was done after interpreting and classifying the rock samples available in appendix 3 and 4, and their spectra in the laboratory (Table 5.1). Once this data was collected, ground points with GPS location with the spectral parameters were extrapolated to HyMap and PRISMA scenes in order to obtain the overview of the spatial distribution of the mineralogy and the alteration zones.

Those being the most representative from the minerals considered significant to separate different alteration zones were the following:

MINERAL	ROCK SAMPLE NAME	ROCK SAMPLE	SPECTRA	LOCATION IN THE MAP
Alunite + Jarosite	05ch094			36°51'38.42"N, 2° 3'34.87"W
Opal	05ch093			36°51'32.69"N, 2° 3'29.20"W
Alunite	MRE02055pm2			36°51'42.69"N, 2° 1'27.88"W
Dickite	MRE01011			36°51'3.07"N, 2° 3'42.69"W
Pyrophyllite + Alunite	MRE02053pm2			36°51'38.88"N, 2° 3'43.91"W
Kaolinite	04MRE125			36°51'41.72"N, 2° 1'24.62"W
Montmorillonite	MRE02019pm1			36°52'17.03"N, 2° 3'9.79"W
Nontronite	MRE02021			36°52'10.74"N, 2° 3'22.03"W
Kaolinite + Smectite	MRE02034			36°51'8.11"N, 2° 3'43.80"W

*Table 5.2. List of endmembers selected from the ITC rock-samples together with their spectral signature and location in the map.*

The locations of the rock-samples selected were designed with the intention of covering all the alteration zones of the area following the two cross-sections traced along Los Tollos and Cerro del Cinto (Figure 5.2).



Figure 5.2. Location of the rock samples selected to create the spectral library for HyMap and PRISMA images.

For this selection a comparison between the different sources was needed. The main source was the spectra collected in the laboratory. The following step was comparing it with the corresponding PRISMA and HyMAP image pixel spectra and with USGS spectral library available in Envi.

This procedure ensured the right selection of endmembers for the later SAM calculations. An example is provided of Alunite spectra (Figure 5.3).

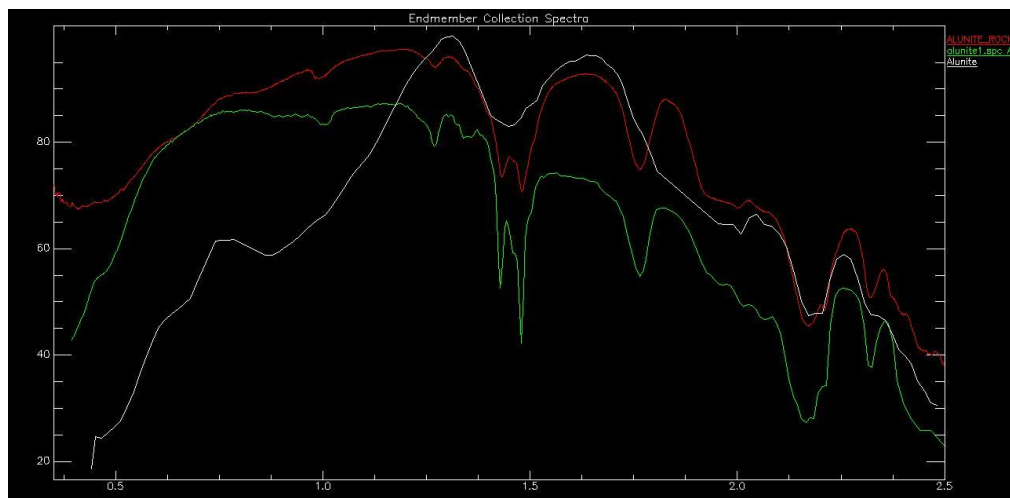


Figure 5.3. Comparison of alunite spectra coming from different sources. White from HyMap images (Cabo de Gata 2 & 3), red from rock sample analysed in the laboratory and green from USGS spectral library.

After collecting these endmembers, the same locations were used to pick the data from PRISMA images. This order of selection of endmembers is necessary due to the poor quality of PRISMA spectra (Figure 5.4). When extracting the endmembers from PRISMA images, one can predict this problem already, since all spectra have dead-points around 1400 and 1900 nm, points which are critical for interpretation. These absorptions are related to atmosphere water absorption bands.

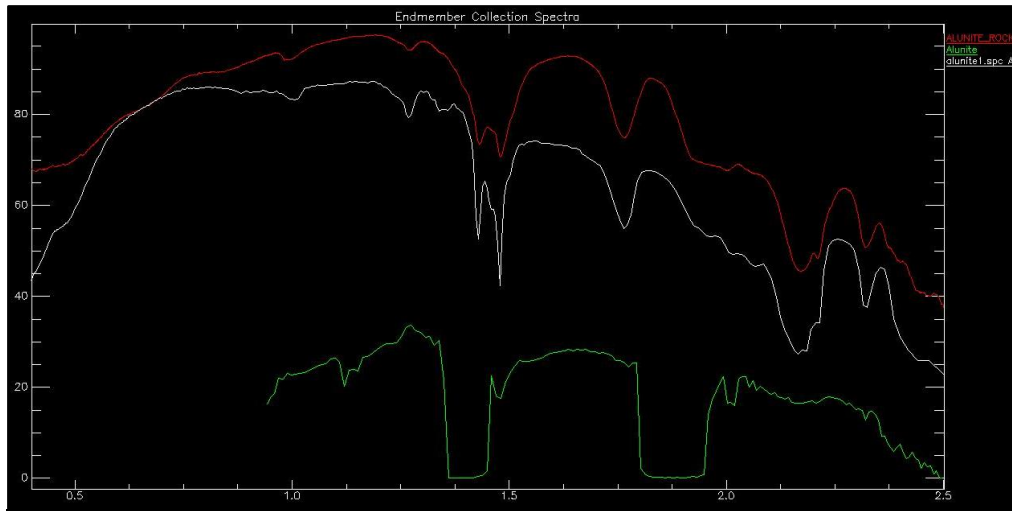


Figure 5.4. Comparison of alunite spectra coming from different sources. White from USGS spectral library, red from rock sample studied in the laboratory and green from PRISMA images.

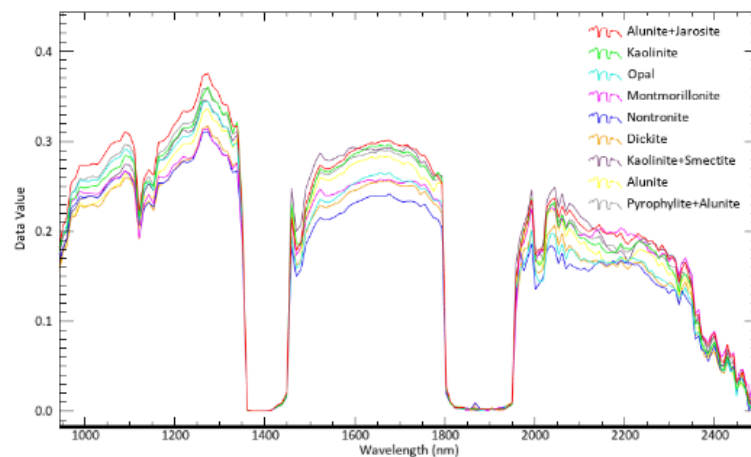


Figure 5.5. Spectra collected of minerals selected for SAM calculation obtained from PRISMA images.

Spectral signatures coming from PRISMA images cannot be compared with USGS spectral library or with the spectral library created in the laboratory (which provide information about the composition of the rock-samples) due to the incompatibility of laboratory and image spectra. Despite this, image spectra collected in PRISMA and HyMap can be used for mapping.

## 5.2. NDVI Results

Masking vegetation is performed by the use of the so-called NDVI. The NDVI picture (Figure 5.1) is computed as the difference between Near-Infrared (NIR between 0,7-1,1 $\mu$ m) and Red (between 0,6-0,7 $\mu$ m) reflectance divided by their sum (J Liu (2005)).

For PRISMA images the bands assigned to NIR and Red are 44 and 32, respectively. For HyMap images these bands are 26 and 17, respectively.

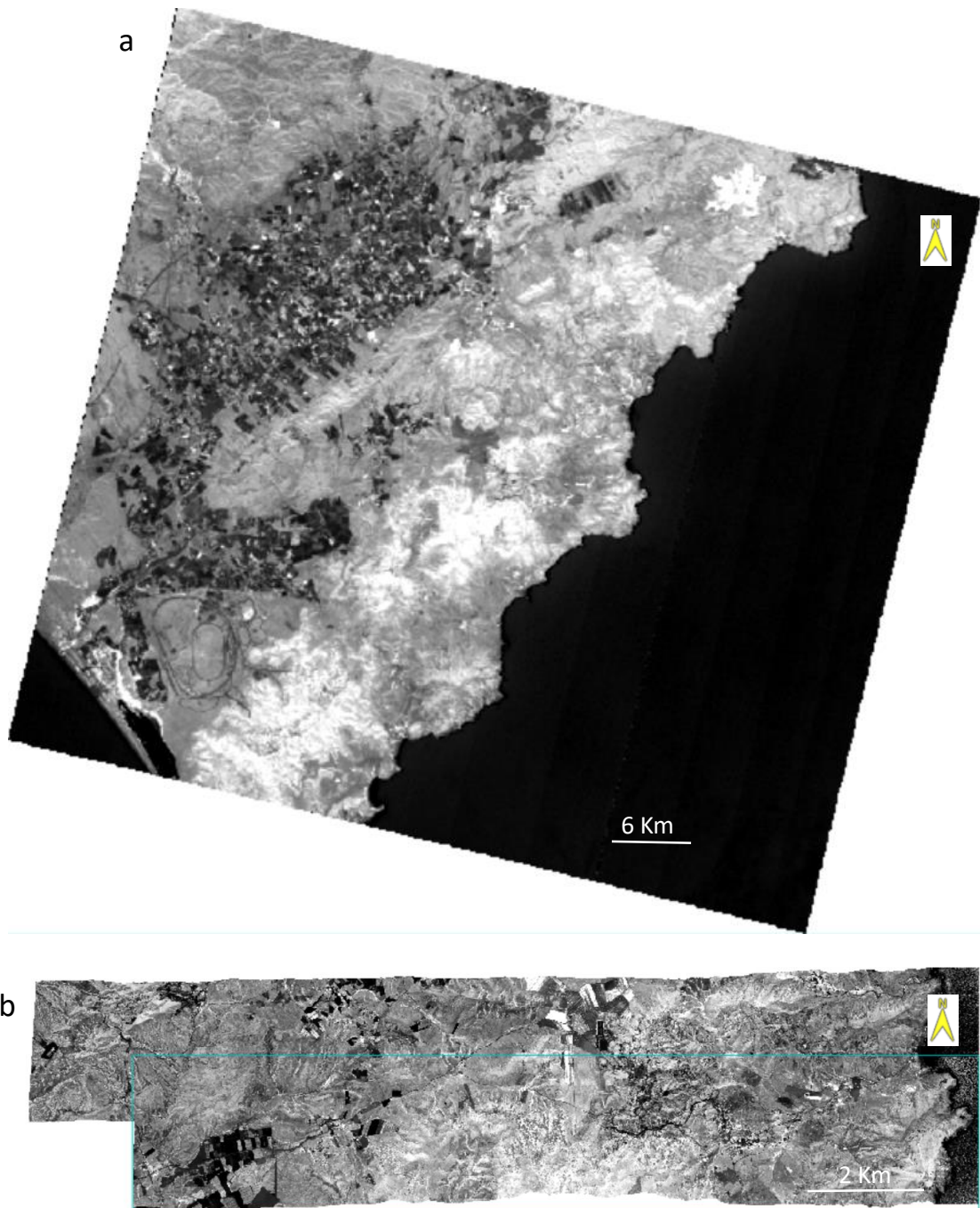


Figure 5.6. NDVI images calculated from PRISMA images (a) and HyMap images (b).

The filter applied in this report to mask vegetation filters all pixels with a NDVI value higher than 0.18 (based on statistics). A total of 33,78% of the pixels were masked in PRISMA image. HyMap images Cabo de Gata 2 & Cabo de Gata 3 had a total of 2,69% and 2,38% of pixels masked.

### 5.3. SAM map resulted from HyMap images using image endmembers

The results after applying Spectral Angle Mapper method were produced in the wavelength range of 0.5 and 2.5  $\mu\text{m}$ . The spatial distribution of these minerals show

patterns of the alteration zones, being the most peripheral the propylitic alteration zone, and the silicic/advanced argillic located more in the centre of the area, taking place in areas where important faults are also present (Figures 5.7 & 5.8).

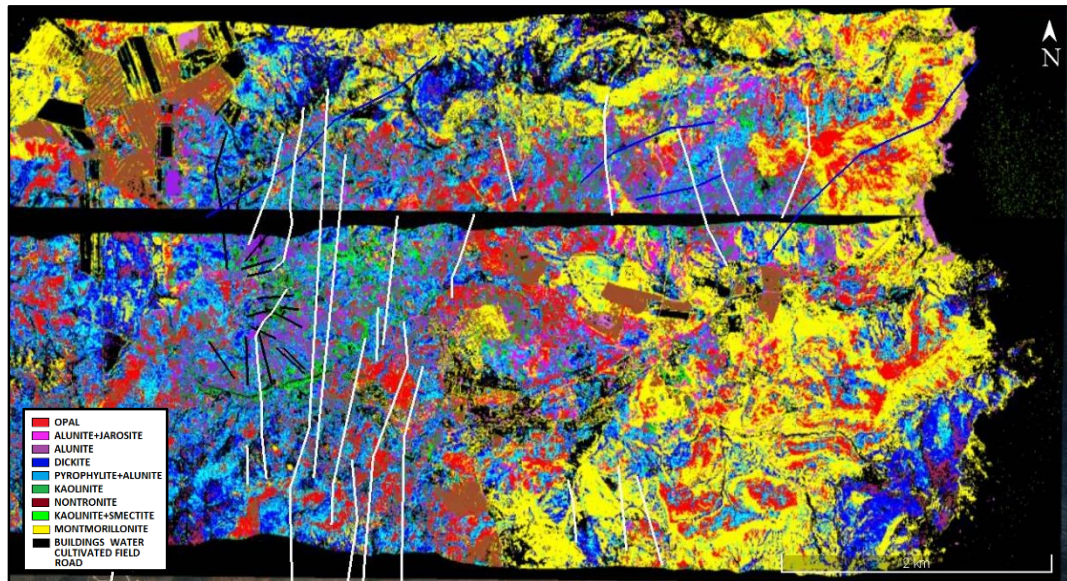


Figure 5.7. HyMap SAM Cabo de Gata 3 on top of Cabo de Gata 2. White, blue and black lines representing important faults in the area and thick black lines representing the location of the cross-sections which will indicate the changes in the alteration zones.

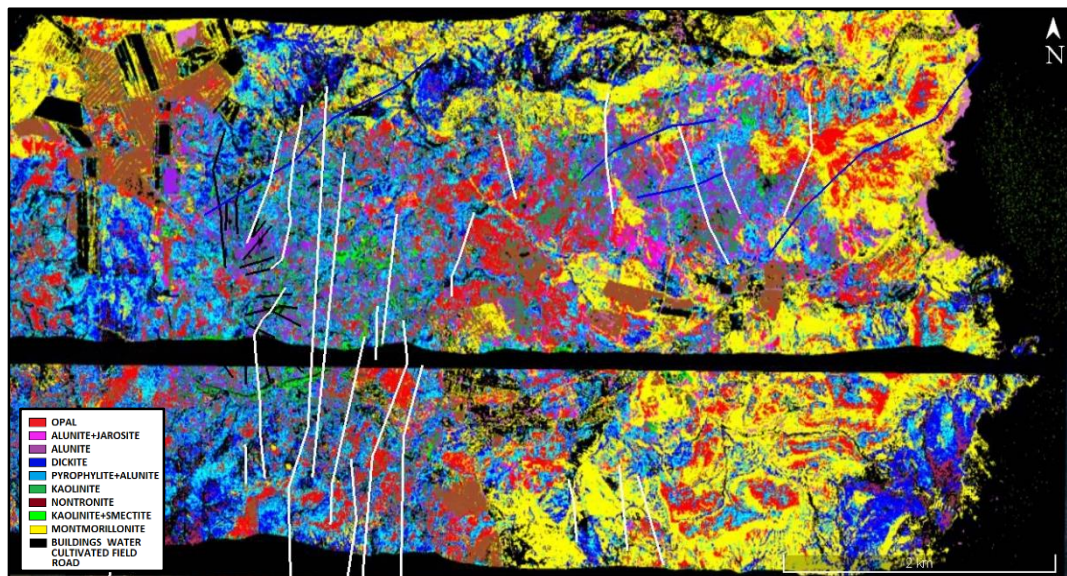


Figure 5.8. HyMap SAM Cabo de Gata 2 on top of Cabo de Gata 3. White, blue and black lines representing important faults in the area and thick black lines representing the location of the cross-sections which will indicate the changes in the alteration zones.

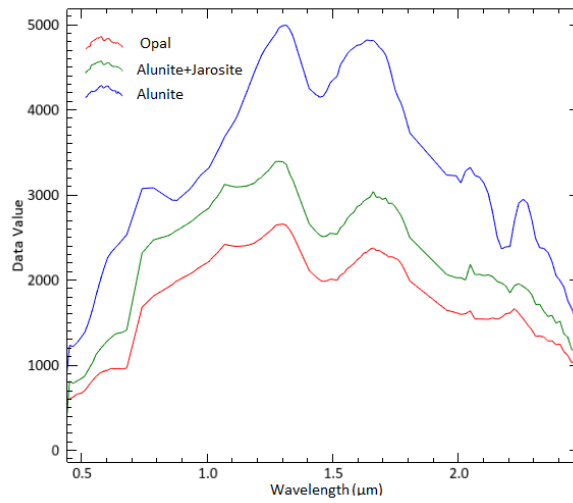


Figure 5.9. Spectral signature assigned for silicic and supergene alteration zones (Source HyMap image).

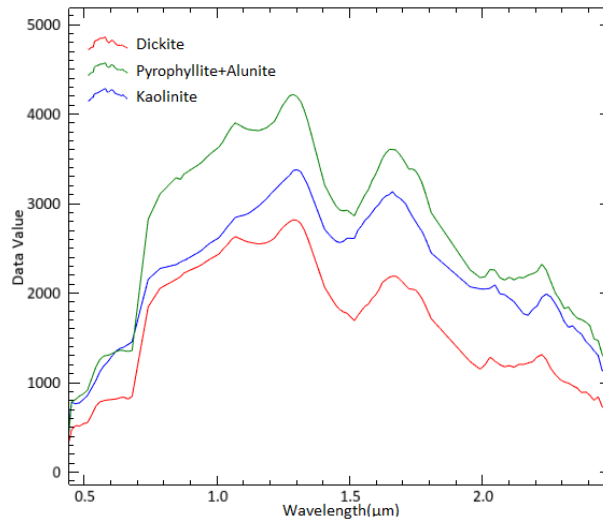


Figure 5.10. Spectral signature assigned for advanced and intermediate argillic alteration zones (Source HyMap image).

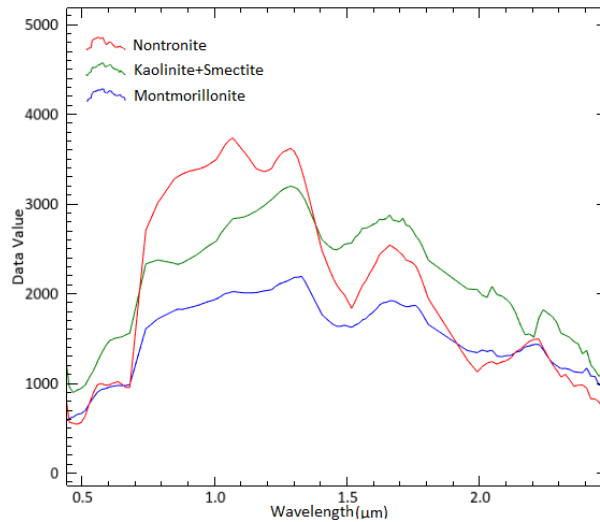


Figure 5.11. Spectral signature assigned for propylitic alteration zone (Source HyMap image).

#### 5.4. SAM map resulted from PRISMA images using image endmembers

PRISMA image results show a more general pattern compared to the more specific pattern acquired from HyMap images. However, this outcome was predictable due to the lower resolution of PRISMA. Interpretation of the absorption features related to rock type and content is difficult and complex.

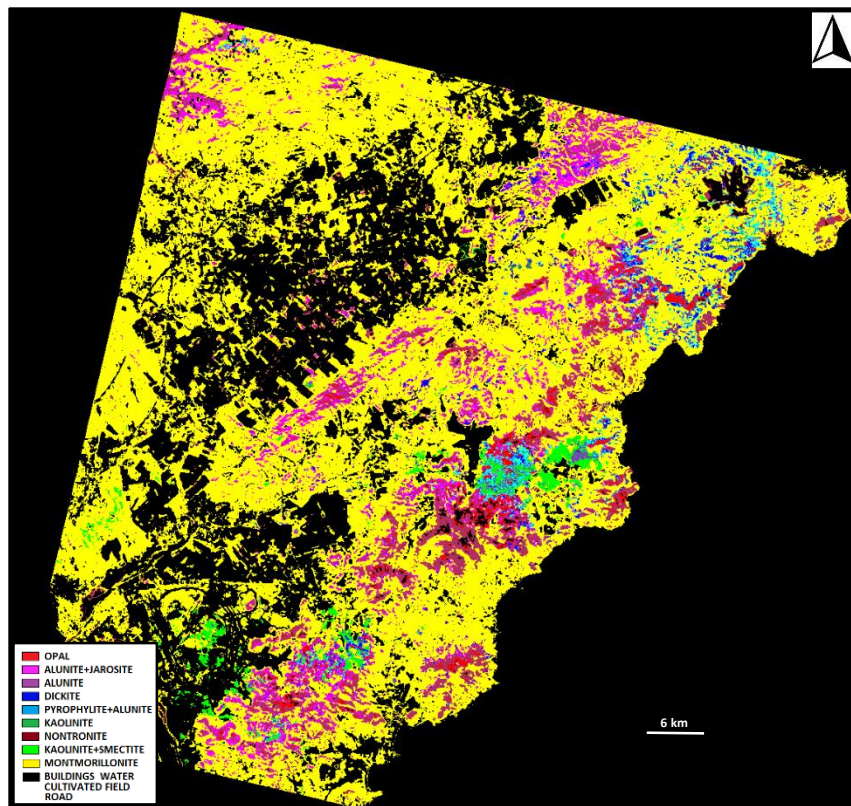


Figure 5.12. Image map resulted from PRISMA SAM classification. In this image it is noticeable the low resolution of PRISMA compared to HyMap images.

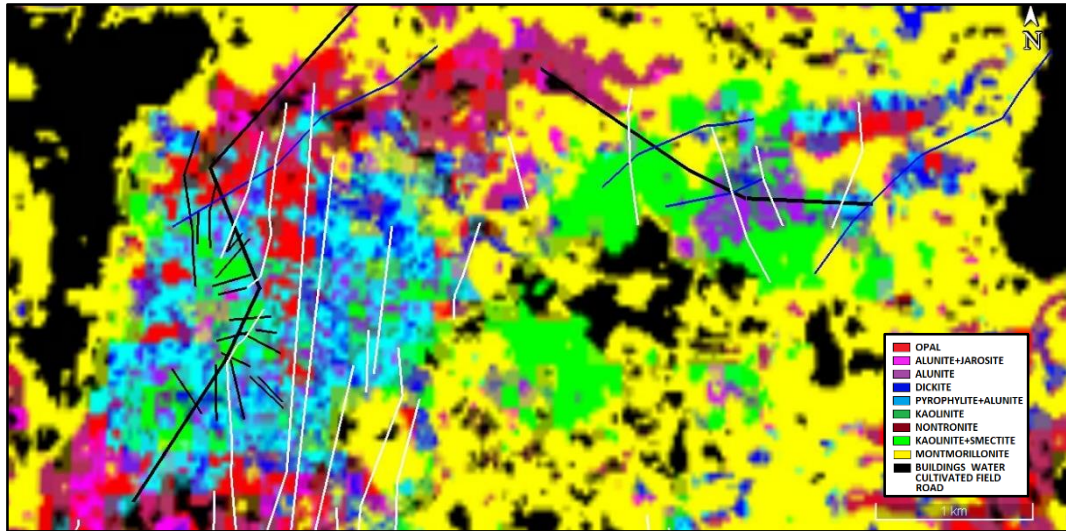


Figure 5.13. PRISMA image resulted from SAM classification. White, blue and black lines representing important faults in the area and thick black lines representing the location of the cross-sections which will indicate the changes in the alteration zones.

Similar to HyMap SAM images, PRISMA SAM results recognized a bigger area dominated by alunite at Los Tollos, which is noted for the presence of a supergene alunite blanket. However, this results exposes this alteration zone in a more general distribution. To the Western part of the image, in Cerro del Cinto deposit, minerals as opal and alunite+jarosite become more abundant, coinciding with radial faults surrounding the caldera margin.

The following images are the spectral signatures from the endmembers selected from PRISMA images for the SWIR range:

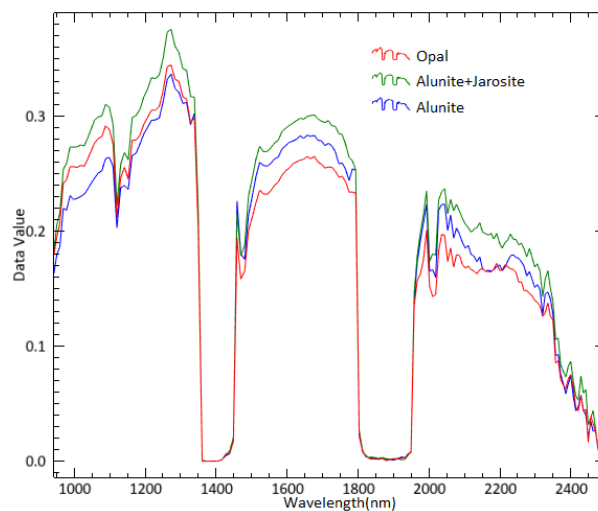


Figure 5.14. Spectral signature assigned for silicic and supergene alteration zones.

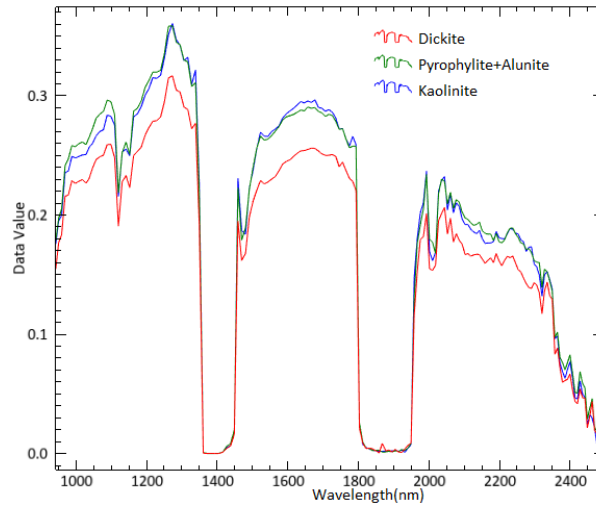


Figure 5.15. Spectral signature assigned for advanced and intermediate argillic alteration zones.

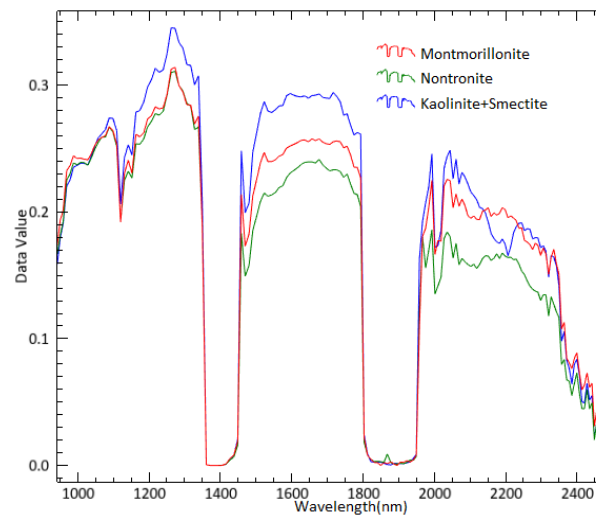


Figure 5.16. Spectral signature assigned for propylitic alteration zone.

### 5.5. Comparison with other sources of information

The hydrothermal alteration and geology within the area of Rodalquilar deposit has been well summarized and carefully mapped by many authors as Rytuba et al., 1990; Arribas et al., 1995, and Bedini et al., 2009, which makes this area an excellent zone to develop and test remote sensing and spectroscopic methods for mineral exploration (Van de Meer et al., 2018) (figure 5.17).

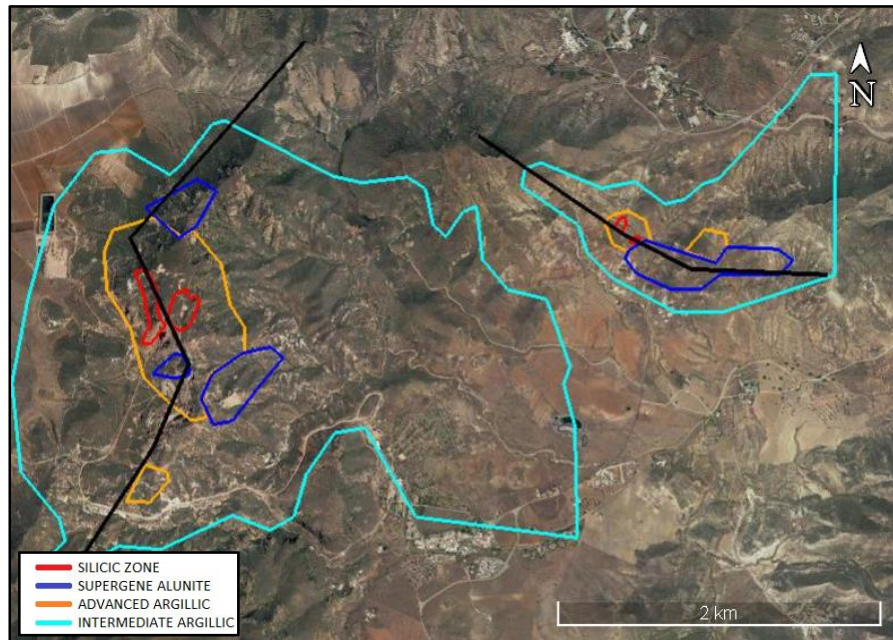


Figure 5.17. Alteration map of the Rodalquilar area (modified after Arribas et al., 1995) which show alteration patterns.

After taking the map from Arribas et al. 1995, as the base building block and delineating the boundaries in between the different alteration zones, it is visible the levels of accuracy of the resulting maps after applying SAM calculation. Differences and similarities of PRISMA and HyMap images versus figure 5.17 were investigated.

For example, the inner parts of the high sulphidation epithermal system indicated by Arribas et al. were matching in many parts of the HyMap images (Figure 5.18), especially purple areas which indicate high amount of alunite. Outer zones are also well indicated, coinciding limits set by Arribas with the ones obtained from HyMap (yellow parts).

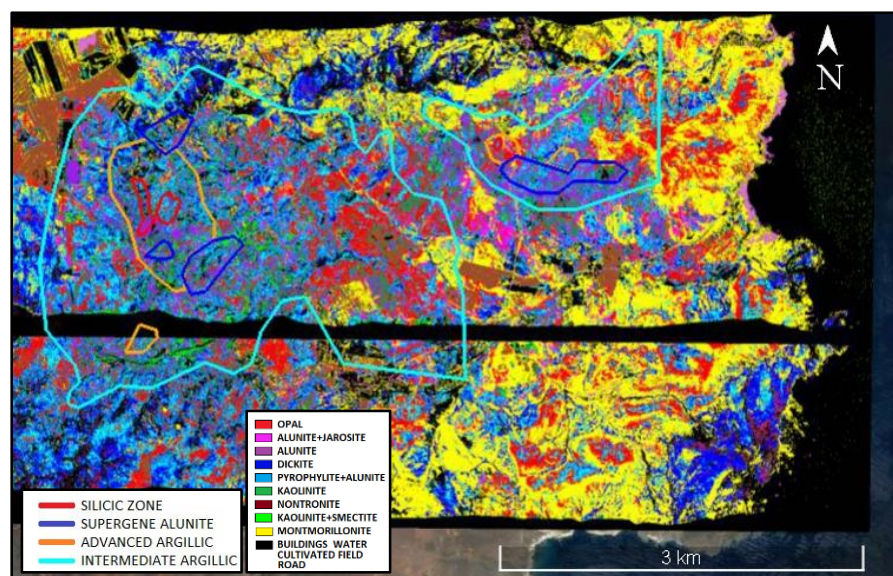


Figure 5.18. Alteration map of the Rodalquilar area (modified after Arribas et al., 1995) showing alteration patterns on top of HyMap images.

Comparing PRISMA images (Figure 5.19) with the alteration zones from Arribas et al. 1995, some of these epithermal trends can be identified from the minerals mapped. Those minerals classified as highly altered are to some extent within the silicic and supergene alteration zones mapped by Arribas et al., while more external minerals as dickite or kaolinite are within the intermediate argillic zone. Cerro del Cinto epithermal alteration setting seems to adapt better to Arribas et al. map than Los Tollos deposit alteration. Montmorillonite and kaolinite are mapped in many parts of Los Tollos within supergene and silicic alteration zones.

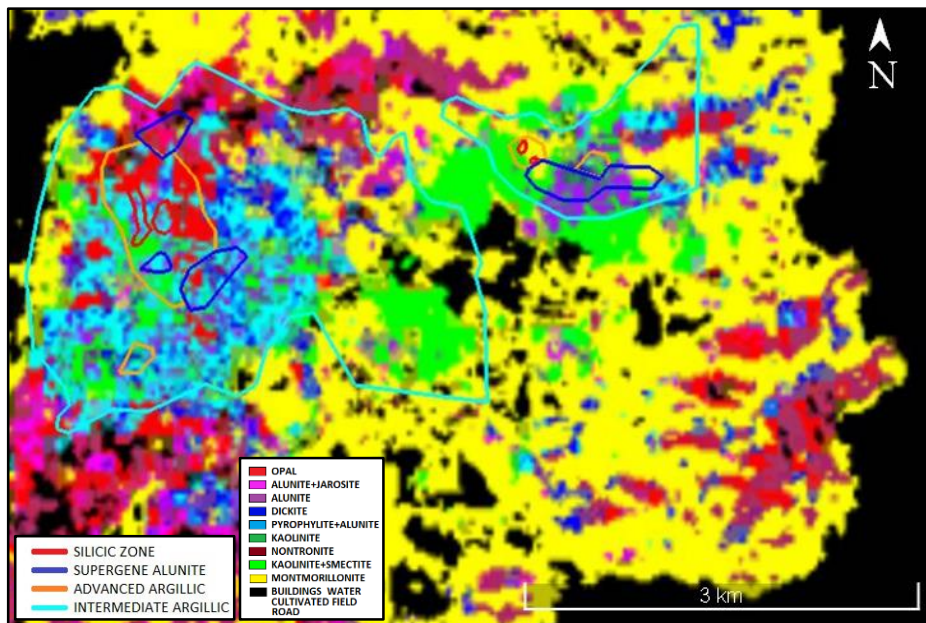


Figure 5.19. Alteration map of the Rodalquilar area (modified after Arribas et al., 1995) showing alteration patterns on top of PRISMA image.

A more detailed comparison is realised in chapter 5.7.4, taking into account information from the maps obtained from PRISMA and HyMap images, and from the rock-samples collected from the field.

#### 5.6. Cross-sections indicating alteration zones and rock samples

HyMap images and PRISMA images have fairly good image quality in terms of signal-to-noise ratios (SNR) and provide information at different spatial scales (5m versus 30m pixels). Therefore, they provide different spatial patterns of the hydrothermal area.

Cross-sections over the hydrothermal alteration zones as indicated in Figure 3.5 provided detailed information about the transition and boundaries of the mineral occurrence. In order to get cross-sections to later compare the different results obtained by using HyMap, PRISMA and rock-sample information, these cross-sections were divided into four (in the case of Cerro del Cinto deposit) and three (in the case of Los Tollos deposit) sub-sections. Cross-section P.C was traced crossing Cerro del Cinto deposit from North to

South. Cross-section P.T was traced crossing Los Tollos deposit from North-West to South-East (Figure 5.20).

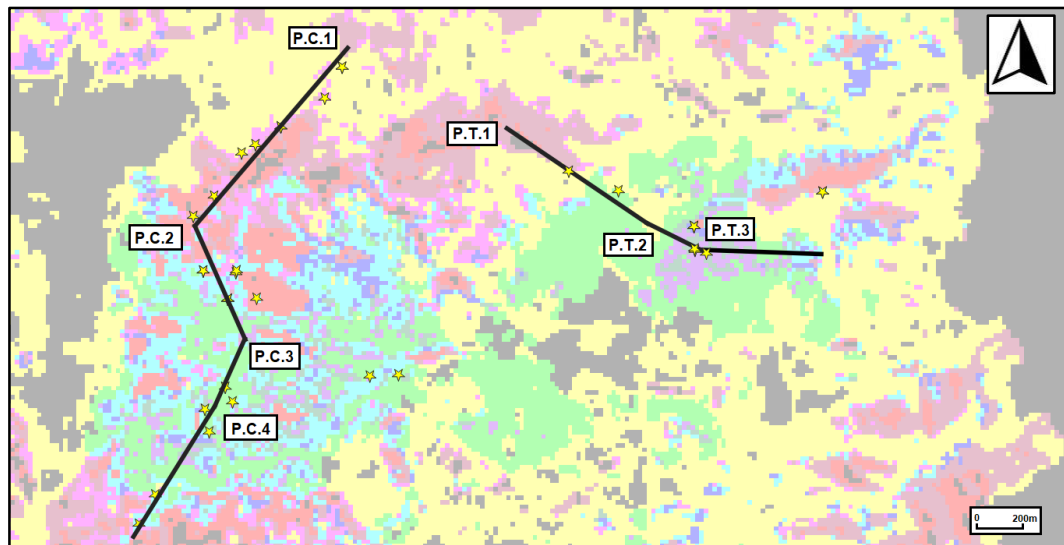


*Figure 5.20. Final setting of cross-sections (on top of PRISMA image) used to represent alteration zones distribution. Yellow stars symbolize rock-samples collected in the field and studied in the laboratory.*

#### 5.6.1. Cross-section from HyMap images

The following pictures are some of the cross-sections obtained from calculating SAM using HyMap images. These cross-sections show in 2D the spreading of the epithermal system patterns. For a complete overview of all the cross-sections obtained go to Appendix 5.

Pink, red and purple colours correspond to alunite+jarosite, opal and alunite minerals respectively. Together they represent silicic and supergene zones.

Dark blue, light blue and dark green colours correspond to dickite, pyrophyllite+alunite and kaolinite respectively, representing the intermediate argillic and argillic zones.

Yellow, brown and green colours correspond to montmorillonite, nontronite and kaolinite+smectite respectively, representing the propylitic zone.

These zones are hard to differentiate based exclusively on spectral signatures. Thus, information from rock-samples would be needed for a final interpretation.

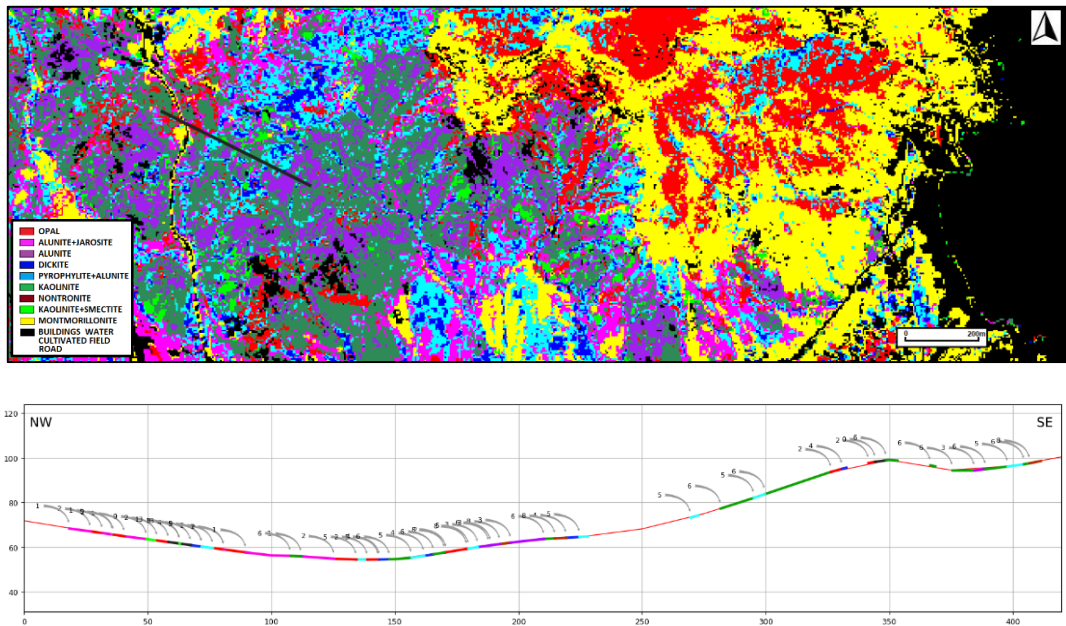


Figure 5.21. A. Location of the cross-section selected. B. Cross-section P.T.2 from Los Tollos deposit.

P.T.2 is located in Los Tollos deposits (Figure 5.21). This cross-section goes through a high alteration zone from North-West to South-East, having some less-altered zones from the middle of the section to the end. From 0 to 130 m minerals as alunite+jarosite, alunite and opal are abundant, which can be interpreted as a silicic alteration zone. From 130 m to almost the end of the cross-section (around 350 m) blue and green colours (corresponding to dickite, pyrophyllite+alunite and kaolinite+smectite) become more dominant, indicating a more external zone of the epithermal alteration zone. In spite of this, this part of the section has some alunite points appearing in between these more external alteration zones. These points of alunite in between external alteration zones coincide with important faults from Arribas et al., 1995 map, which would explain their abruptly appearance (Figure 5.22). The final part of the cross-section is again dominated by more alunite (purple colour).

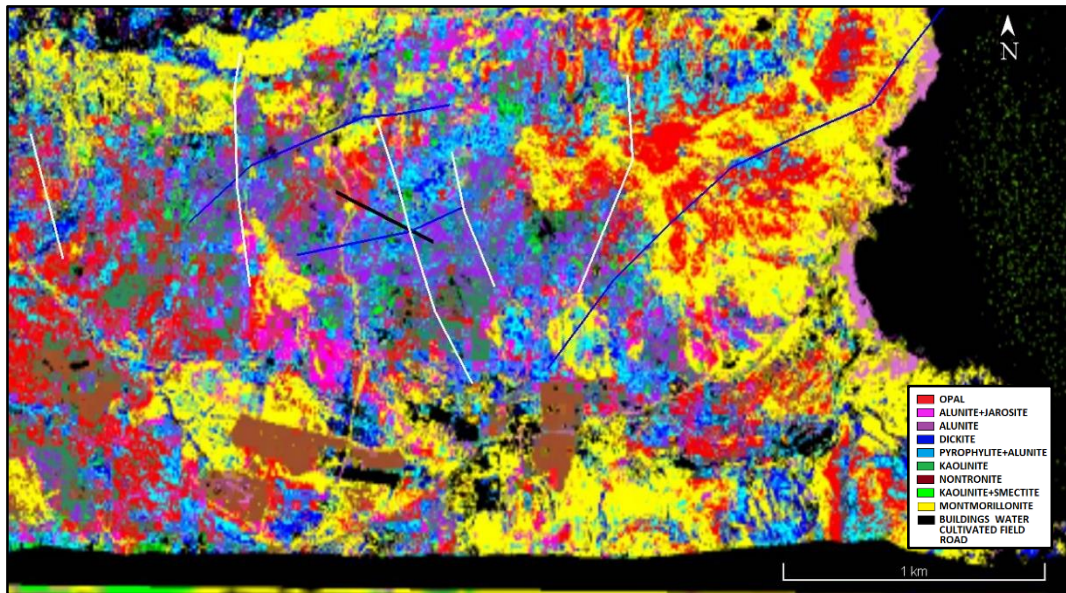


Figure 5.22. HyMap image of Los Tolloos with P.T.2 cross section (black) and important faults (white, blue and black) influencing the deposit.

P.C.2 cross-section is located in Cerro del Cinto deposit (Figure 5.23), in the limits of the caldera margin. It shows a more intermediate zone towards the North-west of the profile, which evolves to a more silicic zone towards the South-eastern part, where alunite is highly abundant, especially from 500m to 760m.

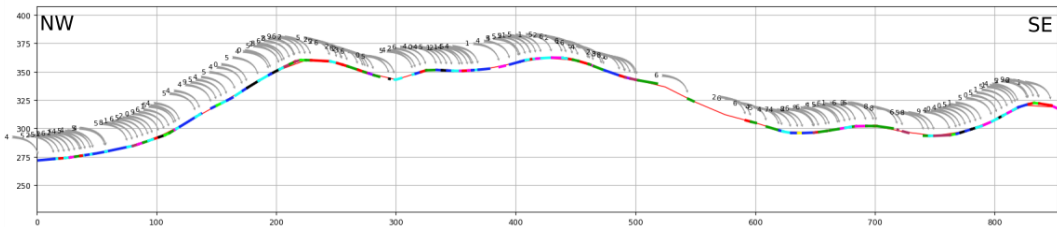
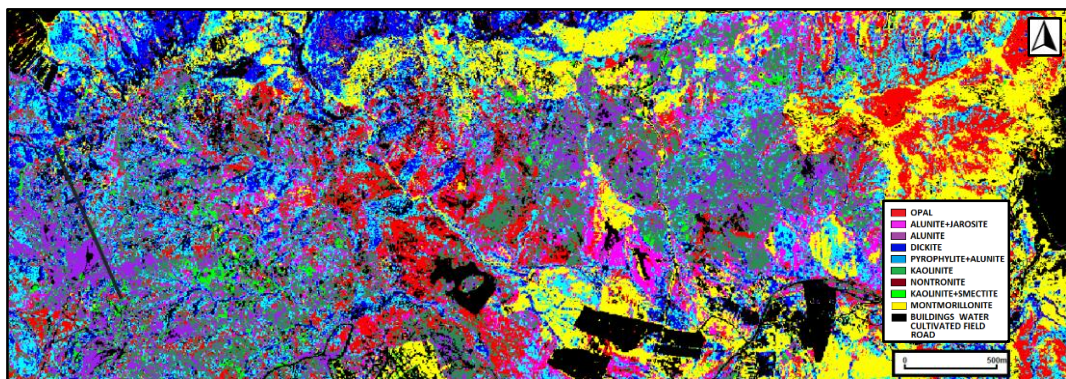


Figure 5.23. A. Location of the cross-section selected. B. Cross-section P.C.2 from Cerro del Cinto deposit.

These zones where alunite is more abundant, coincide with radial faults surrounding the caldera, faults that were formed due to the continued resurgence of the caldera and which may contain the most economically important deposits in the caldera complex.

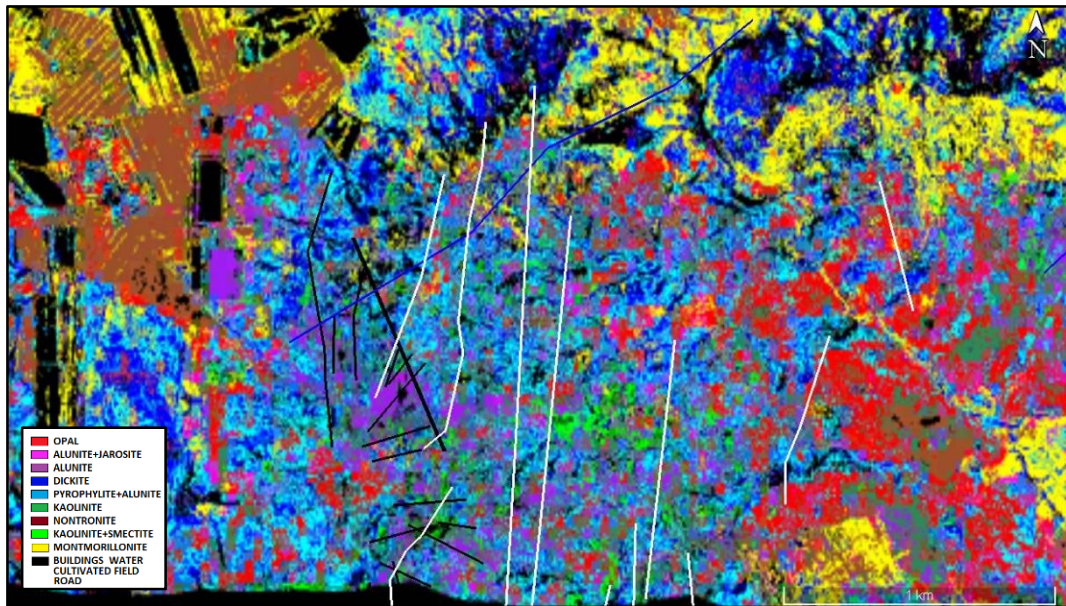


Figure 5.24. HyMap image of Cerro del Cinto with P.C.2 cross section (black) and important faults (white, blue and black) influencing the deposit.

Cross-sections obtained from HyMap images are more difficult to read. The resolution of this images is higher (5x5m), which leads to a more detailed map with a larger amount of horizontal changes in between alteration zones.

#### 5.6.2. Cross-section from PRISMA images

Cross-sections obtained from PRISMA images show a more general distribution of the halo produced by the epithermal system in both deposits, leading to more smooth changes in between alteration zones and visually more clear in cross-sections. The legend used to represent minerals is the same applied to HyMap images, therefore comparison in between cross-sections can be directly done. The following cross-section is the same as the one used in 5.6.1.

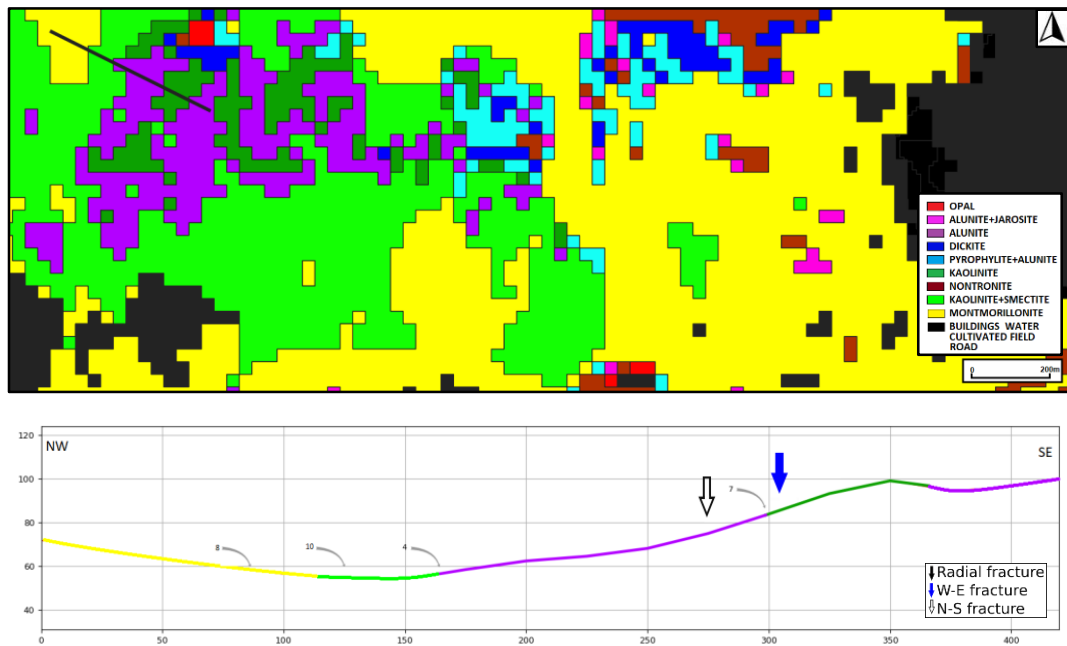


Figure 5.25. A. Location of the cross-section selected. B. Cross-section P.T.2 from Los Tollos deposit with blue and white arrows indicating important faults (W-E and N-S, respectively).

The first part of this section, located in Los Tollos deposit (Figure 5.25), starts with external minerals from the alteration zone, evolving to a more altered in the mid-section. This middle part is a good example to highlight how PRISMA classification is more general than HyMap. While HyMap cross-section show alternation of alunite and more external zone minerals, PRISMA classifies this entire zone as alunite.

Faults in this part of Rodalquilar deposit do not coincide that well with PRISMA images (Figure 5.26), since alteration zones seem to not be following their trends or they are not affected by them.

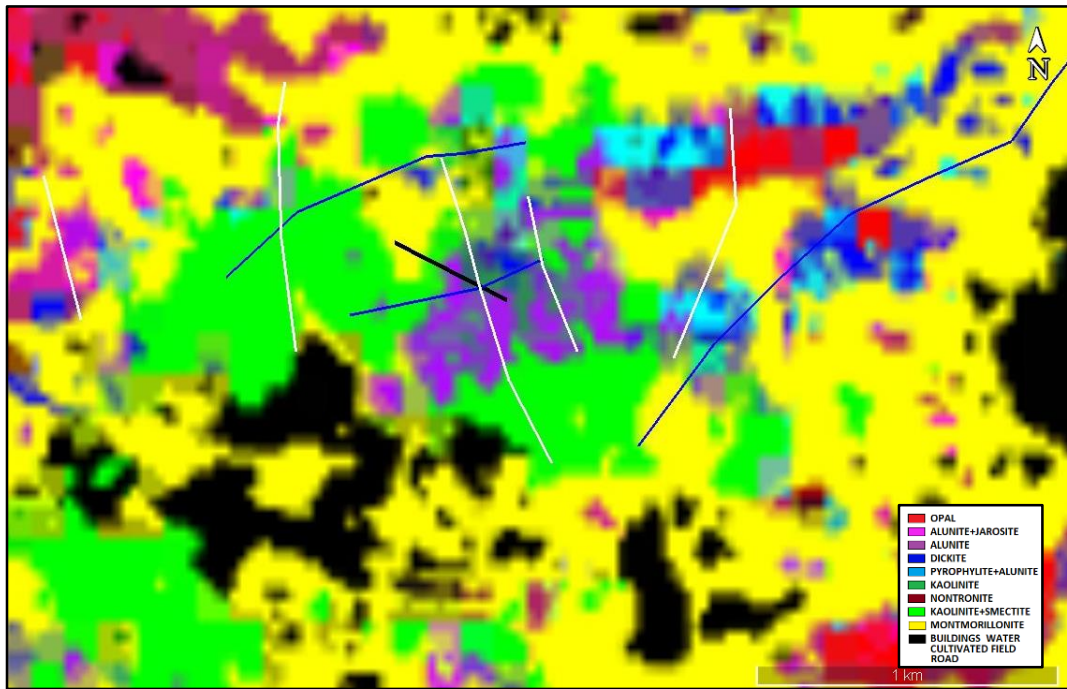


Figure 5.26. SAM classification of PRISMA images. White, blue and black lines represent important faults within the deposit of Los Tollos.

SAM classification from PRISMA image in Cerro del Cinto (Figure 5.27) shows a less altered zone than HyMap in the South-eastern part of the cross-section, being kaolinite and pyrophyllite+alunite more abundant in this part. The North-western part of the cross-section shows a more altered zone, with opal and alunite+jarosite being the main minerals.

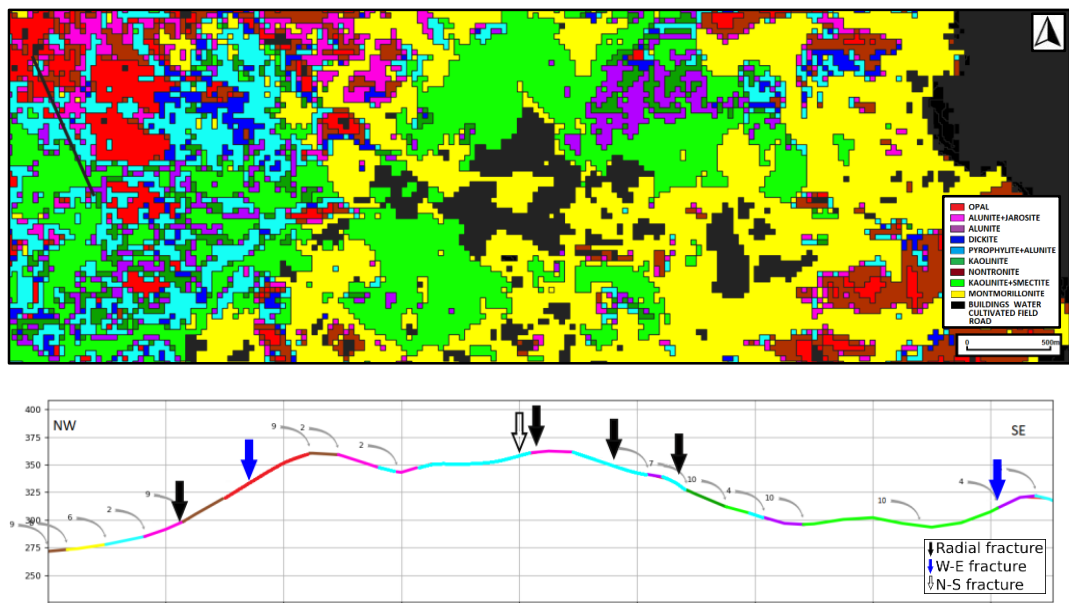


Figure 5.27. A. Location of the cross-section selected. B. Cross-section P.C.2 from Cerro del Cinto deposit with black, blue and white arrows indicating important faults (radial, W-E and N-S, respectively).

Again, zones of vuggy silica (those where alunite+jarosite and opal are more dominant) seem to be controlled by faults located mainly within the eastern margin of the Lomilla caldera (Arribas et al., 1995) (Figure 5.28). Many of the faults within this cross-section (Figure 5.27) coincide with highly altered zones. Those faults falling out of them, fall in advanced/intermediate argillic alteration zones.

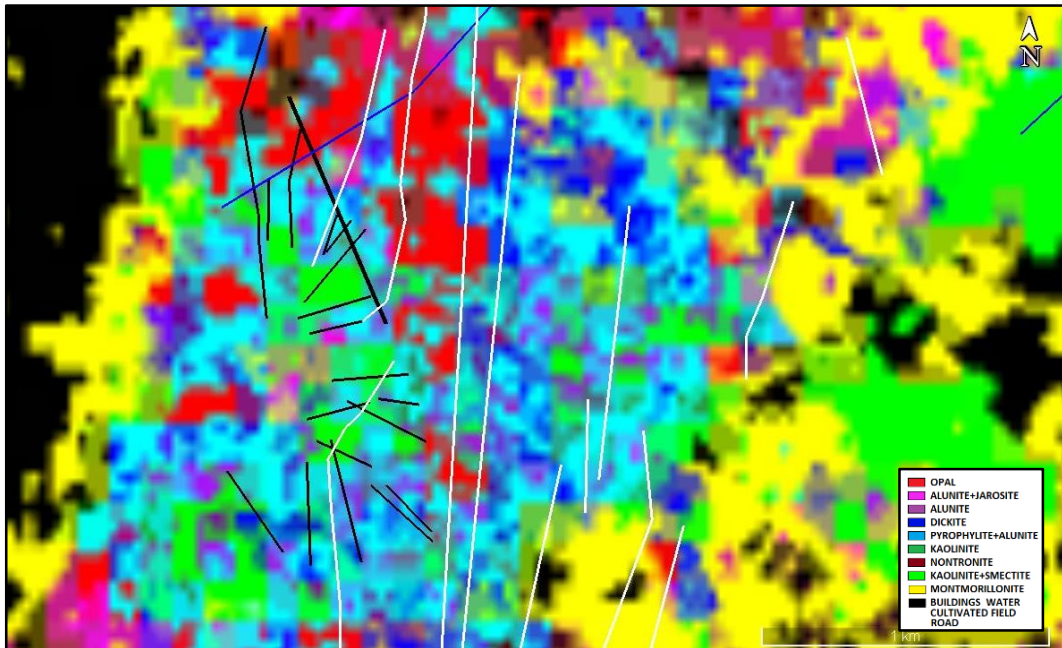


Figure 5.28. SAM classification of PRISMA images. White, blue and black lines represent important faults within the deposit of Cerro del Cinto.

### 5.7.3. Cross-section from rock-samples projection

The obtained cross-sections, based on the projection of rock-samples in this cross-sections, are a rough interpretation of the evolution of the alteration zones. In many of these cross-sections the information is poor (as for example in P.T.3 where there is only one rock-sample available). Hence, geological interpretation needs to be done in between alteration zones, since the transit between silicic and prophylic alteration zones require intermediate stages of pressure and temperature and, therefore, less altered minerals belonging to advanced or intermediate alteration zones.

For interpretation it should be also taken into account the distance of these rock samples to the cross-sections, since the buffer applied was  $\pm 200$  m.

The rock-samples information to create these cross-sections is found in appendix 3 and 4.

Hence, colours in these cross-sections do not represent minerals, as in HyMap and PRISMA cross-sections, but alteration zones. Silicic alteration zone is represented by red, indicating areas where extremely acid environment led to the formation of minerals as opal and alunite+jarosite. Supergene zone is represented by blue, indicating zones that were developed due to the atmospheric oxidation of sulphides during weathering (Arribas et al., 1995). Brown represents advanced alteration zones, indicating rocks that occur specially in the Cinto area surrounding the cores of vuggy silica and enclosing most of the Au orebodies (Arribas et al., 1995). Light blue intermediate alteration zones, indicating

zones that were developed at higher temperatures (<180°C) than the advanced argillic zone (<120°C). Green the outermost propylitic alteration zone, developed at >240°C deep in the epithermal environment.

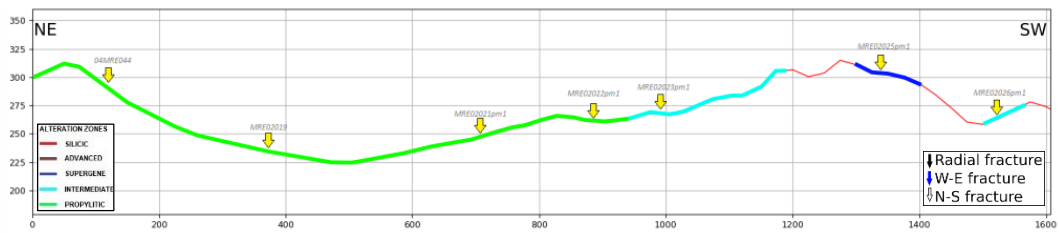


Figure 5.29. Cross-section P.C.1.

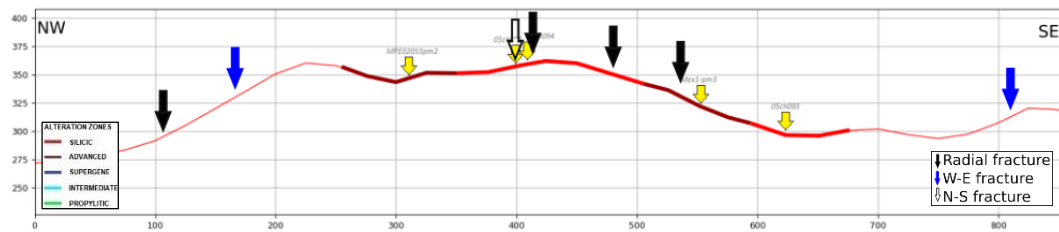


Figure 5.30. Cross-section P.C.2.

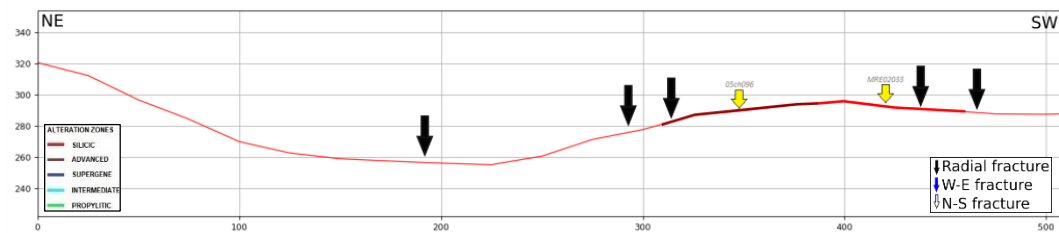


Figure 5.31. Cross-section P.C.3.

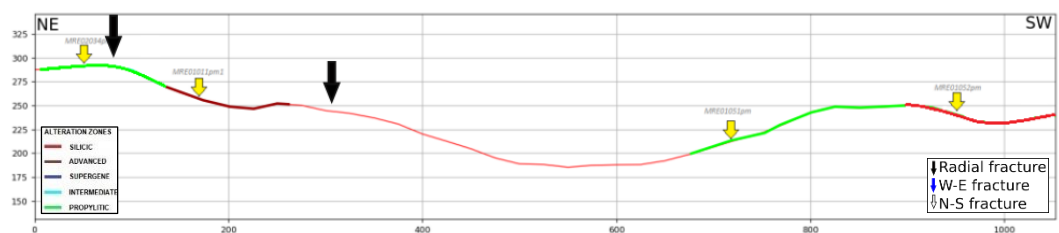


Figure 5.32. Cross-section P.C.4.

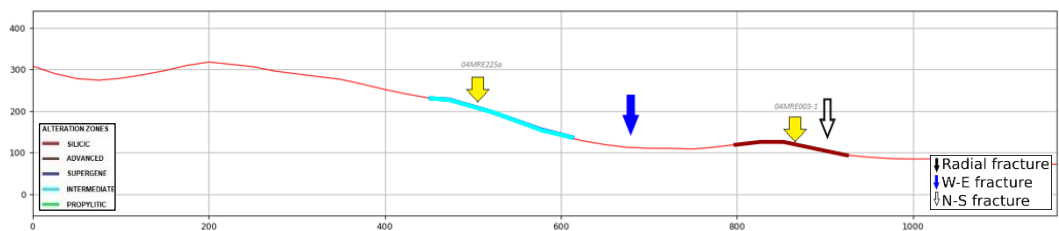


Figure 5.33. Cross-section P.T.1.

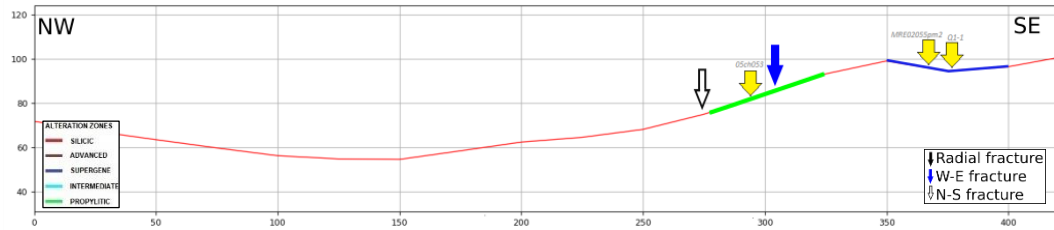


Figure 5.34. Cross-section P.T.2.

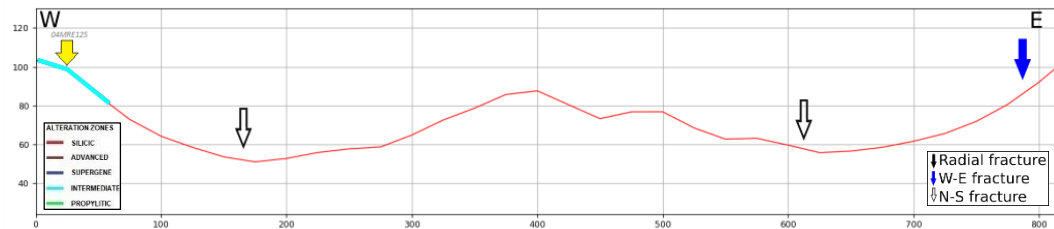


Figure 5.35. Cross-section P.T.3.

#### 5.7.4. Comparison between PRISMA-HyMap-Rock samples cross-sections

To evaluate the results and assess their quality, cross-sections resulted from the two different sources (HyMap and PRISMA images) were compared. Rock-samples cross-sections were also used to confirm interpretations. In cases where rock-samples were more far away from the cross-sections, comparison was done directly from the SAM maps, at the location of these samples and in parts of these sections where there was no rock-sample information.

##### Comparison P.C.1

The first part of this section (NE) is not described since it falls out of the HyMap coverage area. However, PRISMA image and rock-sample (04MRE044) cross-sections coincide with classification of this part as propylitic.

Part of the section where rock-sample MRE02019 falls, is classified as propylitic (specifically as montmorillonite). Although this rock-sample is too far from the cross-section to take it as reference within the cross-section (123 meters), HyMap maps coincide with its classification. PRISMA classifies the pixel where the rock-sample falls as silicic alteration zone, however, the cross-section itself coincides with the other ones.

After this rock-sample, comes the transition between propylitic and silicic alteration zones towards the end of the cross-section. This transition is not well represented by none of the sources. PRISMA cross-section abruptly changes from propylitic zones being in direct contact with silicic zones, dismissing intermediate transitions.

The following rock-sample is MRE02021, classified from its spectra and VISU characteristics as andesite/dacite, corresponding to the outermost part of the alteration zones. This sample is wrongly classified by PRISMA as alunite+jarosite. However, HyMap coincides in its classification as nontronite, which coincides with the part of the alteration zone this rock-sample falls in.

MRE02022 rock-sample is rightly classified by both PRISMA and HyMap as montmorillonite (propylitic zone), coinciding with spectral and VISU classification.

The next rock-sample is MRE02023 (which falls 60 meters far away from the cross-section). Based on spectral and VISU classification, this sample is classified as kaolinite. However, PRISMA classifies it wrongly in the propylitic alteration zone. HyMap classifies it as pyrophyllite+alunite, which is not totally wrong since it coincides with the alteration zone (intermediate argillic).

Sample MRE02025 appears to hold the same problem. From spectral and VISU information, it is classified in the supergene alteration zone. It also falls in this zone in HyMap map, however PRISMA classifies it at the intermediate and propylitic argillic alteration zone.

The last rock-sample (MRE02026) located at the end of the cross-section (SW) is wrongly classified by both PRISMA (as silicic zone) and HyMap (as intermediate zone) compared to VISU-Spectral classification (propylitic zone).

### Comparison P.C.2

In general, this cross-section goes through a quite altered zone.

Parts of the sections where there are not rock-samples available are different in between the cross-sections. The South-Eastern part of the cross-section in HyMap quite altered, while PRISMA classifies this zone as a more intermediate alteration area with some spot characterized by high-altered minerals. However, the Western part of the cross-section from HyMap is characterized by a less altered zone than the one from PRISMA, being this last one characterized by the presence of opal and some alunite+jarosite.

Rock-samples are available in the central part of the cross-sections. MRE02053 is classified in the advanced alteration zone based on spectral and VISU information. HyMap and PRISMA pixels also classify this sample in the same alteration zone, although it is important to be aware of that classification of the mineral by these maps differs from VISU-Spectral classification.

05ch095 and 05ch094 rock-samples too remote to project them at the cross-section (140 meters). However, the classification of the pixel in that location coincide in both PRISMA and HyMap images (silicic alteration zone).

The following rock-sample is Mex-pm3. Its classification coincides in HyMap and rock-sample cross-sections as alunite. However, PRISMA classifies this area in the intermediate argillic alteration zone, differing from the others.

The last rock-sample (05ch093) falls in the limit of the buffer applied (180 meters far away from the cross-section). Both PRISMA and HyMap classification coincide. Although their pixels are representing this sample as a different mineral, they are both from the same high altered zone.

### Comparison P.C.3

HyMap cross-section generally represents a highly altered zone of the deposit, being alunite the most abundant mineral of these alteration zone. On the other hand, PRISMA

cross-section keeps on classifying this whole area as a more external propylitic alteration zone.

In the South-West part of the cross-section there is rock-samples information available. With VISU information, 05ch096 sample was classified in the advanced/silicic alteration zone, and based on spectral information was classified more into the silicic alteration zone due to its high alunite content. According to HyMap classification, it is eventually classified in the silicic alteration zone. This rock is a clear example of the need to use all sources of information for classification. PRISMA classifies this pixel as kaolinite-smectite, categorizing this section as a more external propylitic alteration zone.

MRE02033 rock-sample falls 88 meters far away from the cross-section. By VISU and spectral information is classified in the silicic alteration zone. HyMap pixel where this rock-sample is located is classified also in the silicic zone, meanwhile PRISMA pixel classifies it wrongly as kaolinite-smectite.

#### Comparison P.C.4

Throughout these sections PRISMA and HyMap representation is quite distinct. In the part of the cross-section where there is no rock-sample PRISMA classifies these pixels as kaolinite-smectite (propylitic alteration zone) while HyMap classifies this part of the cross-section as a more altered zone with the presence of alunite and more advanced alteration zones with dickite.

MRE02034 rock-sample is classified with VISU and spectral information as kaolinite-smectite. However, HyMap and PRISMA pixels are classified as dickite, which makes it a more inner zone.

The following part of the cross-section where MRE01011 rock-sample is located coincides with HyMap pixel. This part also coincides with PRISMA cross-section in the same alteration zone, however the pixel classified by PRISMA falls in an outer part of the alteration zone (propylitic).

To the southern part of the section is located MRE01051 rock-sample, representing according to VISU and spectral classification the outermost part of the alteration zones. This rock-sample is classified as kaolinite and pyrophyllite+alunite by HyMap or PRISMA, respectively.

MRE01052 rock-sample was hard to classify by just using spectrometer information due to its high montmorillonite content. Based on VISU information, it was classified as belonging to silicic zone. Based on PRISMA and HyMap information, they both confirm the classification made by VISU description.

#### Comparison P.T.1

At the beginning of the cross-section (in the North-Western part) PRISMA classifies this part as a highly inner alteration zone, in contrast with HyMap which classifies it as a less altered and more intermediate zone.

Rock-sample 04MRE225a is not well classified by either of the image sources. HyMap and PRISMA pixels classify it as nontronite. Based on both VISU and spectral information, this sample is classified in the supergene zone.

04MRE033 rock-sample is classified as alunite by HyMap. However, according to VISU and spectral classification in the laboratory, this rock-sample belongs more to the advanced argillic alteration zone. PRISMA shows this part as a much lower altered zone, classifying this pixel as montmorillonite (yellow colour).

#### Comparison P.T.2

This section is well represented by both PRISMA and HyMap cross-sections. This section serves as a good example to appreciate the differences in quality in between the less resolution PRISMA images and the higher detailed HyMap results. PRISMA classification leads to believe that alunite abruptly appears around kaolinite+smectite, being in direct contact and rejecting the existence of halos characteristic of the epithermal alteration zones. However, HyMap shows how this more altered zones are surrounded by advanced and intermediate argillic alteration zones with minerals as dickite and pyrophyllite+alunite.

Rock-sample 05ch053 falls far away from the cross-section (113 meters). PRISMA pixel representing this sample classifies it as it is classified by VISU and spectral information from the laboratory (in the propylitic alteration zone). However, HyMap pixel classifies it in a more intermediate zone (as kaolinite).

Q1-1 and MRE02055 rock samples fall closer to the cross-section (30 meters far away). These rock-samples are classified both in the supergene alteration zone by PRISMA, HyMap, VISU and spectral laboratory information.

#### Comparison P.T.3

The cross-section classification based on rock-samples information is too poor since there is only one sample available (04MRE125) of this section in the Western part and it is 40 meters far away. Pixels from HyMap and PRISMA classify this sample wrongly. However, the closest pixels in HyMap surrounding this sample are classified as a high-altered zone, which fits more with VISU and spectral classification (supergene zone).

Central parts of HyMap and PRISMA sections are well classified, although PRISMA in a more general way. At the more Eastern part of the cross-sections both tend to colours representing more outer altered zones (blue and yellow).

For a more visible comparison of the accuracy of both HyMap and PRISMA images, the following table was created (Table 5.3), comparing the classification realized using laboratory spectra and VISU rock-samples (see Apendix 2 for location) with the one performed by SAM classification. Samples coloured in the table show pixels that coincide with the original classification (laboratory spectroscopy), being a total of 58% from HyMap images, and a total of 42% from the use of PRISMA image.

	Laboratory spectroscopy			HyMap	PRISMA
	Rock-sample	Rock classification	Alteration zone	Alteration zone	Alteration zone
P.C.1	04MRE044	Andesite/dacite	Propylitic	-	Propylitic
	MRE02019	Andesite/dacite	Propylitic	Interm/adv argillic	Silicic/Supergene
	MRE02021pm1	Andesite/dacite	Propylitic	-	Silicic/Supergene
	MRE02022pm1	Monmorillonite	Propylitic	Interm/adv argillic	Propylitic
	MRE02023pm1	Kaolinite	Interm/adv argillic	Interm/adv argillic	Propylitic
	MRE02025pm1	Halloysite	Silicic/Supergene	Silicic/Supergene	Silicic/Supergene
	MRE02026pm1	Illite	Interm/adv argillic	Interm/adv argillic	Silicic
P.C.2	MRE02053pm2	Dickite	Interm/adv argillic	Silicic/Supergene	Interm/adv argillic
	05ch095	Vuggy quartz	Silicic/Supergene	Silicic/Supergene	Silicic/Supergene
	05ch094	Vuggy quartz	Silicic/Supergene	Silicic/Supergene	Interm/adv argillic
	Mex1-pm3	Alunite	Silicic/Supergene	Silicic/Supergene	Interm/adv argillic
	05ch093	Vuggy quartz	Silicic/Supergene	Silicic/Supergene	Interm/adv argillic
P.C.3	05ch096	Alunite	Silicic/Supergene	Silicic/Supergene	Propylitic
	MRE02033	Opal	Silicic/Supergene	Silicic/Supergene	Propylitic
P.C.4	MRE02034pm1	Kaolinite	Interm/adv argillic	Propylitic	Interm/adv argillic
	MRE01011pm1	Quartz	Silicic/Supergene	Interm/adv argillic	Propylitic
	MRE01051pm	Andesite/dacite	Propylitic	Interm/adv argillic	Interm/adv argillic
	MRE01052	Quartz	Silicic/Supergene	Silicic/Supergene	Silicic/Supergene
P.T.1	04MRE225a	Kaolinite	Interm/adv argillic	-	Propylitic
	04MRE003-1	Vuggy silica	Silicic/Supergene	Silicic/Supergene	Propylitic
P.T.2	05ch053	Andesite/dacite	Propylitic	Interm/adv argillic	Propylitic
	MRE02055pm2	Alunite	Silicic/Supergene	Silicic/Supergene	Interm/adv argillic
	Q1-1	Alunite	Silicic/Supergene	Silicic/Supergene	Silicic/Supergene
P.T.3	04MRE125	Kaolinite	Interm/adv argillic	Interm/adv argillic	Interm/adv argillic

Table 5.3. Comparison of classification from different sources (laboratory spectra, HyMap images and PRISMA image).

## 6. DISCUSSION

Coming back to the main objectives of this study (Chapters 1.4 and 1.5), one of them was determining the rock-types that differentiate the sub-areas identified within Rodalquilar and describing the distribution and diffusion of the minerals present in the area. After using Spectral Angle Mapper analysis imaging spectrometer data recorded by PRISMA, it was possible to map the distribution of the hydrothermal alteration mineralogy and, hence, trying to answer this questions.

PRISMA map classification shows a zone of extensive argillically altered rocks trend from East to West through the caldera and is well delineated by HyMap and PRISMA. These mineralisations are located mainly in rhyolitic tuffs and domes. The main minerals determining the differenced sub-areas identified in these two deposits were alunite and opal, being alunite more abundant in Los Tollos deposit and opal in Cerro del Cinto deposit. The extensive alunite presence in Los Tollos deposit can be mainly related to a supergene blanket without mineralization Arribas et al., 1995. This second supergene state of acid sulphate alteration is found mainly within shallow intensely altered areas which surround, or are sometimes superimposed on the central core of the hypogene advanced argillic alteration (G., & Pillars, H.)

Advanced and intermediate argillic minerals (those identified as dickite, pyrophyllite-alunite and kaolinite) are more abundant in the Western part of the map, characterizing Cerro del Cinto deposit, while their presence is more poor in Los Tollos deposit.

Nontronite, montmorillonite and kaolinite+smectite, which corresponds to propylitic alteration zones around the epithermal gold deposits, are abundant in the northern and eastern part of the scene. This signature representing the background, was found more abundant in Los Tollos area than in Cerro del Cinto.

Influence and classification of faults was also aim of this study. Faults systems that formed during each phase of the caldera cycle provide the structural control for ore deposits within or near the caldera (Arribas et al., 1989). At the end of the caldera cycle (phase 4), both calderas (Lomilla and Rodalquilar) were cut by north-trending normal faults along the strike-slip Cabo de Gata fault, which reactivated north-trending radial faults in the wall of Lomilla caldera. Emplacement of a dioritic stock east of Lomilla caldera domed and opened the radial and north-trending fault zones, which resulted on degassing from magma and acid sulphate alteration leading to the development of large zones of vuggy silica enveloped in alunite and kaolinite along east ring fault, the radial faults and the north trending faults in the east wall of the Lomilla, which is visible in PRISMA map classification (Figure 5.13), where the silicic alteration zone (represented by the presence of opal, red colour) is concentrated in Cerro del Cinto deposit and some of them following these north-trending and radial faults (white and black colours, respectively), while Los Tollos deposit does not show that characteristics.

The late north-trending faults (white lines in the map, Figure 5.13) were active during emplacement of the dioritic stock which was the source of the alteration associated with the hydrothermal gold alunite deposits. Early radial faults (black thin lines in the map, Figure 5.13) provided the structural controls for the gold alunite deposits, especially those reactivated and opened during structural doming (Arribas et al., 1989). These gold alunite deposits (represented by purple colour in the map) seem to be not well represented by PRISMA due to their inexistence along these radial faults.

Comparison along line-transects crossing Los Tollos and Cerro del Cinto deposits between results derived by remote sensing and ground data was found an interesting way to study the agreement of the outcome information. Cross-sections based in rock-samples show an irregular pattern of the alteration zone distribution, which may be indicating the presence of veinlets intruding the Rodalquilar area. Results from both PRISMA and HyMap differ from the classification accomplished in the laboratory. PRISMA shows the least favourable results, being more than the half of these pixels wrongly classified and thus, wrongly categorizing the alteration zone they belong to. For example, rock-sample 05ch096 is classified as alunite by VISU and spectroscopy studies (and also by HyMap images) corresponding to the core of the alteration, the silicic/supergene alteration zone, however PRISMA classifies the pixel where this sample is located as kaolinite+smectite, locating it at the outermost part of the alteration zone (propylitic). Differences between poorly-highly crystalline kaolinite and hydrate-dehydrated halloysite to separate silicic and supergene alteration zones were harder to prove by using PRISMA spectral signatures, reason why silicic and supergene zones were grouped together in PRISMA and HyMap SAM classification.

Comparing with other sources of information, in this case with the alteration map modified after Arribas et al., 1995, it becomes visible how (in a rougher way when using PRISMA images) this halos of alteration zone that belong to higher levels of alteration become more abundant to zones affected by faults, which are linked to have created ideal fluid pathways for hydrothermal flows to pass through and deposit its precious cargo.

These halos of highly altered epithermal zones (red, pink and granite areas) indicate an alteration assemblage formed under low pH and high temperatures which evolve to a low-pressure-temperature propylitic alteration zone around them (represented by blue and green colours).

## 7. CONCLUSIONS

Local spectral library of the area of Los Tollos and Cinto deposits was completed. Interpretation of the absorption features related to rock type performed in the laboratory was an easier task than the interpretation done from PRISMA images.

Spectral signature quality from PRISMA images limits spectral classification and makes a harder task to identify and separate minerals, especially due to those gaps situated around 1400 nm and between 1800 and 2000 nm, ranges that were considered fundamental for many minerals differentiation. These spectral regions are due to the atmospheric absorptions from water vapour and gases, primarily H<sub>2</sub>O, O<sub>3</sub> and CO<sub>2</sub> (Zdunkowski et al., 2009).

Having a non-unique spectral response leads to a later treatment with caution and interpretation of results based principally on knowledge for the geology in the area. Therefore, spectral mapping strongly depends on field observations and information.

Classification from PRISMA images is poor and transitions in between alteration zones are abrupt. In many occasions, there are no transitions in between the highest and the lowest altered zones. Therefore, using PRISMA images is still a matter that cannot be done without other sources of information.

The accuracy assessment stage continues being problematic in every remote sensing application due to issues related to satellite accuracy, images resolution, geolocation, sample size and quality of ground data. Comparison with geological maps shows differences in between these sources. While geological maps are always existing of large groups of units, images classification show more patterns of transition zones.

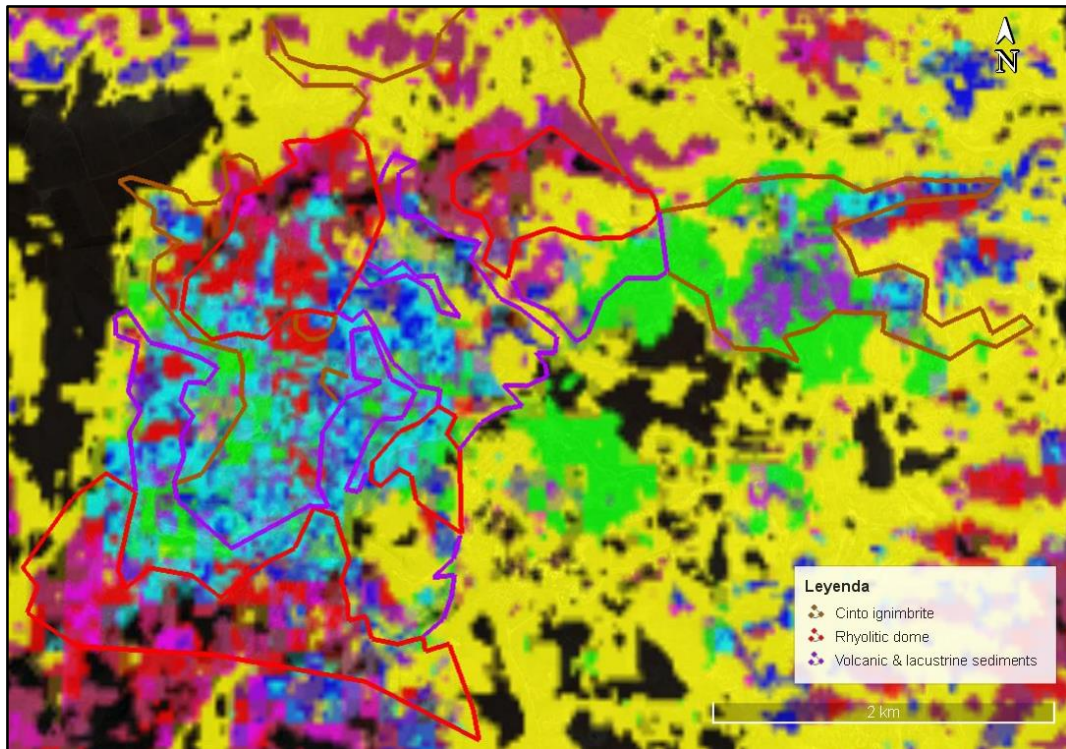


Figure 7.1. Geological units (Source IGME) on top of PRISMA SAM classification.

## 8. RECOMMENDATIONS

Some of the recommendations for future projects using PRISMA images would be using a different classification method for mapping, as for example Linear Spectral Unmixing or Maximum Likelihood classification. It might be useful to compare results in between PRISMA images and check whether applying an alternative method is beneficial for the outcome.

Another recommendation would be masking also roads, waterbodies and, if possible, agricultural fields from the image before carrying out a geological image interpretation to avoid confusion or wrong classifications.

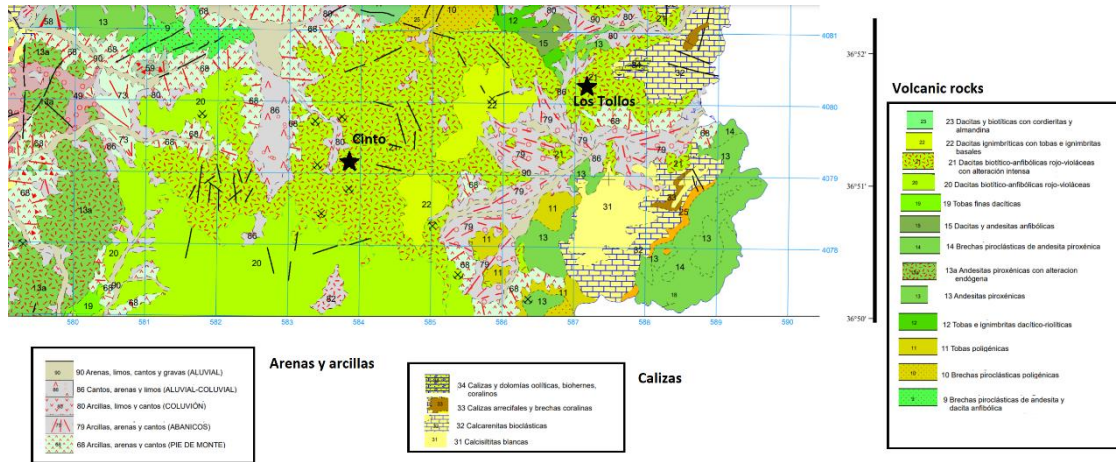
## LIST OF REFERENCES

- Abera, M. (2020). Characterization of Rock Samples Using Swir-Lwir Hyperspectral Imaging techniques- an Example of the High Epithermal system of Rodalquilar, Southeast Spain. *Faculty of Geo-Information Science and Earth Observation of the University of Twente*.
- Arribas, A. (1993). Mapa geológico del distrito minero de Rodalquilar, Almería. March.
- Arribas, A. (1995). Geology, geochronology, fluid inclusions, and isotope geochemistry of the Rodalquilar gold alunite deposit, Spain. *Economic Geology*, 90(4), 795–822. <https://doi.org/10.2113/gsecongeo.90.4.795>
- Arribas, A. (1995). Characteristics of high-sulfidation epithermal deposits, and their relation to magmatic fluid. *Mineralogical Association of Canada Short Course Series*, 23(November), 419–454.
- Agenzia Spaziale Italiana. (n.d.). PRISMA. ASI.IT. <https://www.asi.it/en/earth-science/prisma/>
- Bedini, E. (2009). Mapping lithology of the Sarfartoq carbonatite complex, southern West Greenland, using HyMap imaging spectrometer data. *Remote Sensing of Environment*, 113(6), 1208–1219. <https://doi.org/10.1016/j.rse.2009.02.007>
- Bedini, E., van der Meer, F., & van Ruitenbeek, F. (2009). Use of HyMap imaging spectrometer data to map mineralogy in the Rodalquilar caldera, southeast Spain. *International Journal of Remote Sensing*, 30(2), 327–348. <https://doi.org/10.1080/01431160802282854>
- Bertels, L., Deronde, B., Kempeneers, P., Provoost, S., & Tortelboom, E. (2005). Potentials of airborne hyperspectral remote sensing for vegetation mapping of spatially heterogeneous dynamic dunes, a case study along the Belgian coastline. “Dunes and Estuaries 2005” - *International Conference on Nature Restoration, September*, 153–163.
- Carranza, E. J. M., van Ruitenbeek, F. J. A., Hecker, C., van der Meijde, M., & van der Meer, F. D. (2008). Knowledge-guided data-driven evidential belief modeling of mineral prospectivity in Cabo de Gata, SE Spain. *International Journal of Applied Earth Observation and Geoinformation*, 10(3), 374–387. <https://doi.org/10.1016/j.jag.2008.02.008>
- Choe, E., van der Meer, F., van Ruitenbeek, F., van der Werff, H., de Smeth, B., & Kim, K. W. (2008). Mapping of heavy metal pollution in stream sediments using combined geochemistry, field spectroscopy, and hyperspectral remote sensing: A case study of the Rodalquilar mining area, SE Spain. *Remote Sensing of Environment*, 112(7), 3222–3233. <https://doi.org/10.1016/j.rse.2008.03.017>
- Corp, H. (2004). *HyEurope 2004 Summary Report*.
- Denver, P. (n.d.). Cerro del Cinto- (short route).
- Fulignati, P. (2020). Clay minerals in hydrothermal systems. *Minerals*, 10(10), 1–17. <https://doi.org/10.3390/min10100919>
- Garg, p. (2020). Effect of contamination and adjacency factors on snow using spectroradiometer and hyperspectral images. *Hyperspectral Remote Sensing :167-196*, DOI: 10.1016/B978-0-08-102894-0.00016-4</opt>
- Hernández Ortiz, F. (2016). El cierre de las minas de oro de de Rodalquilar (1966): Auge y declive de la planta Denver. *De Re Metallica (Madrid): Revista de La Sociedad Española Para La Defensa Del Patrimonio Geológico y Minero*, 26, 9–17. <https://dialnet.unirioja.es/servlet/articulo?codigo=6004311>
- Huete, A. R. (1988). A soil-adjusted vegetation index (SAVI). *Remote Sensing of Environment*, 25(3), 295–309. [https://doi.org/10.1016/0034-4257\(88\)90106-X](https://doi.org/10.1016/0034-4257(88)90106-X)
- J. Kramer, H. (2002). PRISMA (Hyperspectral) - *eoPortal Directory*. Earth Esa. <https://earth.esa.int/web/eoportal/satellite-missions/p/prisma-hyperspectral>
- Kauth, R.J. & Thomas, G.S. (1976). The tasseled Cap - A Graphic Description of the Spectral-Temporal Development of Agricultural Crops as Seen by Landsat. *Environmental Research Institute of Michigan*

- Kruse, F. A., A. B. Lefkoff, J. B. Boardman, K. B. Heidebrecht, A. T. Shapiro, P. J. Barloon, and A. F. H. Goetz. "The Spectral Image Processing System (SIPS) - Interactive Visualization and Analysis of Imaging Spectrometer Data." *Remote Sensing of Environment* 44 (1993): 145-163.
- Kruse, F., Boardman, J., Lefkoff, A. B., Young, J., & Kierein-Young, K. (2000). HyMap: An Australian hyperspectral sensor solving global problems-results from USA HyMap data acquisitions. *Proceedings of the 10th Australasian Remote Sensing and Photogrammetry Conference*, 18–23. [http://hgimaging.ipower.com/PDF/kruse\\_10ARSPC\\_hymap.pdf](http://hgimaging.ipower.com/PDF/kruse_10ARSPC_hymap.pdf)
- Liu, J. (2005). *REMOTE SENSING | Passive Sensors. Encyclopedia of Geology* :431-439, DOI: 10.1016/B0-12-369396-9/00510-4</opt>
- L3 Harris Geospatial. (n.d.). *Spectral Angle Mapper*.  
<https://www.l3harrisgeospatial.com/docs/spectralanglemapper.html>
- Madrid, R., & Luis, A. (2014). Geology, alteration, mineralization and hydrothermal evolution of the La Bodega-La Mascota deposits, California-Vetas Mining District, Eastern Cordillera of Colombia, Northern Andes.
- Oppelt, N., & Mauser, W. (2007). Airborne visible / infrared imaging spectrometer AVIS: Design, characterization and calibration. *Sensors*, 7(9), 1934–1953.  
<https://doi.org/10.3390/s7091934>
- Pontual, S., Merry, N., & Gamson, P., (1997). Spectral Interpretation Field Manual.
- P. N. BIERWIRTH (1990) Mineral mapping and vegetation removal via data-calibrated pixel unmixing, using multispectral images, *International Journal of Remote Sensing*, 11:11, 1999-2017, DOI: 10.1080/01431169008955157
- Rytuba, J. J., Rye, R. O., Cunningham, C. G., Podwyssocki, H., Kelly, W. C., Sr, A. A., McKee, E. H., & Smith, J. G. (1989). *Antonio Arribas Jr. I Open-File Report 89-327 This report is preliminary and has not been reviewed for conformity with U. S. Geological Survey editorial standards*.
- Rytuba, J. J., Arribas Jr., A., Cunningham, C. G., McKee, E. H., Podwyssocki, M. H., Smith, J. G., Kelly, W. C., & Arribas, A. (1990). Mineralized and unmineralized calderas in Spain; Part II, evolution of the Rodalquilar caldera complex and associated gold-alunite deposits. *Mineralium Deposita*, 25(1), 29–35.  
<http://www.springerlink.com/index/j55110300r6777j7.pdf>
- Rytuba, J. J. (1994). Evolution of volcanic and tectonic features in caldera settings and their importance in the localization of ore deposits. *Economic Geology*, 89(8), 1687–1696.  
<https://doi.org/10.2113/gsecongeo.89.8.1687>
- Sintes, I. G. (2016). *Filón 340, Rodalquilar, Níjar, Almería*. 1–48.
- Tucker, C. J., Pinzon, J. E., Brown, M. E., Slayback, D. A., Pak, E. W., Mahoney, R., Vermote, E. F., & El Saleous, N. (2005). An extended AVHRR 8-km NDVI dataset compatible with MODIS and SPOT vegetation NDVI data. *International Journal of Remote Sensing*, 26(20), 4485–4498. <https://doi.org/10.1080/01431160500168686>
- Tun, M. M., Warmada, I. W., Harijoko, A., Al-Furqan, R., & Watanabe, K. (2015). Characteristics of Hydrothermal Alteration in Cijulang Area, West Java, Indonesia. *Journal of Applied Geology*, 7(1), 1–9. <https://doi.org/10.22146/jag.16917>
- Van der Meer, F. D., van der Werff, H. M. A., & van Ruitenbeek, F. J. A. (2014). Potential of ESA's Sentinel-2 for geological applications. *Remote Sensing of Environment*, 148, 124–133. <https://doi.org/10.1016/j.rse.2014.03.022>
- Van der Werff, H., & van der Meer, F. (2016). Sentinel-2A MSI and Landsat 8 OLI provide data continuity for geological remote sensing. *Remote Sensing*, 8(11).  
<https://doi.org/10.3390/rs8110883>
- Van der Meer, F., Kopačková, V., Koucká, L., van der Werff, H. M. A., van Ruitenbeek, F. J. A., & Bakker, W. H. (2018). Wavelength feature mapping as a proxy to mineral chemistry for investigating geologic systems: An example from the Rodalquilar epithermal system.

- International Journal of Applied Earth Observation and Geoinformation*, 64 (September 2017), 237–248. <https://doi.org/10.1016/j.jag.2017.09.008>
- Vries, M. J. Van De. (2013). *Hymap images as a base for geologic interpretation and gypsum variation detection in Carboneras, southern Spain*. studentnumber 3251608, 0–58.
- Wur, J. P. G. W. C. (n.d.). *Remote Sensing*.
- Ylagan, R. F., Altaner, S. P., & Pozzuoli, A. (1996). Hydrothermal alteration of a rhyolitic hyaloclastite from Ponza island, Italy. *Journal of Volcanology and Geothermal Research*, 74(3–4), 215–231.
- Zdunkowski, W., Trautmann, T., & Bott, A. (2009). Absorption by gases. *Radiation in the Atmosphere*, 276–332. <https://doi.org/10.1017/cbo9780511535796.009>

Appendix 1. Description of geological units in Rodalquilar



1. Metamorfisim of Betic Units

1.1. Neogene volcanic rocks

1.1.1. Calcoalcaline vulcanism

1.1.1.1. Poligenic tobas (11)

They consist of centimetric stones of both types of andesites (anfibolic and piroxenic) in a thin cineritic or tuffaceous matrix, or of small pyroclasts called lapilli with a more lacking in matrix. They are spread through the whole field of the map.

1.1.1.2. Piroxene andesites (13)

They are one of the most characteristic and basic materials in Cabo de Gata area. They present a serial porfidic texture. It is formed by plagioclase and pyroxene phenocrysts which proportion rarely surpasses the 50% of the rock. The matrix, with a high proportion of glass, presents a variable number of tabular microlites of plagioclase and piroxenes disposed intertwined or with fluency around the phenocrysts.

In the SW of the map, these materials (13a) show an intermediate to high hipogenic alteration with alunization, carbonatation, potasification and siicification.

1.1.1.3. Piroclastic breccias of piroxenic andesite (14)

They form chaotic aspect outcrops of piroxenic andesite blocks, angulars, decametric, with a same composition matrix. According to authors as Sanchez Cela (1968), Coello and Castañon (1965) and Fuster et al. (1965), its genesis could be in a brecciation, in the emission channel, of the homogene materials due to its own viscosity and gigh magma volatile content.

1.1.1.4. Anfibolic andesites and dacites (15)

In the microscope they present porfidic texture generally serial, with a matrix that oscillates from microcrystalline to vitreous. They consist of variable quantity of quartz, amphibole and biotite. In less proportion there is ortho- and cliropiroxenes, and opaque minerals, apatite and zircon as minor common accessories.

Quartz is normally found in rounded crystals with marginal corrosion. Phenocrystals can be from numerous to non-existent, depending on the rock type (andecite or dacite).

### 1.1.2. Calcoalkaline vulcanism? Rocks with endogene alteration

#### 1.1.2.1. Biotitic-anfibolic dacites (20)

They present a massive and homogene facie, highlighting their typical big rounded phenocrystals of quartz and plagioclase. Their color is red-violet, quite characteristic.

Plagioclases are normally smaller than quartz crystals and with partial or total alteration to alunite.

#### 1.1.2.2. Biotitic-anfibolic dacites highly altered (21)

The unit described before evolves laterally to the intensely altered rocks of Rodalquilar, in which the famous gold mineralizations are localized. These alterations are accentuated, occurring an extreme silicification and a complex process of neoformation of minerals from clay and similar (kaolinite, dickite, etc.). Despite everything, its typical structure of phenocrystals of quartz and plagioclase are still recognisable.

Field data indicates that these rocks lie as powerful flows on top of the previous described calcoalkaline materials. Probably, its emission source was in the area of Rodalquilar.

#### 1.1.2.3. Ignimbritic dacites with tobas and basal ignimbrites (22)

Basally, they consist of well-layered tuffs with some metric pyroclastic breccias. To the top they evolve to ignimbrite facies with centrimetric greenysh flames. On the top of the formation they turn into green dacited with columnar disjunction with some still recognisable flame structure; its thickness reaches 50m.

### 1.2. Neogene sedimentary cover

#### 1.2.1. Arrecifal complex

The transgression that initiates on the volcanic basement and that originates these deposits reaches its maximum development in the Messiniense. The level of the sea rapidly raises invading a complex relief, when this ascent is stops (still-stand) a large part of the volcanic cones and the Betic basement are covered by water, being colonized by corals. These corals triggered an important development of arrecifal complex in all the region.

##### 1.2.1.1. Marls (31)

They are white, bioturbated marls with high content in planktonic foraminifera, spicules of sponges, ostreids. They are well-layered and barely cemented.

The absence of important tectonic in the area along with the great exposure and conservation of the outcrops, permits the recognition of the original morphology of the arrecifal system.

##### 1.2.1.2. Calcarenites (32)

Volumetrically it is the most abundant facies from the Arrecifal complex. It is composed by bioclastic bioturbated grainstones-packstones. Mega-crossbedding is frequent. Calcarenites are well-layered, reaching 50-60 cm of thickness, with parallel lamination and graded bedding in some cases.

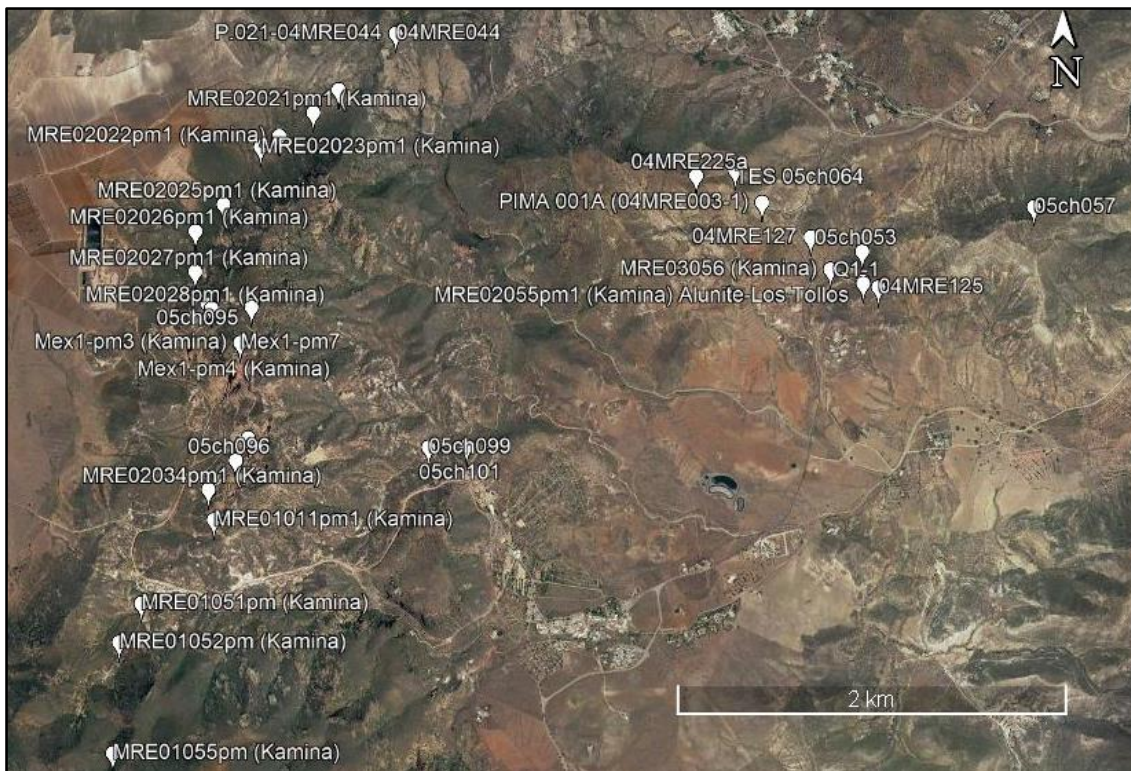
##### 1.2.1.3. Arrecifal limestones (33)

In this section it is included both the limestones that form the reef as the breccias formed by fragments and blocks of reef, which are chaotic, not classified and not layered along with molluscs and bryozoos.

### 1.3. Quaternary

- 1.3.1. Clay, sand and river stones (Pie de monte) (68)
- 1.3.2. Clay, sand and river fans (79)
- 1.3.3. Clay, limes and stones colluvium (80)
- 1.3.4. Stones, sand and limes alluvial-colluvial (86)

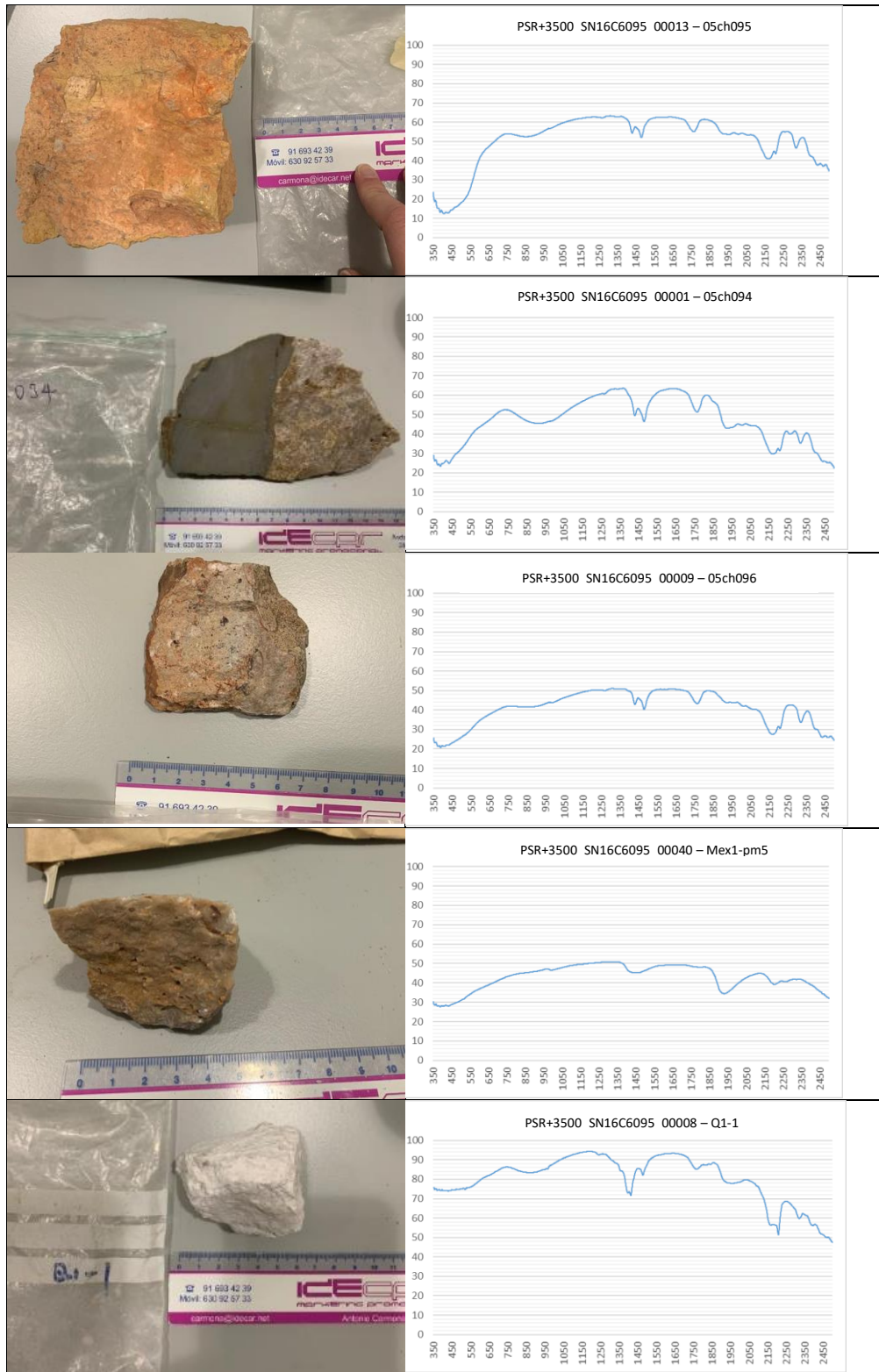
Appendix 2. Rock-samples location (The sample codes MRE and CH in the entire paper stand for Mineral Resource Exploration and Chris Hecker respectively.)

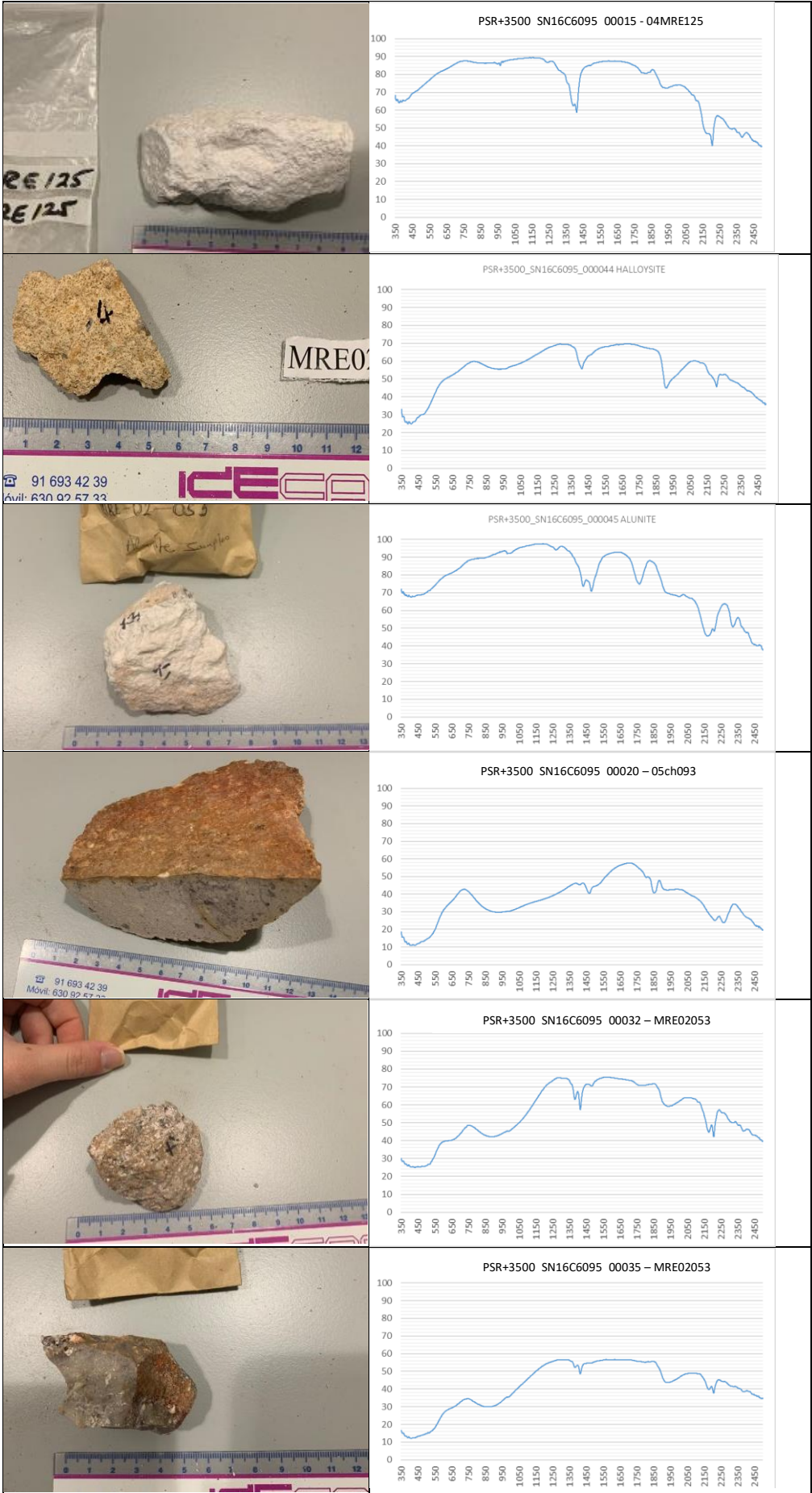


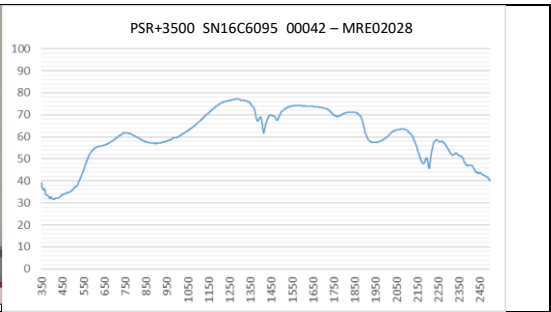
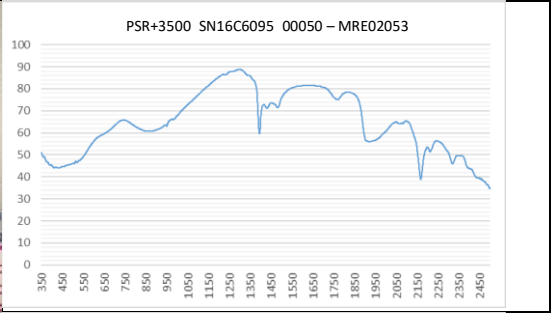
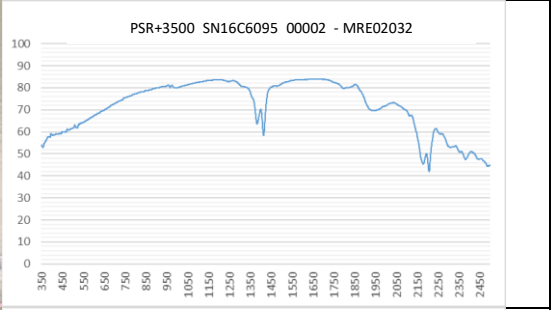
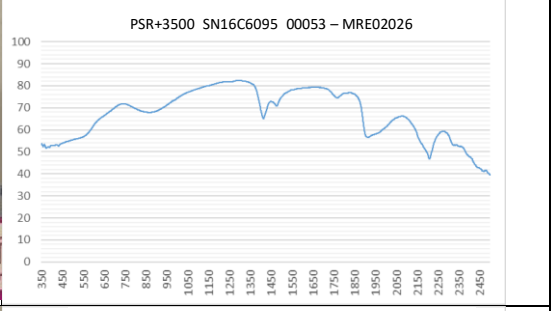
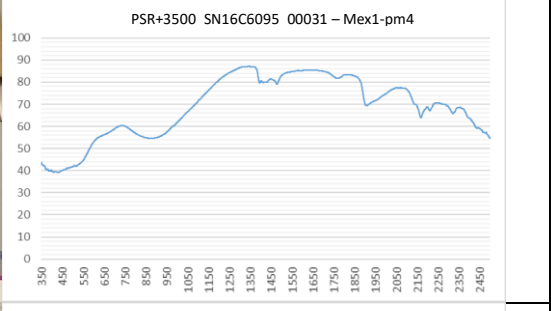
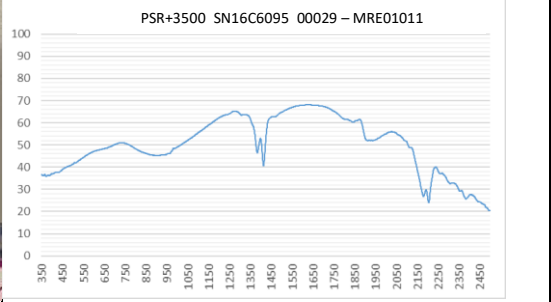
	Station Name	Easting	Northing	Samples name
<b>VISU SIZE</b>	05ch094	583819	4079829	05ch094
	04MRE003	586440	4080391	PIMA 001A (04MRE003-1)
	05ch101	584933	4079130	05ch101
	05ch099	584737	4079121	05ch099
	AQ1	586965	4079982	Q1-1
	05ch096	583746	4079044	05ch096
	05ch057	587839	4080382	05ch057
	05ch095	583823	4079843	05ch095
	04MRE125	587043	4079963	04MRE125
	05ch053	586958	4080146	05ch053
	04MRE225a	586100	4080525	04MRE225a
	05ch093	583961	4079654	05ch093
	04MRE044	584547	4081237	P.021-04MRE044
	04MRE044	584547	4081237	04MRE044
	MRE01052	583155	4078106	MRE01052pm (Kamina)
	04MRE044	584547	4081237	P.021-04MRE044
	MRE02021	584127	4080828	MRE02021pm1 (Kamina)
	MRE01011	583636	4078738	MRE01011pm1 (Kamina)
	MRE01051	583267	4078307	MRE01051pm (Kamina)
	MRE01001	583763	4079647	Mex1-pm4 (Kamina)
	MRE02053	583595	4079841	MRE02053pm3 (Kamina)
	MRE02022	583953	4080707	MRE02022pm1 (Kamina)
	MRE02053	583595	4079841	MRE02053pm1 (Kamina)
	MRE02023	583858	4080649	MRE02023pm1 (Kamina)
	MRE02034	583607	4078893	MRE02034pm1 (Kamina)
	MRE01001	583763	4079647	Mex1-pm5 (Kamina)
	MRE02028	583614	4079820	MRE02028pm1 (Kamina)
	MRE01055	583128	4077539	MRE01055pm (Kamina)
	MRE02025	583670	4080354	MRE02025pm1 (Kamina)
	MRE02055	586962	4079992	MRE02055pm1 (Kamina) Alunite-Los Tollos
	MRE02055	586962	4079992	MRE02055pm2 (Kamina) Alunite - Los Tollos
	MRE02055	586962	4079992	MRE02055pm3 (Kamina) Alunite - Los Tollos
	MRE02019	584428	4081025	MRE02019pm1 (Kamina)
	MRE02033	583796	4078944	MRE02033pm1 (Kamina)
MRE01001	583763	4079647	Mex1-pm3 (Kamina)	
MRE02053	583595	4079841	MRE02053pm2 (Kamina)	
MRE02032	583808	4079159	MRE02032pm1	
MRE02026	583527	4080215	MRE02026pm1 (Kamina)	
MRE02027	583528	4080008	MRE02027pm1 (Kamina)	

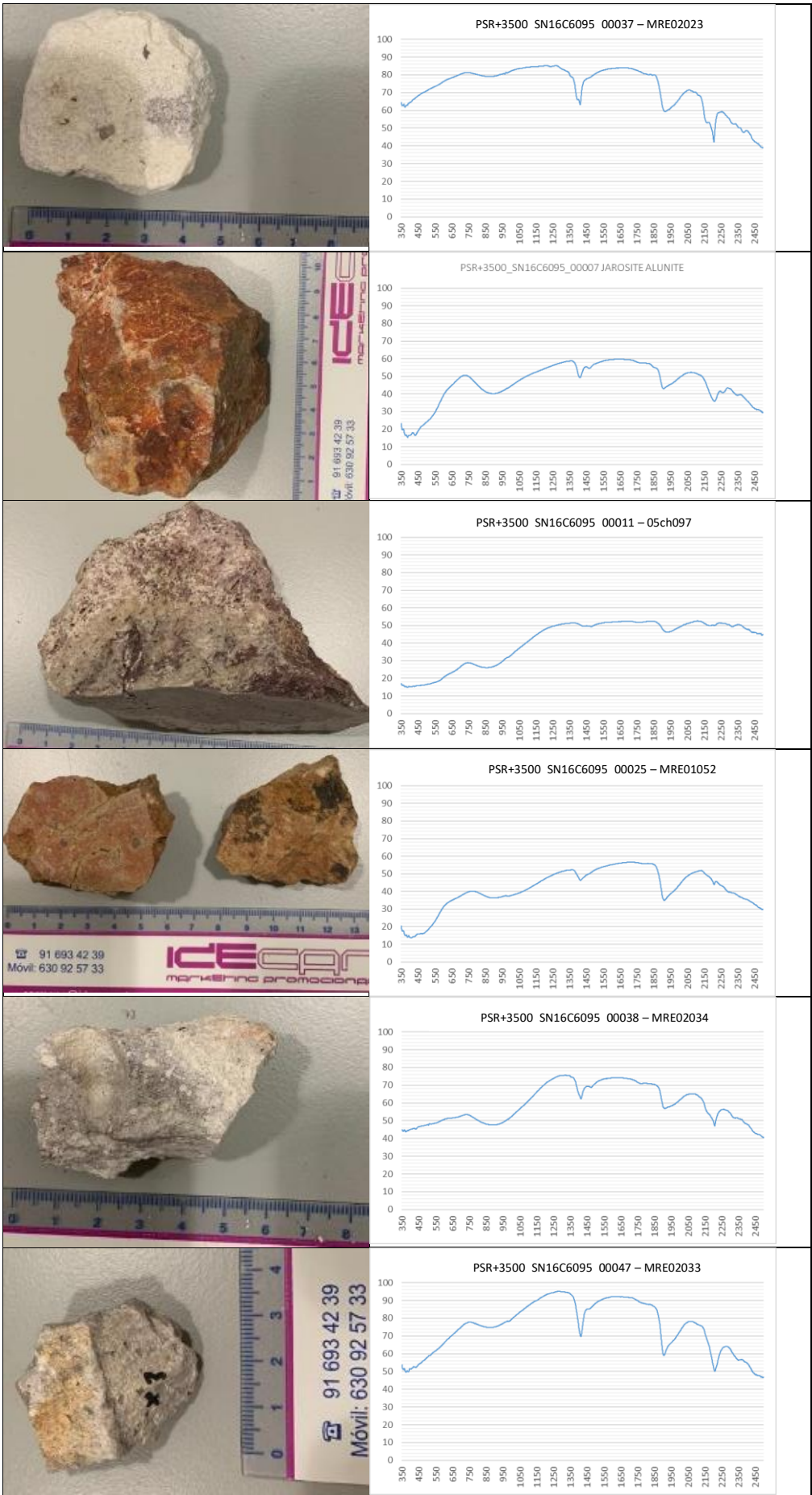
	<b>Station Name</b>	<b>Easting</b>	<b>Northing</b>	<b>Samples name</b>
<b>POWDER SAMPLES</b>	MRE01053	583236	4077924	MRE01053pm (Kamina)
	MRE03056	586795	4080052	MRE03056 (Kamina)
	MRE02029	583918	4079684	MRE02029pm1 (Kamina)
	MRE02031	583956	4079303	MRE02031pm1 (Kamina)
	MRE01051	583267	4078307	MRE01051pm (Kamina)
	MRE02053	583595	4079841	MRE02053pm2 (Kamina)
	MRE03023	581364	4079128	MRE03023pm (Kamina)
	MRE02020	584256	4080946	MRE02020pm1-r (Kamina)
	MRE01050	583237	4078377	MRE01050pm (Kamina)
	MRE01012	583358	4078762	MRE01012pm1 (Kamina)
	MRE01049	583292	4078567	MRE01049pm (Kamina)
	MRE01070	583336	4079772	MRE01070pm2 (Kamina)
	MRE02053	583595	4079841	MRE02053pm1 (Kamina)
	MRE01011	583636	4078738	MRE01011pm1 (Kamina)
	MRE02030	583987	4079500	MRE02030pm1 (Kamina)

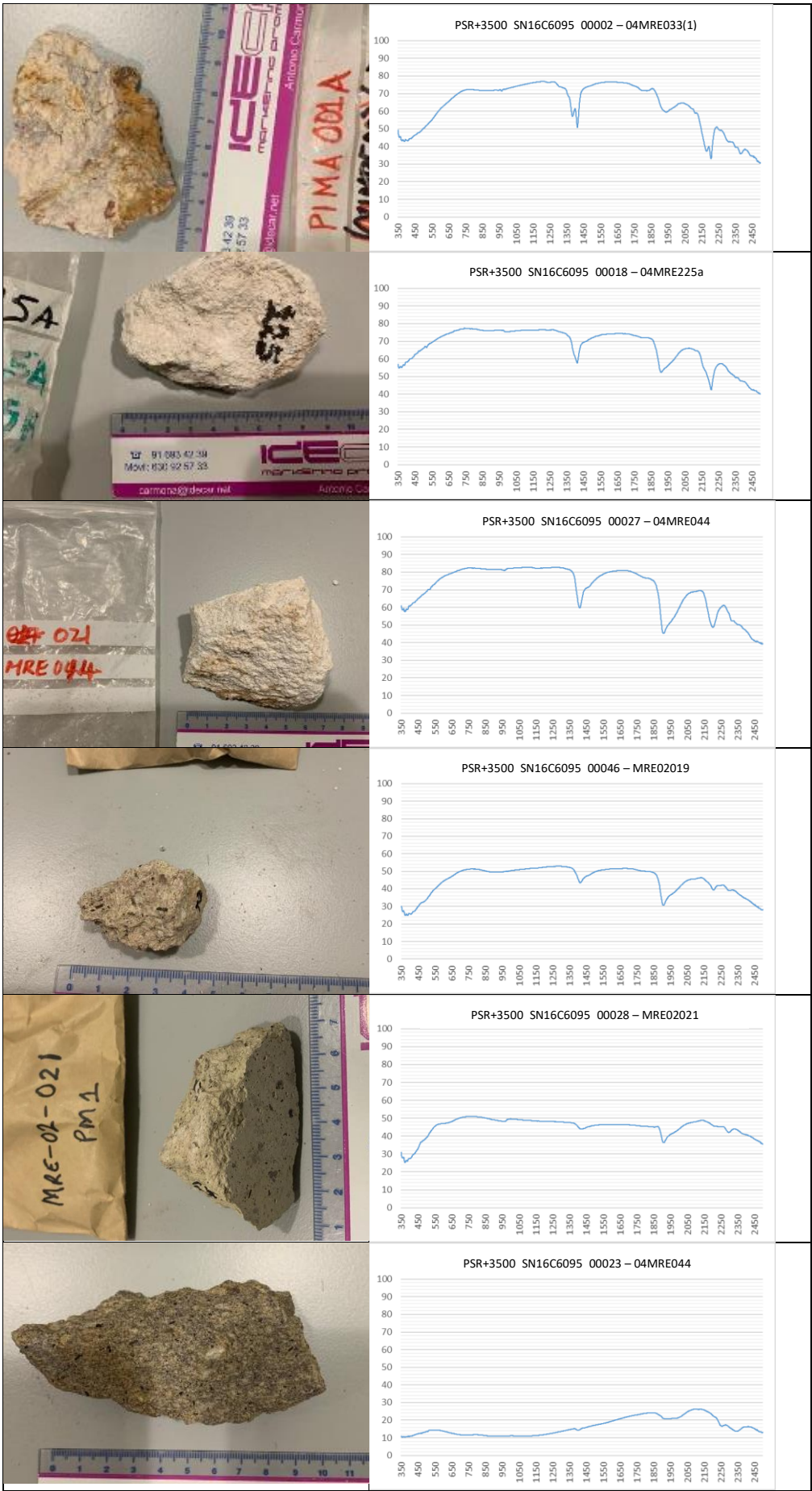
Appendix 3. List of minerals and spectral signature.

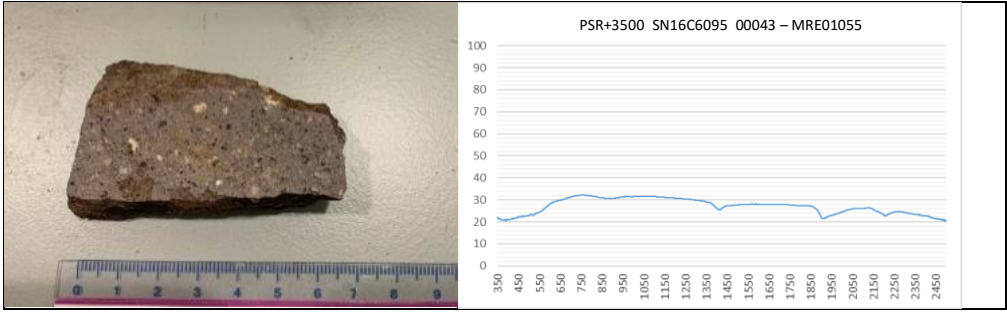




	<p>PSR+3500 SN16C6095 00042 – MRE02028</p> 
	<p>PSR+3500 SN16C6095 00050 – MRE02053</p> 
	<p>PSR+3500 SN16C6095 00002 - MRE02032</p> 
	<p>PSR+3500 SN16C6095 00053 – MRE02026</p> 
	<p>PSR+3500 SN16C6095 00031 – Mex1-pm4</p> 
	<p>PSR+3500 SN16C6095 00029 – MRE01011</p> 







## Appendix 4. General description rock samples VISU

Nº	Name rock	Alteration degree	Unit	Veins	Phenocrysts	Cavities	Color	Composition	Grain size	Comments / remarks	Photos
1	05ch094	Very high	Cinto Ignimbrite ashflow	Yes	No	Yes	Grey/white	Quartz, jarosite, chalcedony	Fine	Vuggy silica. Chalcedony vein	
2	04MRE003	Very high	Cinto Ignimbrite	Yes	Yes	No	Grey/white	Quartz	Fine	Veins of oxides. Phenocryst of silica	
3	05ch101	Very high	Rhyolitic Dome	No	No	Yes	Red	Quartz	Fine	Very oxidized. Vuggy silica. Cavities filled	
4	05ch099	Very high	Rhyolitic Dome	Yes	No	Yes	Red	Quartz	Fine	Very oxidized. Vuggy silica. Cavities filled. Quartz veins	
5	Q1	Very high	Cinto Ignimbrite	No	No	No	White	Alunite	Very fine	Homogeneous	
6	05ch096	High	Cinto Ignimbrite	No	Yes	No	Grey/pink	Quartz	Medium	Veins of oxides. Mafic minerals	
7	05ch097	Very high	Tertiary Marine Sediments	No	No	Yes	White/Purple		Fine	Vuggy	
8	05ch095	High	Cinto Ignimbrite ashflow	No	Yes	Yes	Orange	Quartz	Fine	Phenocrysts of silica. Vuggy	
9	04MRE125	Very high	Cinto Ignimbrite	No	No	No	White	Kaolinite	Very fine	Homogeneous	
10	05ch053	Very low	Cinto Ignimbrite	No	Yes	No	Black	Andesite-Dacite	Very fine	Unaltered. Mafic phenocrysts. Pyroxene-amphibolite phenocrysts	
11	04MRE225A	High	Rhyolitic Dome	No	Yes	No	White	Kaolinite	Very fine	Few phenocrysts of mafic minerals. Homogeneous	
12	05ch093	High	Cinto Ignimbrite	No	Yes	Yes	Red	Quartz	Fine	Vuggy quartz. Phenocryst of silica	
13	04MRE044	Very low	Cinto Ignimbrite	No	Yes	No	Green	Andesite-Dacite	Very fine	Ignimbrite. Porphyritic texture. Amphibolite phenocrysts. Matrix of glass fragments	
14	MRE01052	High	Rhyolitic Dome	Yes	Yes	No	Red	Quartz	Fine	Very oxidized. Phenocryst of silica	
15	04MRE044	High	Cinto Ignimbrite	No	Yes	No	White	Illite	Very fine	Homogeneous. Few phenocrysts of mafic minerals	
16	MRE02021	Low	Rhyolitic Dome	No	Yes	No	Green	Andesite-Dacite	Very fine	Amphibolite and pyroxene phenocrysts	
17	MRE01011	High	Cinto Ignimbrite	Yes	Yes	No	Red/Grey	Quartz	Fine	Very oxidized.	
18	MRE01051	Low	Rhyolitic Dome	No	Yes	No	Green	Andesite-Dacite	Very fine	Mafic and plagioclase phenocrysts. Very fine matrix	
19	Mex1pm4	High	Aluvial deposit	No	Yes	Yes	Grey	Quartz	Very fine	Vuggy quartz. Phenocryst replaced by clays or empty cavities	
20	MRE02053_PM3	High	Cinto Ignimbrite	No	Yes	No	Beige/White		Very fine	Few phenocrysts of mafic minerals	
21	MRE02022	Low	Rhyolitic Dome	No	Yes	No	Green		Very fine	Fine matrix.	
22	MRE02053_PM1	Low	Cinto Ignimbrite	No	No	No	Dark grey	Quartz	Very fine	Homogene. Massive	
23	MRE02023	High	Rhyolitic Dome	No	Yes	No	White	Kaolinite	Very fine	Weak. Homogeneous	
24	MRE02034_PM1	High	Cinto Ignimbrite	No	Yes	No	Grey		Fine	Mafic minerals. Phenocrysts replaced by clay minerals.	
25	Mex1_pm5	Very high	Aluvial deposit	No	No	Yes	Grey	Quartz	Very fine	Vuggy silica. Oxidized	
26	MRE02028_PM1	Very high	Cinto Ignimbrite	No	Yes	Yes	Beige/Grey	Quartz	Fine	Phenocrysts of silica	

Nº	Name rock	Alteration degree	Unit	Veins	Phenocrysts	Cavities	Color	Composition	Grain size	Comments / remarks	Photos
27	43_MRE01055	Very Low	Cinto Ignimbrite	No	Yes	No	Dark grey	Andesite-Dacite	Very fine	Amphibolite and pyroxene phenocrysts. Very fine and homogeneous matrix	
28	MRE02025	High	Rhyolitic Dome	No	Yes	No	Orange/Yellow	Quartz	Very fine	Phenocrysts of silica. Mafic phenocrysts replaced by alteration minerals.	
29	45_MRE02055_P M2	Very high	Cinto Ignimbrite	No	No	No	White	Alunite	Very fine	Homogeneous	
30	MRE02019	Low	Rhyolitic Dome	No	Yes	No	Grey	Andesite-Dacite	Very fine	Amphibolite phenocrysts. Very fine matrix	
31	MRE02033	High	Cinto Ignimbrite	No	Yes	No	White	Illite	Very fine	Phenocrysts of silica	
32	Mex1_PM3	High	Aluvial deposit	No	Yes	No	White	Alunite	Very fine	Cavities filled with clay. Phenocrysts of silica	
33	MRE02053_PM2	Very high	Cinto Ignimbrite	No	No	No	White		Fine	Some oxides	
34	MRE02032_PM1	High	Cinto Ignimbrite	No	No	No	White/Grey		Fine		
35	MRE02026	Low	Rhyolitic Dome	No	Yes	No	White	Illite	Fine	Some phenocrysts of amphibolite and quartz	
36	MRE02027_PM1	Low	Rhyolitic Dome	No	Yes	No	White	Illite	Fine	Few phenocrysts of amphibolite and quartz	
37	04MRE256A	Low	Rhyolitic Dome	No	Yes	No	Green	Andesite-Dacite	Variable	Preserves original texture. Huge phenocrysts	

Appendix 5. Cross-sections obtained from SAM in HyMap images

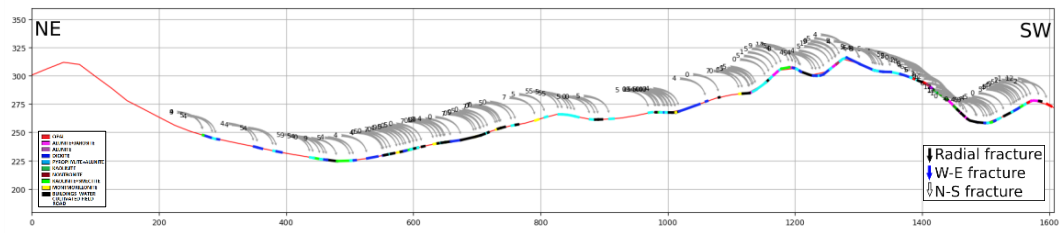


Figure 5.1. Cabo de Gata 2, cross-section P.C.1.

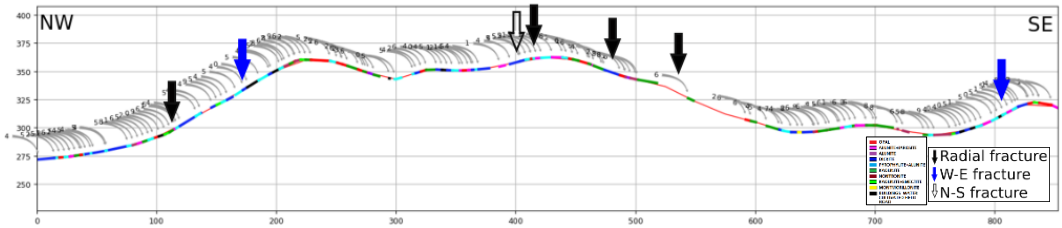


Figure 5.2. Cabo de Gata 2, cross-section P.C.2.

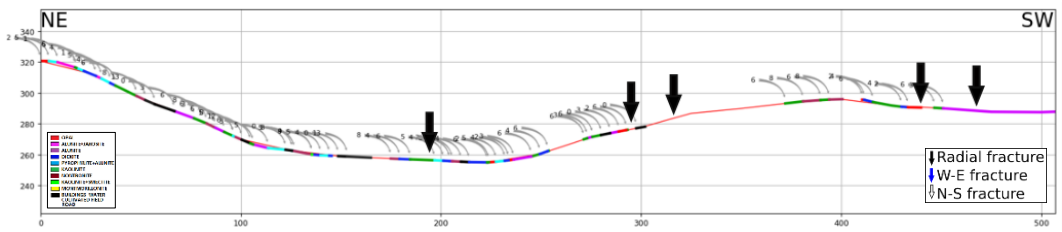


Figure 5.3. Cabo de Gata 2, cross-section P.C.3.

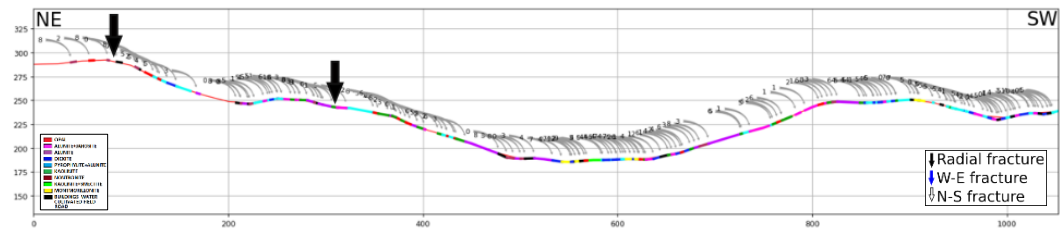


Figure 5.4. Cabo de Gata 3, cross-section P.C.4.

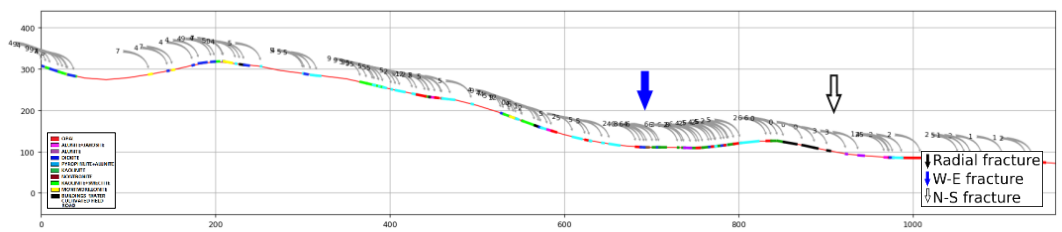


Figure 5.5. Cabo de Gata 2, cross-section P.T.1.

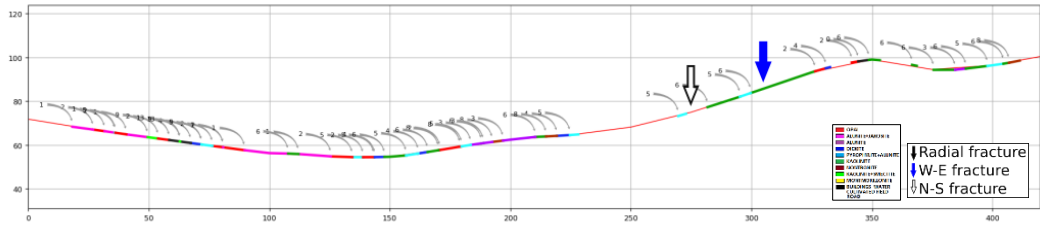


Figure 5.6. Cabo de Gata 2, cross-section P.T.2.

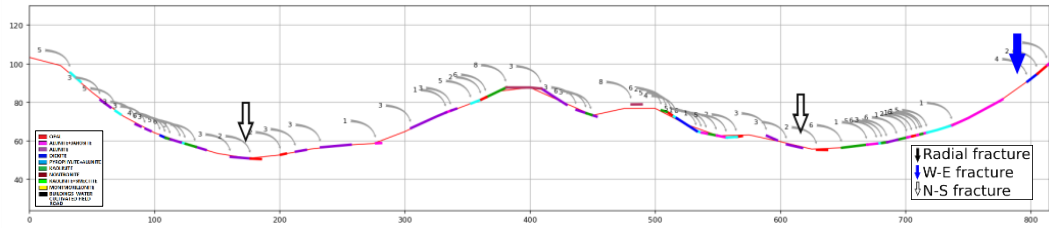


Figure 5.7. Cabo de Gata 2, cross-section P.T.3.

Appendix 6. Cross-sections obtained from SAM in PRISMA images

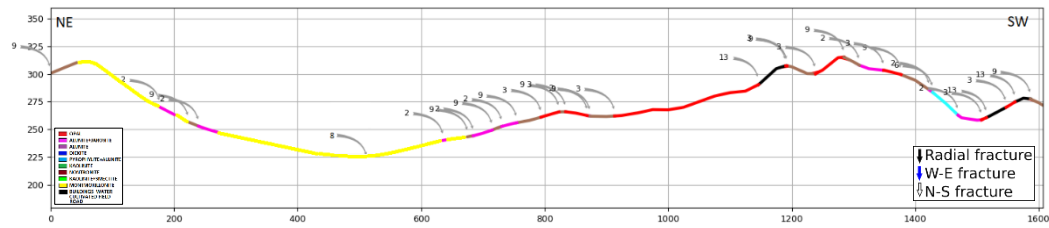


Figure 6.1. PRISMA cross-section P.C.1.

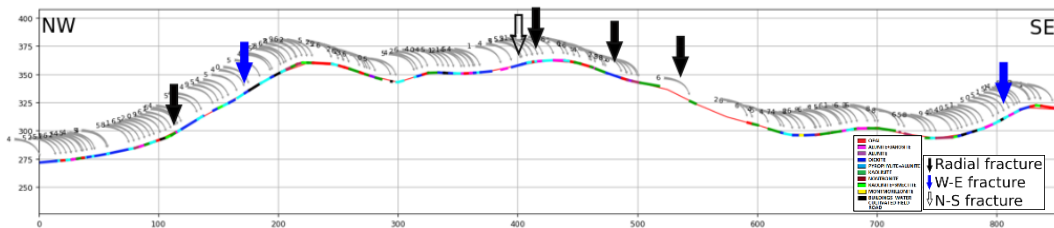


Figure 6.2. PRISMA cross-section P.C.2.

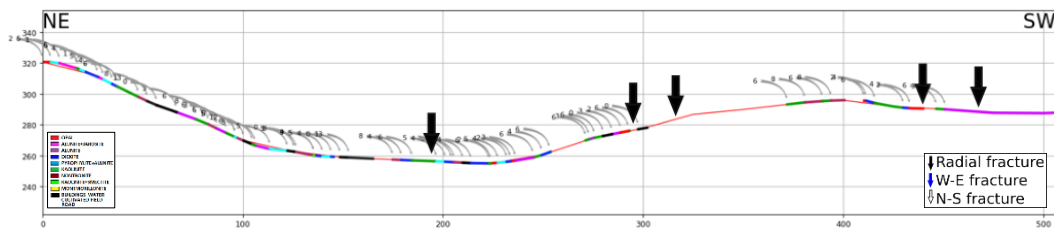


Figure 6.3. PRISMA cross-section P.C.3.

